UNIVERSIDADE FEDERAL DA BAHIA
ESCOLA POLITÉCNICA
PROGRAMA DE PÓS-GRADUAÇÃO EM ENGENHARIAS
ELÉTRICA E DE COMPUTAÇÃO

Tese de Doutorado

Improving Rational Modeling Realization for Accurate EMT Simulations

Alexandre Akira Kida

Salvador–BA, Brasil
Setembro, 2025

Alexandre Akira Kida

Improving Rational Modeling Realization for Accurate EMT Simulations

Tese de Doutorado apresentada ao Programa de Pós-graduação em Engenharias Elétrica e de Computação da Universidade Federal da Bahia, como parte dos requisitos necessários à obtenção do título de Doutor em Engenharias Elétrica e de Computação.

Orientadores
Prof. Dr. Fernando Augusto Moreira
Prof. Dr. Antonio Carlos Siqueira de Lima

Salvador–BA, Brasil
Setembro, 2025

K46 Kida, Alexandre Akira.
Improving rational modeling realization for accurate EMT simulations / Alexandre Akira Kida. – Salvador, 2025.

122f.: il. color.

Orientadores: Prof. Dr. Fernando Augusto Moreira.
Prof. Dr. Antonio Carlos Siqueira de Lima.

Tese (doutorado) – Curso de Pós-Graduação em Engenharias Elétrica e de Computação, Escola Politécnica, Universidade Federal da Bahia, 2025.

1. Análise de transitório eletromagnético. 2. Frequência - distorção. 3. Sistemas elétricos. I. Moreira, Fernando Augusto. II. Lima, Antonio Carlos Siqueira de. III. Universidade Federal da Bahia. IV. Título.

CDD: 621.317

Ficha catalográfica elaborada pela Biblioteca Bernadete
Sinay Neves, Escola Politécnica – UFBA.

Alexandre Akira Kida

Improving Rational Modeling Realization for Accurate EMT Simulations

Tese de doutorado aprovada como parte dos requisitos para a obtenção do grau de Doutor em Engenharias Elétrica e de Computação do Programa de Pós-Graduação em Engenharias Elétrica e de Computação da Universidade Federal da Bahia.

Banca examinadora:

Documento assinado digitalmente
gov.br
FERNANDO AUGUSTO MOREIRA
Data: 12/10/2025 20:31:35-0300
Verifique em https://validar.iti.gov.br

Prof. Dr. Fernando Augusto Moreira - UFBA
Orientador

Documento assinado digitalmente
gov.br
ANTONIO CARLOS SIQUEIRA DE LIMA
Data: 13/10/2025 10:27:22-0300
Verifique em https://validar.iti.gov.br

Prof. Dr. Antonio Carlos Siqueira de Lima - UFRJ
Orientador

Documento assinado digitalmente
gov.br
FABIANO FRAGOSO COSTA
Data: 15/10/2025 11:22:29-0300
Verifique em https://validar.iti.gov.br

Prof. Dr. Fabiano Fragoso Costa - UFBA
Membro

Documento assinado digitalmente
gov.br
TITO LUIS MAIA SANTOS
Data: 14/10/2025 09:06:50-0300
Verifique em https://validar.iti.gov.br

Prof. Dr. Tito Luís Maia Santos - UFBA
Membro

Documento assinado digitalmente
gov.br
ALBERTO RESENDE DE CONTI
Data: 15/10/2025 14:02:33-0300
Verifique em https://validar.iti.gov.br

Prof. Dr. Alberto Resende De Conti - UFMG
Membro

Documento assinado digitalmente
gov.br
WASHINGTON LUIZ ARAUJO NEVES
Data: 17/10/2025 20:44:43-0300
Verifique em https://validar.iti.gov.br

Prof. Dr. Washington Luiz Araújo Neves - UFCG
Membro

Salvador - Bahia - Brasil, 02 de setembro de 2025.

I dedicate this thesis to Cintia, Amelia, Antonio, and my paw-friend Rosquinha (in memoriam).

Resumo

Simulações no domínio do tempo com métodos de integração linear multipasso, como o trapezoidal, estão sujeitas a um erro frequentemente negligenciado em análises de transitórios eletromagnéticos (EMT) conhecido como distorção em frequência ou *frequency warping*. Esta tese estabelece tal erro como um problema fundamental que compromete a acurácia das simulações EMT, exigindo abordagens específicas para sua mitigação. Inicialmente, investigou-se como o *frequency warping* se manifesta no método combinado nodal e espaço de estados, evidenciando que pequenos erros de *frequency warping* podem se acumular ao longo do tempo, gerando distorções significativas mesmo com passos de tempo conservadores. Em seguida, explorou-se a modelagem de equivalentes dependentes de frequência por funções racionais, introduzindo o *Complex Vector Fitting* (CVF) no contexto de sistemas de potência. O CVF reduziu a raiz do erro quadrático médio (RMSE) em até oito ordens de magnitude em relação ao *Vector Fitting* tradicional, ao relaxar a restrição de conjugado complexo nos polos e resíduos do modelo racional. Diferenças em relação à passividade dos modelos também foram observadas. Dois métodos foram propostos para reduzir o *frequency warping* sem alterar o tamanho do passo de tempo: o *Pole-Residue Compensation* (PRC), que ajusta polos e resíduos do modelo para compensar as perturbações numéricas nos autovalores discretizados; e o *Frequency-shifted Pole-Residue Compensation* (FPRC) que combina o PRC, o CVF e a translação em frequência. O PRC permitiu ampliar o passo de tempo em até 6,7 vezes sem perda de acurácia ou reduzir o RMSE em até 24 vezes. Graças ao baixo custo computacional e à natureza de pós-processamento, o PRC pode ser facilmente integrado a rotinas de simulação já existentes. O FPRC alcançou ganhos ainda maiores, com passos de tempo até 35 vezes maiores ou reduções do RMSE em até 901 vezes. Os resultados foram validados através de simulações computacionais típicas de estudos EMT: linhas de transmissão, transformadores de potência, rede de distribuição e sistema de transmissão de energia elétrica. Os métodos desenvolvidos nesta tese superam limitações das simulações EMT, oferecendo flexibilidade para aumentar a acurácia ou reduzir significativamente o custo computacional, viabilizando análises mais confiáveis de sistemas elétricos em larga escala.

Abstract

Time-domain simulations carried out with linear multistep integration methods, such as the Trapezoidal Rule, are subject to an error often neglected in electromagnetic transient (EMT) analyses, known as *Frequency Warping*. This thesis establishes the *frequency warping* as a fundamental problem that compromises the accuracy of EMT simulations, requiring specific approaches for its mitigation. Initially, the manifestation of *frequency warping* in the combined nodal and state-space method was investigated, demonstrating that small errors due to *frequency warping* can accumulate over time, generating significant distortions even with conservative time-step sizes. Subsequently, the modeling of frequency-dependent equivalents through rational functions was explored, introducing Complex Vector Fitting (CVF) in the context of power systems. The CVF methodology significantly improved accuracy, reducing the Root Mean Square Error (RMSE) by up to eight orders of magnitude compared to the conventional Vector Fitting approach, by relaxing the complex conjugate constraint on model poles and residues. Differences regarding model passivity were also observed. Two techniques were developed to reduce *frequency warping* without reducing the time step size: Pole-Residue Compensation (PRC), which adjusts poles and residues of rational models to compensate for numerical perturbations in the discretized system eigenvalues; and Frequency-shifted Pole-Residue Compensation (FPRC), which utilizes CVF and adds frequency translation to the compensation. PRC enabled time steps 6.7 times larger without accuracy loss or, for the same step size, errors up to 24 times smaller in terms of RMSE. Due to the low computational cost and post-processing nature of the PRC, it can be easily integrated into existing simulation routines. FPRC achieved even greater gains: steps up to 35 times larger or RMSE reduction by a factor of up to 901 times. The results were validated through computer simulations of electrical networks, which included components such as transmission lines and power transformers, as well as equivalents of electric power distribution and transmission networks. The techniques developed in this thesis overcome limitations of conventional EMT simulations, offering flexibility to significantly increase accuracy or substantially reduce computational cost, thus enabling more reliable analyses of modern large-scale power systems.

Acknowledgment

The development of a doctoral thesis constitutes, in itself, a complex and challenging task. This challenge is significantly amplified when it becomes necessary to balance research with professional demands as a faculty member at the Federal Institute of Bahia. Thus, the completion of this work was only possible thanks to the support and collaboration of the people I acknowledge here.

First and foremost, I thank God for placing extraordinary people in my path throughout this entire academic journey.

To my wife Cintia, I express my deepest gratitude for her constant encouragement and the strength she gave me to persist in the face of challenges encountered, making the entire process lighter and more meaningful.

To my parents, Antonio and Amelia, I am grateful for their unconditional support and confidence in my ability to complete this thesis.

To my friends Daniel Batista, Washington Souza, Rodrigo Barros (*in memoriam*), and Alberto Vianna, for the countless conversations and constant support throughout the entire doctoral journey.

To my advisor, Dr. Fernando Augusto Moreira, for his consistent and dedicated guidance throughout this entire research. His extensive technical expertise, meticulous attention to detail, and remarkable patience in listening to me and providing counsel during challenging moments were essential to this work's completion. I could always count on his unwavering support and mentorship.

To my co-advisor, Dr. Antonio Carlos Siqueira de Lima, the "Tony", with whom I had the privilege of meeting in person on two occasions abroad, at conferences in Greece and Mexico, I thank him for his contribution to the development of this research and for being a true guru. His guidance was decisive in directing the work, making it more focused and coherent.

Finally, I thank the members of the examining committee, Dr. Alberto Resende De Conti, Dr. Fabiano Fragoso Costa, Dr. Tito Luís Maia Santos, and Dr. Washington Luiz Araújo Neves, for accepting to dedicate their time and expertise to evaluate this work.

Contents

List of Figures

List of Tables

Chapter 1

Introduction

Electric power systems are experiencing profound transformations driven by the global transition from fossil fuels to renewable energy sources (GONZALEZ-LONGATT, 2015). This shift encompasses the integration of intermittent and stochastic renewable energy sources, such as solar photovoltaic and wind power, energy storage devices with varying time constants, high-voltage DC technologies, and cross-country interconnections in both AC and DC (PAOLONE *et al.*, 2020). These developments introduce complex network dynamics and pose significant challenges to traditional power system planning and operations.

High-accuracy simulations are indispensable for capturing the intricate interactions within modern power systems, particularly since analytical solutions are often unavailable (JI and XING, 2023). In this regard, time-domain Electromagnetic Transient (EMT) simulations play a crucial role in enabling a detailed understanding and analysis of the dynamic behavior of electric power systems. These simulations generate “snapshots” of the instantaneous voltage and current waveforms at discrete time intervals (steps), closely mirroring their real-world counterparts. The fidelity of EMT simulations can be further improved through advances in numerical methods or through refined mathematical modeling, such as incorporating detailed power electronic models, closed-loop control dynamics, frequency-dependent equipment behavior, and nonlinear magnetic effects, leading to more accurate and reliable system representations.

In EMT simulations, time-domain solutions are obtained through numerical integration methods that solve differential circuit equations. These methods must exhibit stability, accuracy, and computational efficiency to meet the requirements of EMT applications (BRANDWAJN, 1977). Among linear multi-step integration methods, the trapezoidal rule offers second-order accuracy and is A-stable, meaning its stability is independent of the chosen time-step size (DAHLQUIST, 1963). As a result, it is extensively employed in commercial EMT-type simulators such as ATP, PSCAD, and EMTP (AMETANI, 2015).

Although widely used, the trapezoidal rule is prone to sustained numerical oscillations during abrupt variable changes and suffers from an error known as *frequency warping*. To address these oscillations, a common practice is to switch from the trapezoidal rule to the backward Euler method during discontinuities in inductor currents and capacitor voltages (MARTI and LIN, 1989). While frequency warping is not unique to the trapezoidal rule, it affects all linear multi-step methods to different degrees (BRAMBILLA and STORTI-GAJANI, 2003). Frequently overlooked, frequency warping distorts the frequency response in the discrete-time domain, potentially leading to inaccurate solutions, especially in oscillatory circuits (BRAMBILLA and STORTI-GAJANI, 2003).

High-accuracy modeling of power system components must account for their frequency-dependent characteristics, given the wide bandwidth of the EMT phenomena (ABDEL-RAHMAN *et al.*, 2003). However, simulating an entire electric power system with such a detailed representation significantly increases model complexity. Additionally, simulation times may become impractical due to computational resource limitations, such as processing power, memory, and storage, particularly for statistical studies and sensitivity analyses (LIMA *et al.*, 2020). A conventional approach that balances fidelity and computational burden involves representing part of the network as a frequency-dependent equivalent using rational models (GRIVET-TALOCIA and GUSTAVSEN, 2015).

1.1 Motivation

Frequency warping errors are particularly pronounced in circuits characterized by frequency oscillations (BRAMBILLA and STORTI-GAJANI, 2003). In modern electric power systems, the increasing integration of power electronic devices – such as those used in renewable energy and high-voltage DC systems – elevates the likelihood of frequency oscillations. These oscillations can reach several kV due to interactions between devices or between devices and the power grid (CHEN *et al.*, 2023). For instance, ZOU *et al.* (2018) documented a case in which a 1.27 kHz resonance emerged between a voltage-source converter-based high-voltage DC and the power grid. Therefore, careful analysis and effective mitigation strategies are essential for managing frequency oscillations. Frequency warping can also distort the output waveforms of frequency-dependent equivalents during time-domain simulations (DICLER, 2021). While the effects of frequency warping may appear subtle, accumulated errors over time can lead to significantly corrupted solutions, compromising the reliability of simulation results (BRAMBILLA and STORTI-GAJANI, 2003). Therefore, addressing frequency warping is critical for enhancing the accuracy and reliability of EMT simulations.

Developing methods that simultaneously enhance the accuracy and computational performance of electrical system models is crucial for advancing power system analysis. Curve-fitting techniques, such as the pole relocation algorithm known as Vector Fitting (VF) (GUSTAVSEN and SEMLYEN, 1999), are widely employed for synthesizing electrical systems through rational functions (CAMPELLO *et al.*, 2023).

YE *et al.* (2019) proposed the Complex Vector Fitting (CVF) method, a novel approach that relaxes the requirement for complex-conjugate pole-residue pairs. Originally developed for modeling baseband photonic systems through scattering parameters, CVF demonstrated its effectiveness in handling non-Hermitian systems with asymmetric frequency responses. Building upon this foundation, this thesis extends the CVF methodology to power system applications, demonstrating its potential for enhancing frequency-dependent equivalent modeling.

In addition to advancing modeling techniques, developing strategies to mitigate frequency warping errors is essential for enhancing EMT simulation accuracy, reliability, and computational efficiency. By enhancing rational models and implementing effective frequency warping mitigation strategies, simulations can better reflect real-world conditions, providing deeper insights into system dynamics.

1.2 Thesis Objectives

This thesis categorizes its objectives into general and specific objectives, as outlined below.

1.2.1 General Objective

This thesis primarily aims to enhance the accuracy and reliability of EMT simulations by addressing frequency warping errors and improving frequency-dependent equivalent modeling.

1.2.2 Specific Objectives

To achieve the general objective, this research pursues the following specific objectives:

- investigate the implications of frequency warping in EMT simulations and quantify its impact on simulation accuracy;
- conduct a comprehensive comparative analysis of VF and CVF techniques for admittance synthesis, with particular emphasis on computational efficiency, model accuracy, and passivity characteristics;

- evaluate the effectiveness and suitability of CVF methodology for developing computationally efficient reduced-order frequency-dependent equivalents;
- design, implement, and test novel compensation strategies to minimize frequency warping-induced distortions in EMT simulations, with verification on representative power system cases.

1.3 Publications

The following first-authored papers were produced as part of this thesis.

Journal papers:

PAPER#1. KIDA, A. A., LIMA, A. C. S., MOREIRA, F. A., MARTÍ, J. R., TARAZONA, J. "Inaccuracies due to the frequency warping in simulation of electrical systems using combined state–space nodal analysis", *Electric Power Systems Research*, v. 223, pp. 109657, 2023;

PAPER#2. KIDA, A. A., DICLER, F. N. F., CAMPELLO, SILVA, L. T. F. W., LIMA, A. C. S., MOREIRA, F. A., DIAS, R. F. S., TARANTO, G. N. "Enhancing Computation Performance of Rational Approximation for Frequency-Dependent Network Equivalents with Parallelism and Complex Vector Fitting", *Electric Power Systems Research*, v. 234, p. 110778, 2024;

PAPER#3. KIDA, A. A., LIMA, A. C. S., MOREIRA, F. M. VASCONCELLOS. "Improving EMT Simulations Using Frequency-Shifted Rational Approximations", *Electric Power Systems Research*, In press;

PAPER#4. KIDA, A. A., LIMA, A. C. S., MOREIRA, F. M. VASCONCELLOS. "High-Accuracy EMT Simulations through Pole-Residue Compensation", *Electric Power Systems Research*, In press.

Conference paper:

PAPER#5. KIDA, A. A., LIMA, A. C. S., MOREIRA, F. A., MICRONI, D. "Emprego do Ajuste Vetorial Complexo na Síntese Racional de Sistemas Representados por Admitâncias". *X Simpósio Brasileiro de Sistemas Elétricos*, pp. 1-6, Manaus, Amazonas, Brazil, Oct 2023.

1.4 Thesis Outline

Besides this first introductory chapter, this thesis has five chapters described below:

- Chapter 2 presents an overview of the current state of the art, highlights research gaps, and outlines the primary contributions of this thesis;
- Chapter 3 analyzes the frequency warping error and its impact on the combined nodal-SSE method. This chapter is based on PAPER#1;
- Chapter 4 introduces the concept of rational modeling and assesses the accuracy and computational performance of VF and CVF across four test cases. This chapter is based on PAPER#2 and PAPER#5;
- Chapter 5 presents the developed methodologies to reduce frequency warping; This chapter is based on PAPER#3 and PAPER#4;
- Chapter 6 states the main conclusions of this thesis.

Chapter 2

Literature Review

This chapter provides a literature review on frequency warping and frequency-dependent equivalents in EMT simulations, as outlined in the introduction, aiming to establish existing knowledge, analyze previous research, and situate this thesis within the current state-of-the-art.

2.1 Frequency Warping

In general terms, frequency warping refers to the transformation (or mapping) of an original set of frequencies to another different (distorted or *warped*) frequency scale (OPPENHEIM and JOHNSON, 1972). Depending on the application, frequency warping can be either a deliberate technique for altering frequency content or an unintended error in digital simulations.

In the domain of audio processing, frequency warping is employed as a *technique* to alter the spectral content of sound by remapping the original set of frequencies to a new set of frequencies (EVANGELISTA and CAVALIERE, 2001). This approach has practical applications in various fields, including speech recognition (LEE and ROSE, 1998; UPADHYAY and ROSALES, 2018; YEUNG *et al.*, 2021), voice conversion (TIAN *et al.*, 2017), and pitch modulation (EVANGELISTA and CAVALIERE, 2001). These applications leverage frequency warping to achieve desired acoustic effects or to enhance the performance of audio processing algorithms.

However, in the context of digital simulations, frequency warping manifests as an *error* introduced by the discretization process. In digital filter design, frequency warping causes discrepancies between analog and digital cutoff frequencies. This issue can be reduced by pre-warping the digital frequency to align with the analog frequency specifications (TAN, 2008; YANG *et al.*, 2009). For instance, PRESTI (1983) addressed the frequency warping by pre-warping the poles and zeros of Laplace-defined digital filters using their frequencies. Decades later, TENG *et al.* (2016) applied a similar pre-warping strategy to enhance notch filter tuning in motion controllers. Frequency warping also poses challenges in the digital implementation of phase-locked loops, where WANG *et al.* (2019) compensated for it by pre-warping proportional-integral controllers using the detected angular frequency.

In time-domain simulations, frequency warping emerges as a numerical error that affects all linear multi-step methods, including the trapezoidal rule (BRAMBILLA and STORTI-GAJANI, 2003). This error distorts the system frequency response, compromising the accuracy and reliability of digital simulations (BRAMBILLA and D'AMORE, 1993). This thesis focuses on the impact of frequency warping in the context of EMT simulations.

The impact of frequency warping in time-domain simulations is not a new topic, but research on it remains relatively limited in specialized literature, especially for electric power systems. Initial reports on the frequency-dependent behavior of inductors and capacitors due to discretization date back to BRANDWAJN (1977). This behavior was also examined by MARTI and LIN (1989) and the EMTP Theory Book (DOMMEL, 1996), although these works did not explicitly call the phenomenon frequency warping.

BRAMBILLA and D'AMORE (1993) introduced the frequency warping term in the context of time-domain simulations to describe frequency alterations of output waveforms caused by the trapezoidal rule method. These alterations were undetected by the amplitude error tolerance of the SPICE simulator.

PERŠIČ (1994) demonstrated that the trapezoidal rule method causes only frequency deviations, whereas the Gear method introduces both frequency and amplitude errors. Additionally, PERŠIČ and BASARIČ (2001) extended the theoretical analysis of frequency warping for the trapezoidal rule and highlighted the potential for chaotic behavior in simulations that employ variable time-step sizes. Subsequently, BRAMBILLA and STORTI-GAJANI (2003) provided a rigorous error analysis of frequency warping regarding the trapezoidal rule, backward Euler, and Gear methods for time-domain simulations. Their work revealed that frequency warping can be seen as a perturbation of the poles (or eigenvalues) of the linearized ordinary differential problem. They also established that the frequency warping is directly related to the order of the linear multi-step method used. For example, the trapezoidal rule is a second-order linear multi-step method (DAHLQUIST, 1963). RAHKONEN and ANDREANI (2005) extended the frequency warping analysis to include forward Euler and Adams-Bashforth methods, while also evaluating the impact of frequency warping on the quality factor of oscillatory circuits.

In exploring strategies for frequency warping mitigation, BRAMBILLA and STORTI-GAJANI (2003) showed no universal rule for selecting an integration method in time-domain simulations. While higher-order methods can limit frequency warping, they may also introduce instability. The authors also noted that the harmonic balance method, unlike linear multi-step methods, does not suffer from frequency warping. However, this approach can face convergence issues and performance degradation in the presence of nonlinearities.

CONSTANTINESCU *et al.* (2010); GHEORGHE *et al.* (2009) developed adaptive time-step adjustments based on energy balance to reduce frequency warping. OMAR FARUQUE and DINAVAHI (2010) proposed an adaptive discretization framework to reduce frequency warping, where the discretization method varies with the input type, particularly for hardware-in-the-loop applications. GAO (2015) presented a theoretical analysis of frequency warping error for a high-order integration method based on the Obreshkov formula (GAD *et al.*, 2009), which is both A-stable and L-stable, thereby reducing frequency warping. DICLER (2021) demonstrated that frequency warping also affects frequency-dependent equivalents. The author proposed a pre-processing step to pre-warp the system frequency response for frequency-dependent equivalents. However, the resulting rational model is only compensated for frequency warping at the specific time-step size used during pre-processing. If the simulation requires a different time-step size, the VF fitting process must be repeated with the new pre-warped input response. PALMAL *et al.* (2023) recommended using time-step size criteria from MARTI and LIN (1989), specifically one over ten times and one over twenty times the maximum frequency of interest for the trapezoidal rule and backward Euler methods, respectively, to limit the distortion below 3%.

2.2 Frequency Dependent Equivalents

A common approach to achieving accurate, yet computationally efficient, EMT simulations involves dividing the electric power system into two areas: the study area (modeled in detail) and the external area (approximated) (GUSTAVSEN, 2002). The frequency characteristics of the external area can be preserved using frequency-dependent equivalents. A widely used approach for obtaining these equivalents involves representing the transfer function matrix as rational models (GRIVET-TALOCIA and GUSTAVSEN, 2015). A port of a rational model can be characterized using admittance, impedance, or scattering parameters. Admittance and impedance parameters define the relationship between voltages and currents, while scattering parameters link incident and reflected waves. Scattering parameters are particularly advantageous in high-speed electronics, as they provide more precise measurements at very high frequencies compared to admittance or impedance parameters (GUSTAVSEN and DE SILVA, 2013).

Another approach to obtain frequency-dependent equivalents is the descriptor formulation proposed in VARRICCHIO and GOMES (2018), which solves an augmented set of differential-algebraic equations derived from circuit model formulation. The resulting equations can be integrated into EMT simulators or synthesized as equivalent circuits (CAMPELLO *et al.*, 2021). However, most commercial EMT simulators are unable to export external equations. Therefore, a common practice involves fitting rational functions to tabulated frequency data samples obtained using frequency scan tools available in EMT simulators (GRIVET-TALOCIA and GUSTAVSEN, 2016).

Curve-fitting techniques have been under considerable investigation in recent years for realizing frequency-dependent equivalents through rational models (GRIVET-TALOCIA and GUSTAVSEN, 2015). The most popular of these techniques is the pole-relocation algorithm known as VF, developed in GUSTAVSEN and SEMLYEN (1999). Its popularity stems from its computational efficiency, accuracy, simplified formulation, versatility of application, and open-source nature (GRIVET-TALOCIA and GUSTAVSEN, 2015). It is also the curve-fitting method embedded in widely used EMT simulators such as ATP (HØIDALEN, 2024), PSCAD (GUSTAVSEN and NORDSTROM, 2008), and EMTP (NAREDO *et al.*, 2011).

Other curve-fitting techniques with unique characteristics include Frequency-Partitioning Fitting (NODA, 2005), Matrix Pencil Method (SHESHYEKANI *et al.*, 2012), and Loewner Matrix (KABIR and KHAZAKA, 2012). Some distinctions among these techniques are as follows. Frequency-Partitioning Fitting and VF follow iterative processes, whereas the Matrix Pencil Method and the Loewner Matrix do not. Notably, Frequency-Partitioning Fitting, the Matrix Pencil Method, and the Loewner Matrix do not require pole initialization, which simplifies their application. The Matrix Pencil Method and the Loewner Matrix are particularly effective for noisy data and are often used to determine the correct model order. However, VF and Frequency-Partitioning Fitting generally outperform these methods, providing higher accuracy and computational efficiency (CAMPELLO *et al.*, 2023; MORALES RODRIGUEZ *et al.*, 2020; SALARIEH and DE SILVA, 2021). More detailed comparisons are available in these references.

Regardless of the chosen approach, rational models face two key challenges: passivity and computational performance. Passivity implies that the model should never generate power under any applied voltage, regardless of frequency (GUSTAVSEN and SEMLYEN, 2001). Failure to achieve passivity can lead to unstable time-domain simulations (GUSTAVSEN, 2010). Thus, a post-processing routine to enforce passivity is paramount (GUSTAVSEN and SEMLYEN, 2009). Considerable research has been conducted on this topic (BRADDE *et al.*, 2022; DESCHRIJVER *et al.*, 2008a; GUSTAVSEN, 2007, 2008a; GUSTAVSEN and SEMLYEN, 2009; GUSTAVSEN, 2021; IHLENFELD and OLIVEIRA, 2021).

Several research efforts have also focused on enhancing the computational performance of VF (CAMPELLO *et al.*, 2020; CHINEA and GRIVET-TALOCIA, 2011; CHOU and SCHUTT-AINE, 2021; DESCHRIJVER *et al.*, 2008b; GANESHAN *et al.*, 2020; GUSTAVSEN, 2006; GUSTAVSEN and SEMLYEN, 2009; RAHIMI PORDANJANI and XU, 2014). The third version of VF incorporates several improvements, including the relaxation of the non-triviality constraint to enhance convergence (GUSTAVSEN, 2006), the introduction of a half-size singularity test for fast passivity assessment (GUSTAVSEN and SEMLYEN, 2009), and the use of QR decomposition to boost numerical performance (DESCHRIJVER *et al.*, 2008b)

The processing efficiency of the VF significantly degrades as the number of ports increases (CAMPELLO *et al.*, 2020). RAHIMI PORDANJANI and XU (2014) developed a method to accelerate VF convergence by refining pole initialization, which can also be employed as a model-order reduction technique. This methodology identifies the most relevant poles through frequency partitioning. CAMPELLO *et al.* (2020) introduced a stop criterion that automatically halts the VF iterative process when additional iterations do not significantly improve model accuracy. They also proposed a framework based on frequency partitioning and VF, identifying redundant poles through a model-order reduction procedure based on balanced truncation. CHOU and SCHUTT-AINE (2021) proposed an alternative and more efficient procedure to compute the residue matrix, which enhanced the speed of building a rational model with VF. Finally, hardware can further improve VF performance by employing parallel computing (CHINEA and GRIVET-TALOCIA, 2011) and GPU acceleration (GANESHAN *et al.*, 2020).

While VF is highly effective, its application is primarily restricted to physical (band-pass) systems. This limitation arises from the realness compliance requirement, which enforces complex conjugacy constraints on pole-residue pairs. YE *et al.* (2018) addresses this limitation indirectly by applying a constant frequency shift to all poles in the resulting state-space VF model, shifting the entire frequency response of the model to enable baseband modeling. However, this approach also shifts the negative frequencies of the rational model, which are retained in the baseband model proposed by the authors. YE *et al.* (2019) later introduced a variant of VF named CVF, based upon the concept of complex conjugacy relaxation proposed by LEI *et al.* (2008). CVF enables direct baseband modeling while reducing model complexity by using half-size models compared to the previous approach of YE *et al.* (2018). This innovation is critical for efficiently modeling non-physical systems without Hermitian symmetry YE *et al.* (2018). This symmetry implies that the positive frequency spectrum is equal to the complex conjugate of the negative frequency spectrum (BOASHASH, 2003). Baseband systems are inherently non-physical (KING and BRAZIL, 2017) and lack Hermitian symmetry. Since its introduction, CVF has been applied in modeling photonic integrated circuits characterized by scattering parameters (SPINA *et al.*, 2021; ULLRICK *et al.*, 2023; YE *et al.*, 2019, 2022).

2.3 General Remarks

The reviewed studies emphasize the challenges and ongoing research efforts associated with frequency warping and frequency-dependent equivalents. Building on this groundwork, the thesis introduces novel approaches to reduce frequency warping-induced distortions, enhancing the accuracy and reliability of EMT simulations. Furthermore, by investigating the potential application of CVF, a method originally developed for photonic modeling using scattering parameters, in electrical power systems, this work aims to improve the synthesis of frequency-dependent equivalents.

Chapter 3

The Frequency Warping in Time-domain Simulations

Building on the literature review from the previous chapter, this chapter analyzes frequency warping error in time-domain simulations of an RLC circuit through nodal and state-space formulations. It demonstrates that even when adhering to a conservative time-step criterion ($h \leq 1/(10f_{\max})$), where $f_{\max}$ is the maximum frequency of interest, simulations can still produce significant errors due to frequency warping. This chapter is based on PAPER#1, considering the labeling convention established in Section 1.3.

3.1 Introduction

The development of the EMT-type of programs started around 50 years ago, initially as the EMTP (DOMMEL, 1969) and later as a "family" of programs such as MicroTran, ATP, PSCAD, and EMTP. Using numerical integration methods, these simulators obtain the solution in the discrete-time domain by transforming differential equations, which represent network dynamics, into algebraic equations. Remarkably, the basic modeling principles introduced by DOMMEL (1969) are still used in many EMT-type programs today (AMETANI, 2015), including the trapezoidal rule method and the method of characteristics for modeling traveling waves in transmission lines.

The trapezoidal rule is an implicit integration method with second-order accuracy, defined by the recurrence relation:

$$y_{n+1} = y_n + \frac{h}{2}\left[f(t_n, y_n) + f(t_{n+1}, y_{n+1})\right], \quad f(t,y) = \frac{dy}{dt}, \tag{3.1}$$

where h is the time-step size.

The trapezoidal rule is a member of the linear multi-step methods and is A-stable, guaranteeing that the numerical solution remains bounded for any time-step size when applied to a stable linear system (DAHLQUIST, 1963). However, it may produce bounded oscillations around the expected solution during sharp transients or discontinuities (MARTI and LIN, 1989). Despite its classification as a multi-step method, its recurrence relation (3.1) requires only the information from the immediately preceding time step. This structure facilitates a computationally efficient implementation.

However, linear multi-step methods introduce frequency warping – a numerical error due to the non-linear mapping of the frequency axis (BRAMBILLA and STORTI-GAJANI, 2003). This distortion alters the system frequency response and can be interpreted as deviations in the observed values of inductances and capacitances (DOMMEL, 1996). A detailed review of frequency warping and its implications was provided in Chapter 2.

The local truncation error estimators in digital simulators, being amplitude-based, fail to detect frequency alterations caused by the trapezoidal rule method (BRAMBILLA and D'AMORE, 1993). Consequently, even minor initial errors can accumulate over time, leading to significant deviations from the correct solution (BRAMBILLA and STORTI-GAJANI, 2003). This underscores the importance of analyzing inaccuracies caused by frequency warping, given their potential to distort system responses.

Frequency warping is particularly relevant in scenarios involving resonant phenomena, where discretized inductance and capacitance values shift the natural oscillation frequency. For instance, electric power systems with high penetration of power electronic converters, such as those in solar photovoltaic and wind power, experience reduced inertia. This can lead to poorly damped low- and high-frequency oscillations (BEZA and BONGIORNO, 2020). Furthermore, frequency warping can impact frequency-dependent equivalents, potentially leading to inaccuracies in system behavior at certain frequencies (DICLER, 2021).

System dynamics can be modeled using either nodal analysis or state-space equations. Nodal analysis is commonly employed in EMT-type simulators (AMETANI, 2015), while state-space equations are often used in platforms like Simulink and Modelica (MOORMANN and LOOYE, 2002). The state-space equation approach is particularly effective for wideband modeling of overhead lines (GUSTAVSEN, 2007; KUROKAWA *et al.*, 2009; MORCHED *et al.*, 1999) and underground cables (GUSTAVSEN, 2007; MORCHED *et al.*, 1999; RAMIREZ, 2008) in phase coordinates. State-space equations can be efficiently solved using recursive expressions implemented with the trapezoidal rule (GUSTAVSEN, 2007) and the so-called recursive convolutions (SEMLYEN and DABULEANU, 1975). More recently, DUFOUR *et al.* (2011) presented a hybrid methodology, Nodal-SSE, that combines nodal (or modified nodal) analysis and state-space equations.

It is important to notice that the key findings are not limited to the specific circuit studied. The chosen circuit was selected for its scalability to larger circuits, as frequency warping originates from the discretization of inductance and capacitance. The complexity of larger-scale applications may hinder the isolation of this particular phenomenon. Additionally, obtaining the analytical response of an RLC circuit for use as a benchmark is feasible, whereas achieving such a response for larger and more intricate circuits is often impractical.

3.2 The Frequency Warping Effect

The continuous-time domain transfer function of the integrator is

$$\frac{B(s)}{U(s)} = \frac{1}{s}, \tag{3.2}$$

where s is the complex frequency variable in the s-domain; $B(s)$ and $U(s)$ are the Laplace transforms of $b(t)$ and $u(t)$, respectively.

Applying the trapezoidal rule to derive the transfer function in (3.2) in the discrete-time domain yields the approximation:

$$\frac{B[z]}{U[z]} \approx \frac{h}{2}\frac{(1+z^{-1})}{(1-z^{-1})}, \tag{3.3}$$

where h is the time-step size ; $B[z]$ and $U[z]$ are the Z-transforms of $B(s)$ and $U(s)$, respectively; z is the complex variable in the Z-domain.

Equating (3.2) and (3.3) and solving for z yields the bilinear transformation (also known as the Tustin method) (YANG *et al.*, 2009):

$$z \approx \frac{1+0.5sh}{1-0.5sh}. \tag{3.4}$$

The mapping between the analog (continuous-time) frequency ω_a and its corresponding digital frequency ω is derived by substituting $s = j\omega_a$ and $z = e^{j\omega h}$ into the approximate relation (3.4). Solving for ω_a gives:

$$\omega_a = \frac{2}{h}\tan\left(\frac{\omega h}{2}\right). \tag{3.5}$$

The bilinear transformation maps stable[1] or unstable analog systems into stable or unstable discrete-time equivalents, respectively, regardless of the time-step size (A-stability property). The entire imaginary axis $s = j\omega_a$ is mapped uniquely

---

[1] Stable systems produce bounded outputs when excited by bounded inputs.

onto the 2π-length unit circle in the Z-plane. The nonlinear frequency mapping between ω_a and ω in (3.5) compresses the discrete-time frequency scale, introducing a numerical error known as frequency warping (BRAMBILLA and STORTI-GAJANI, 2003).

The Nyquist frequency limit (or folding frequency) is defined as (TAN, 2008):

$$\omega_{NY} = \frac{\pi}{h}, \tag{3.6}$$

$$f_{NY} = \frac{1}{2h}, \tag{3.7}$$

where ω_{NY} and f_{NY} are the Nyquist frequency limit in rad/s and Hz, respectively.

Evaluating the limit in (3.5) as $\omega \to \pm\omega_{NY}$ yields

$$\lim_{\omega \to \pm\omega_{NY}} \frac{2}{h} \tan\left(\frac{\omega h}{2}\right) = \lim_{\omega \to \pm\pi/h} \frac{2}{h} \tan\left(\frac{\omega h}{2}\right) = \pm\infty. \tag{3.8}$$

Fig. 3.1 illustrates the bilinear transformation mapping. Within the analog frequency range $0 \leq \omega_a \leq 0.2\omega_{NY}$, the mapping appears nearly linear. However, in the range $0.2\omega_{NY} \leq \omega_a \leq \omega_{NY}$, the non-linearity becomes more pronounced, compressing the analog frequencies into the digital frequency range $0.2\omega_{NY} \leq \omega \leq 0.64\omega_{NY}$. The entire analog frequency range $-\infty \leq \omega_a \leq \infty$ is mapped onto the digital frequency range $-\omega_{NY} \leq \omega \leq \omega_{NY}$.

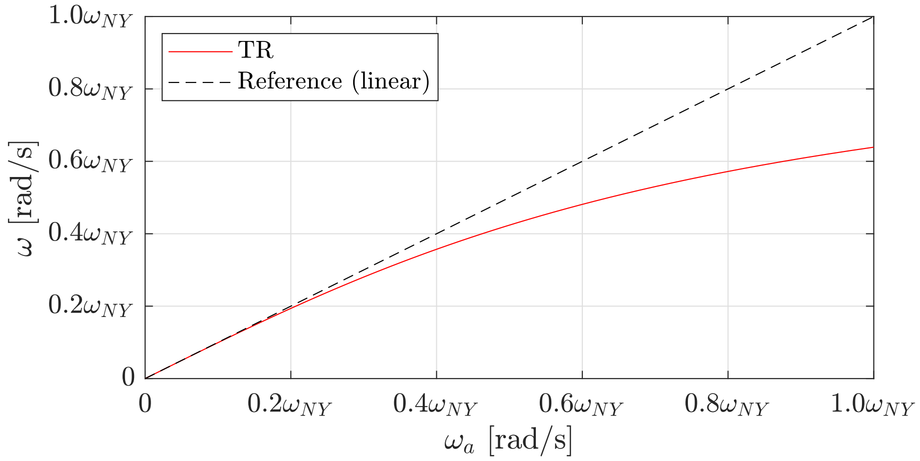

Fig. 3.1: Mapping between digital and analog frequencies of a signal using trapezoidal rule.

The representation of an analytic continuous-time pole p_s in the z-domain p_z is

$$p_z = e^{p_s h}. \tag{3.9}$$

Applying the first-order Taylor series approximation in (3.9) results in

$$p_z \approx \frac{1 + 0.5p_s h}{1 - 0.5p_s h}. \tag{3.10}$$

By comparing (3.4) with (3.10), one can verify that the bilinear transformation is a first-order approximation of $e^{p_s h}$. When mapping back p_z to the continuous-time domain, p_s is not obtained, but rather a new (perturbed) pole p_{per}, such that

$$p_{\text{per}} = \frac{\ln(p_z)}{h}. \tag{3.11}$$

The difference between p_z and p_{per} increases nonlinearly with the time-step size. This numerical error, resulting from frequency warping, can be interpreted as a perturbation of the original eigenvalues. Moreover, if the analytic solution has complex-conjugate eigenvalues, the discrete-time solution will also exhibit complex-conjugate eigenvalues.

When the real part of p_s is altered, the simulated attenuation constant deviates from its analytical counterpart. Similarly, modifying the imaginary part of p_s changes the natural oscillation frequency of the simulation. Consequently, in circuits with a resonant frequency, the discretized solution will exhibit oscillations at frequencies other than the true resonant frequency (BRAMBILLA and STORTI-GAJANI, 2003). This behavior can be interpreted as the inductances and capacitances in the discrete-time domain becoming frequency dependent, a topic explored further in Sections 3.2.1 and 3.2.2.

3.2.1 Discrete-time Behavior of an Inductor

In the discrete-time domain, assuming the trapezoidal rule as the integration method, the relationship between the voltage $v_L(t)$ and the current $i_L(t)$ of an inductor with a continuous-time inductance L is

$$i_L(t) - i_L(t-h) = \frac{h}{2L} v_L(t) + \frac{h}{2L} v_L(t-h). \tag{3.12}$$

By considering $v_L(t)$ and $i_L(t)$ as the input and output, respectively, it is possible to express the former as

$$v_L(t) = e^{j\omega t} \tag{3.13}$$

and the latter as

$$i_L(t) = Y_L e^{j\omega t}, \tag{3.14}$$

where Y_L is the admittance of the discretized inductor.

By replacing (3.13) and (3.14) in (3.12),

$$Y_L e^{j\omega t} - Y_L e^{j\omega(t-h)} = \frac{h}{2L} e^{j\omega t} + \frac{h}{2L} e^{j\omega(t-h)}. \tag{3.15}$$

By isolating Y_L,

$$Y_L = \frac{h}{2L} \frac{e^{j\omega h} + 1}{e^{j\omega h} - 1}. \tag{3.16}$$

The impedance of the discretized inductor is

$$Z_L = \frac{1}{Y_L} = \frac{2L}{h} \frac{e^{j\omega h} - 1}{e^{j\omega h} + 1} = j\frac{2L}{h} \tan\left(\frac{\omega h}{2}\right). \tag{3.17}$$

By defining L_{DT} as a discrete-time equivalent inductance, its impedance is given by:

$$Z_L = j\omega L_{DT}. \tag{3.18}$$

The inspection in (3.17) and (3.18) yields (DOMMEL, 1996)

$$L_{DT} = \frac{2L}{\omega h} \tan\left(\frac{\omega h}{2}\right). \tag{3.19}$$

Equation (3.19) indicates that L_{DT} is frequency-dependent. Alternatively, it can be expressed as

$$L_{DT} = \Psi L, \tag{3.20}$$

$$\Psi = \frac{2}{\omega h} \tan\left(\frac{\omega h}{2}\right), \tag{3.21}$$

where Ψ is the frequency warping error for the bilinear transformation.

3.2.2 Discrete-time Behavior of a Capacitor

The frequency warping error of a capacitor with a continuous-time capacitance C follows the same procedure shown in (3.13)-(3.19), considering the following voltage and current relationship:

$$v_C(t) - v_C(t-h) = \frac{h}{2C} i_C(t) + \frac{h}{2C} i_C(t-h), \tag{3.22}$$

where $v_C(t)$ and $i_C(t)$ is capacitor voltage and current, respectively.

The discrete-time equivalent of C, named C_{DT}, has the following discrete-time impedance:

$$Z_C = \frac{1}{j\omega C_{DT}}, \tag{3.23}$$

Finally, C_{DT} is frequency-dependent (DOMMEL, 1996), such that

$$C_{DT} = \frac{2C}{\omega h} \tan\left(\frac{\omega h}{2}\right). \tag{3.24}$$

Thus,

$$C_{DT} = \Psi C. \tag{3.25}$$

Fig. 3.2 depicts the frequency response of Ψ (3.21), L_{DT}/L (3.20) and C_{DT}/C (3.25). As $\omega \to \omega_{NY}$, the deviation increases non-linearly and becomes infinitely large. This result is consistent with the limit of Ψ as $\omega \to \omega_{NY}$, such that

$$\lim_{\omega \to \omega_{NY}} \frac{2}{\omega h} \tan\left(\frac{\omega h}{2}\right) = \infty. \tag{3.26}$$

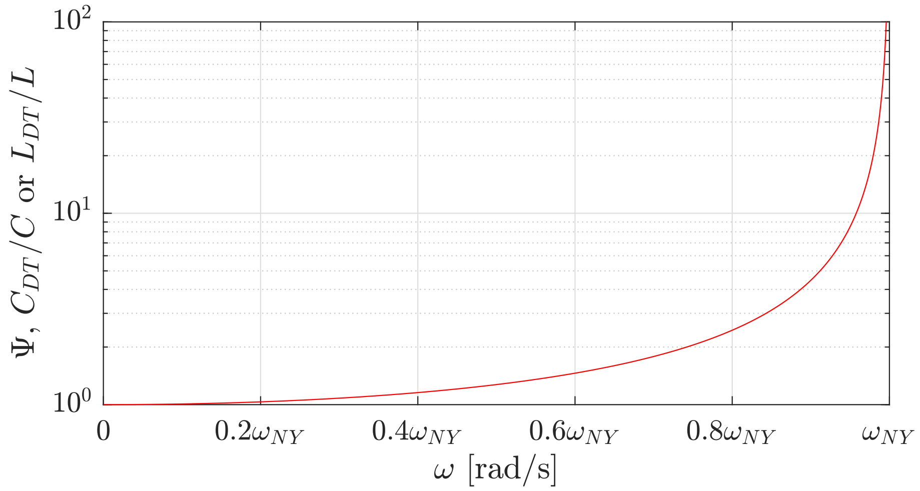

Fig. 3.2: Frequency response of the Ψ, C_{DT}/C and L_{DT}/L using trapezoidal rule with the Y-axis was truncated at 10^2.

Likewise, no distortion in L_{DT} and C_{DT} is observed when $\omega \to 0$, as

$$\lim_{\omega \to 0} \tan\left(\frac{\omega h}{2}\right) / \left(\frac{\omega h}{2}\right) = 1. \tag{3.27}$$

3.3 Electrical Circuit under Consideration

The frequency warping-induced numerical error is evaluated by utilizing the electrical circuit known as Case RLC, depicted in Fig. 3.3. The circuit parameters are $u(t) = cos(120\pi t)$ V, $R_1 = 0.1\ \Omega$, $L_1 = L_2 = 1\,\mu$H, $C_1 = 100\,\mu$F and $C_2 = 1\,\mu$F. The switch S_1 has been open long and closes at $t = 0$ s. The analysis focuses on the voltage at capacitor C_1, $V_{C_1}(t)$.

This study considers only lumped-parameter components, and considers only lumped-parameter components, neglecting any distributed-parameter effects, as their analysis are beyond the scope of this study. The use of a lumped-parameter model is a deliberate simplification to provide a clear and fundamental understanding of how the frequency warping-induced error manifests in a well-defined system.

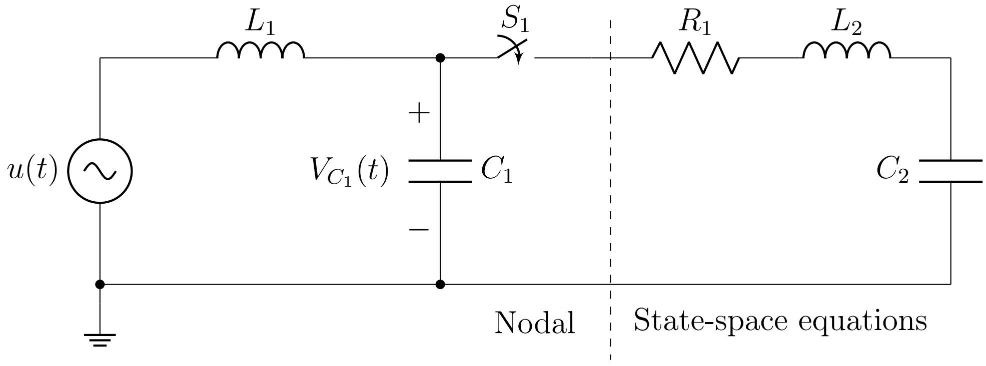

Fig. 3.3: Lumped electrical circuit under consideration, Case RLC.

The analytical solution of $V_{C_1}(t)$ is

$$V_{C_1}(t) = K_1(t) + K_2(t) + K_3(t), \tag{3.28}$$

where

$$K_1(t) = 1.001 \times 10^{-2} e^{-4.9995\times 10^4 t} \cos(1.003\,793 \times 10^6 t - 2.907^o) \text{ V}, \tag{3.29}$$

$$K_2(t) = 1.001 \times 10^{-2} e^{-4.998t} \cos(0.099\,499 \times 10^6 t + 179.43^o) \text{ V}, \tag{3.30}$$

and

$$K_3(t) = \cos(376.99t) \text{ V}. \tag{3.31}$$

Equations (3.29) and (3.30) have damped oscillation frequencies of 159.758 kHz and 15.836 kHz, respectively. The last term (3.31) corresponds to the steady-state response.

3.4 Problem Formulation

This section provides detailed information about the combined Nodal-SSE representations of the Case RLC illustrated in Fig. 3.3.

3.4.1 Nodal Representation

The branch formed by L_1 and C_1 in Fig. 3.3 is represented using nodal analysis, modeled through the well-known companion circuits of DOMMEL (1969), as illustrated in the left portion of Fig. 3.4. The trapezoidal rule is employed as the solution method for the network differential equations.

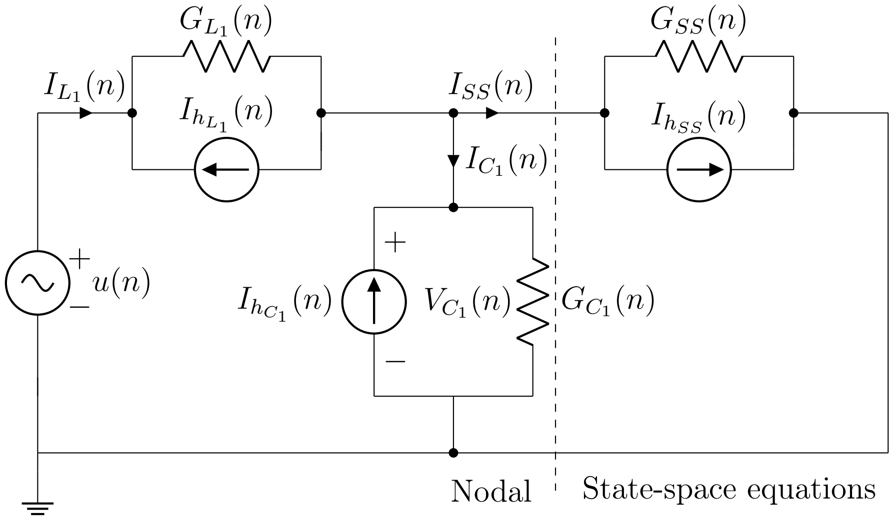

Fig. 3.4: Case RLC represented by companion circuits.

3.4.2 State-space Equations Representation

The branch formed by R_1, L_2, and C_2 in Fig. 3.3 is represented using state-space equations, using two solution methods: the trapezoidal rule and the recursive convolutions.

Consider the following single-input single-output relationship in the s-domain:

$$I(s) = Y(s)V(s), \tag{3.32}$$

where $I(s)$ and $V(s)$ are the terminal current and voltage, respectively; $Y(s)$ is the nodal admittance.

$Y(s)$ can be approximated over the frequency band of interest with a rational model $\overline{Y}(s)$ in a pole and residue form (GUSTAVSEN, 2007), such that

$$Y(s) \approx \overline{Y}(s) = \sum_{i=1}^{N_p} \frac{r_i}{s-p_i} + D + sE, \tag{3.33}$$

where p_i and r_i are the i_{th} poles (real or complex conjugate) and residue of the rational model; N_p is the number of poles of the rational model; D and E are real values that correspond to the constant term and the s-proportional term of the model, respectively. This chapter assumes proper rational model, such that $D \neq 0$ and $E = 0$.

The output $i(t)$ can be computed through the convolution property in (3.32) yields:

$$i(t) = \overline{y}(t) * v(t) = \int_0^\infty \overline{y}(\tau)v(t-\tau)d\tau, \tag{3.34}$$

where $i(t)$, $v(t)$, and $\overline{y}(t)$ are the time-domain current, time-domain voltage, and

$\overline{y}(t)$ is the time-domain impulse response of $\overline{Y}(s)$.

If exponential functions can approximate the step response of a system, then it is possible to employ a recursive solution for the convolution integral (SEMLYEN and DABULEANU, 1975). Thus,

$$i(t) = e^{ph} i(t-h) + \int_0^h e^{p\tau} v(t-\tau) d\tau. \tag{3.35}$$

The state-space equations regarding the output $i(t)$ and the input $v(t)$ are given by (GUSTAVSEN and MO, 2007; GUSTAVSEN, 2013):

$$i(n) = \sum_{i=1}^{N_p} \big(r_i x_i(n) + (D + r_i \lambda_i) v(n) \big), \tag{3.36}$$

$$x_i(n) = \alpha_i x_i(n-1) + (\alpha_i \lambda_i + \mu_i) v(n-1), \tag{3.37}$$

where subscript i indicates its dependency with i-th pole of the rational model; x_i is an internal state of $i(n)$; α_i, λ_i, and μ_i are constants determined by the solution method.

For the trapezoidal rule, the constants in (3.36) and (3.37) (GUSTAVSEN, 2007) are

$$\alpha_i = \frac{2 + p_i h}{2 - p_i h}, \tag{3.38}$$

$$\lambda_i = \mu_i = \frac{h}{2 - p_i h}. \tag{3.39}$$

For the recursive convolutions method, the constants in (3.36) and (3.37) (SEMLYEN and DABULEANU, 1975) are

$$\alpha_i = e^{p_i h}, \tag{3.40}$$

$$\lambda_i = -\frac{1}{p_i} \left(1 + \frac{1 - \alpha_i}{p_i h} \right), \tag{3.41}$$

$$\mu_i = \frac{1}{p_i} \left(\alpha_i + \frac{1 - \alpha_i}{p_i h} \right). \tag{3.42}$$

Note that as $p_i h \to 0$, λ_i (3.41) and μ_i (3.42) tend to infinity, leading to inaccurate results.

The right-hand side in (3.36) can be interpreted as a Norton equivalent, with a history current source $I_{h_{SS}}$ and a conductance G_{SS}, such that

$$I_{h_{SS}}(n) = \sum_{i=1}^{N_p} r_i \big(\alpha_i x(n-1) + (\alpha_i \lambda_i + \mu_i) V_{SS}(n-1) \big), \tag{3.43}$$

$$G_{SS} = D + \sum_{i=1}^{N_p} r_i \lambda_i. \tag{3.44}$$

Equations (3.43) and (3.44) resemble the companion circuit modeling approach, allowing the state-space equations to be incorporated into nodal analysis, as illustrated in Fig. 3.5.

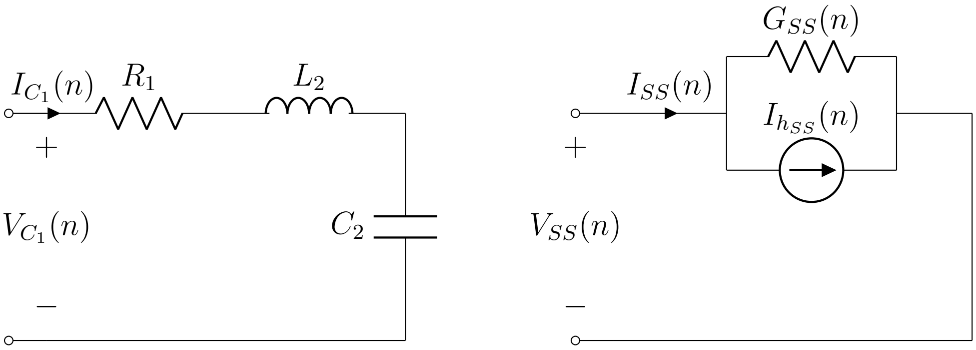

Fig. 3.5: Branch of the Case RLC modeled by state-space equations (left) and its respective companion circuits (right), where $I_{SS}(n) = i(n)$.

3.5 Numerical Results and Discussion

This section provides initial considerations and numerical results related to frequency warping deterioration in time-domain circuits.

3.5.1 Initial Considerations

The aim is to analyze the behavior of the transient with an oscillating frequency of 15.836 kHz, as described by (3.30), while the transient with a higher oscillating frequency of 159.758 kHz, given by (3.29), decays rapidly and is not of primary interest for this study. The time-step size should be sufficiently small to capture the system dynamics, at the cost of increased computational effort. The criterion presented in MARTI and LIN (1989) for choosing the time-step size h was adopted.

$$h \leq \frac{1}{10 f_{max}} \leq \frac{1}{10 \cdot 15.836\,\text{kHz}} \leq 6.31\,\mu\text{s}, \tag{3.45}$$

where f_{max} is the highest frequency of interest, which for the Case RLC is 15.836 kHz.

The maximum time-step size used in this chapter is 4 µs, satisfying the criterion outlined in (3.45).

This study employs the combined Nodal-SSE method introduced by DUFOUR *et al.* (2011) to model the system. Specifically, the trapezoidal rule method is employed to solve the branch containing L_1 and C_1, which is represented using a nodal representation. On the other hand, the branch comprising R_1, L_2, and C_2 is modeled using state-space equations and solved using either trapezoidal rule or recursive convolutions. Table 3.1 summarizes the time-step sizes, solution methods, and terminologies used in this work.

Table 3.1: Nomenclatures regarding the solution methods and time-step size

Nomenclature	Solution method Nodal	 State-space equations	h (µs)
TR_1	Trapezoidal rule	Trapezoidal rule	1
TR_2	Trapezoidal rule	Trapezoidal rule	2
TR_4	Trapezoidal rule	Trapezoidal rule	4
RC_1	Trapezoidal rule	Recursive convolutions	1
RC_2	Trapezoidal rule	Recursive convolutions	2
RC_4	Trapezoidal rule	Recursive convolutions	4

3.5.2 Trapezoidal Rule as the Solution Method for State-space Equations

The trapezoidal rule solves the state-space equations within the combined Nodal-SSE formulation. The waveforms of $V_{C_1}(t)$ for TR_1, TR_2, and TR_4 are depicted at the top of Figs. 3.6, 3.7, and 3.8, respectively, alongside the analytical responses. The absolute errors of TR_1, TR_2, and TR_4 relative to the analytical responses are displayed at the bottom of Figs. 3.6, 3.7, and 3.8, respectively. These errors increase over time as the signals gradually become out-of-phase due to differences in the frequencies of the analytical (frequency warping-free) and simulated waveforms. No difference appeared between solving the entire network using the nodal method with trapezoidal rule and the combined method with trapezoidal rule. Therefore, these results were omitted from the figures for clarity.

The simulation in Fig. 3.6 exhibits an initial inaccuracy, characterized by a spike in the absolute error. This spike arises due to the high-frequency transient component in the analytical response (3.29), which decays rapidly and vanishes after approximately 0.1 s. The absolute error trend over time better illustrates the frequency warping effect than the voltage waveform. Near the maximum and minimum points of the sinusoidal wave, the slope becomes less steep, causing the absolute values of the simulated and analytical responses to converge. This convergence reduces the difference between the two responses, resulting in valleys in the absolute error.

When the time-step size is increased to 2 µs, the waveform of TR_2 in Fig. 3.7 exhibits a small but noticeable phase shift relative to the analytic response by the

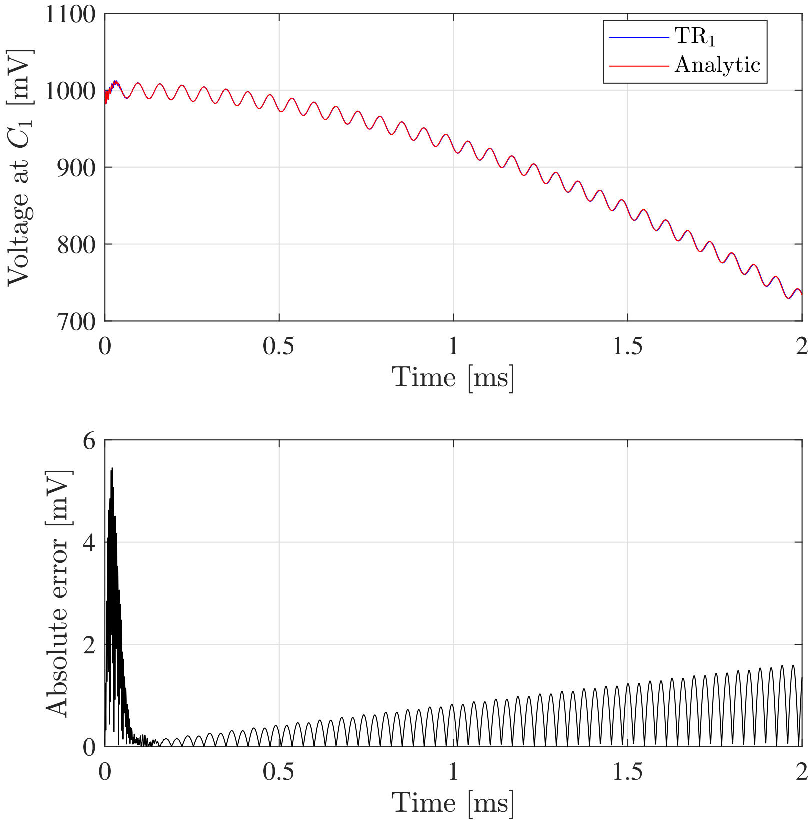

Fig. 3.6: Voltage at capacitor C_1 (top) and its absolute error (bottom) for TR$_1$.

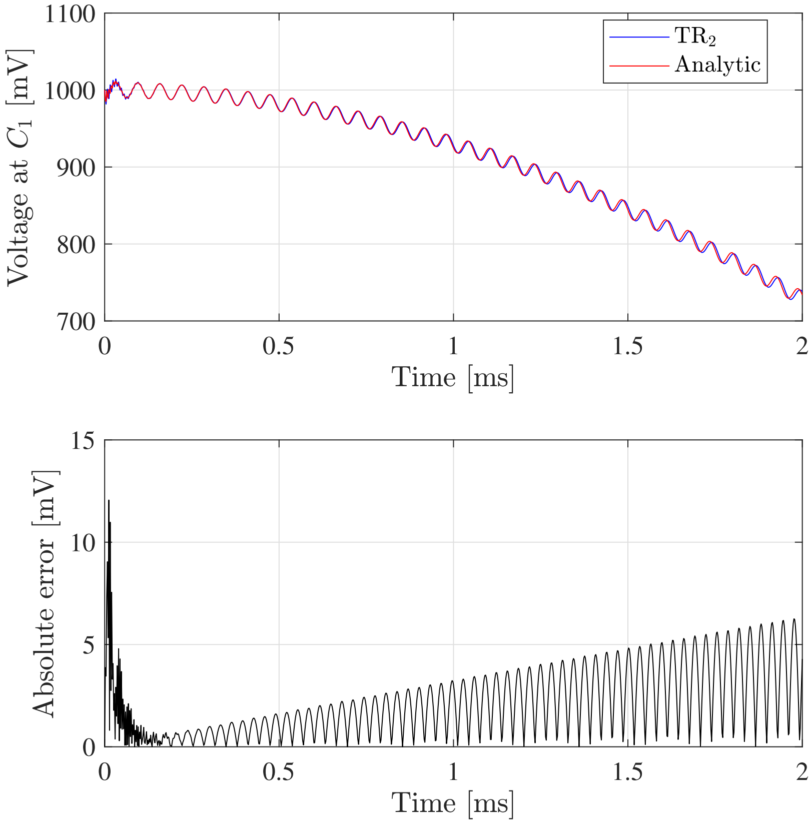

Fig. 3.7: Voltage at capacitor C_1 (top) and its absolute error (bottom) for TR$_2$.

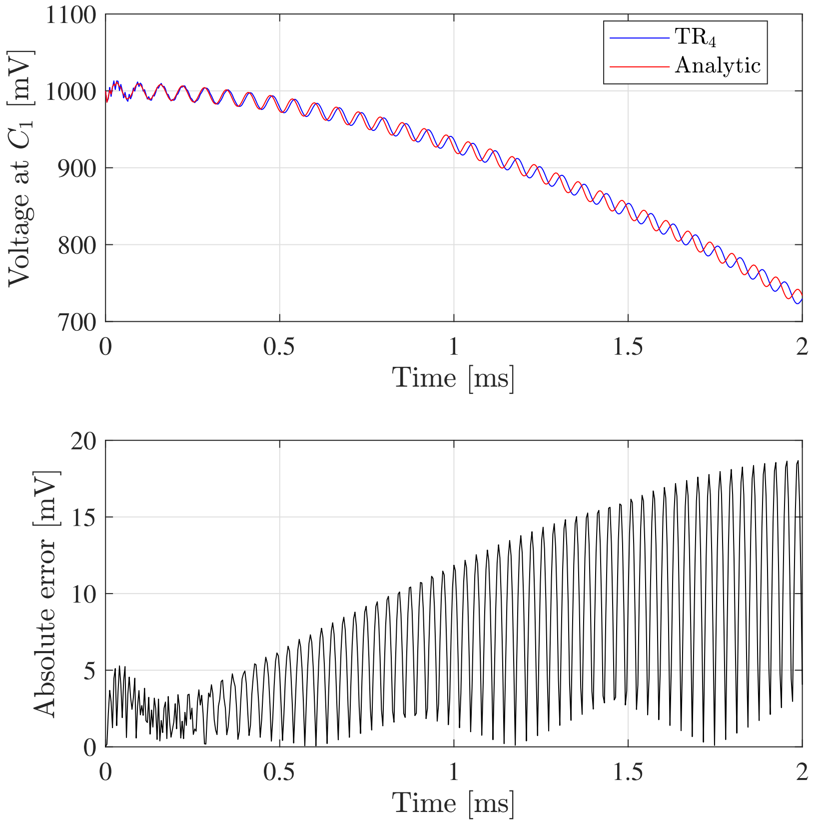

Fig. 3.8: Voltage at capacitor C_1 (top) and its absolute error (bottom) for TR$_4$.

end of the simulation ($t = 2\,\mathrm{ms}$). This phase shift arises from the frequency warping effect, which alters the natural oscillation frequency of the simulated circuit. The absolute errors depicted in Fig. 3.7 display characteristics similar to those observed for TR$_1$ in Fig. 3.6, but with larger amplitudes.

Setting $h = 4\,\mu\mathrm{s}$ results in a significant phase shift visible in the waveform of TR$_4$, as shown in Fig. 3.8. Toward the end of the simulation, TR$_4$ becomes nearly completely out of phase with the analytical response. The absolute error exhibits a much larger amplitude compared to those of TR$_1$ (Fig. 3.6) and TR$_2$ (Fig. 3.7). Additionally, the absolute error at the end of the simulation exceeds its initial value, highlighting the growing inaccuracy over time.

The increase in time-step size leads to a more pronounced frequency warping effect. This observation is quantitatively supported by evaluating the Root Mean Square Error (RMSE) metric, as presented in Table 3.2. The RMSE values demonstrate that larger time-steps amplify phase shifts and error accumulation, highlighting the trade-off between computational efficiency and accuracy.

Fig. 3.9 shows a pulsating absolute error behavior of TR$_4$ when the simulation duration is extended from 2 ms to 20 ms. The peaks and valleys in the absolute error indicate phase shifts of 180^o and 0^o, respectively, resulting from a frequency deviation caused by frequency warping. TR$_4$ takes about 2.4 ms to become completely out of

Table 3.2: RMSE for TR_1, TR_2, and TR_4 until $t = 2\,\mathrm{ms}$

Nomenclature	h (µs)	RMSE (V)
TR_1	1	817.33×10^{-6}
TR_2	2	2.74×10^{-3}
TR_4	4	8.86×10^{-3}

phase. In contrast, TR_1 and TR_2 require about 34.2 ms and 9.5 ms, respectively, to become 180^o out of phase compared to the analytical solution. The frequency warping in TR_1 is not easily observable in the waveform of $V_{C_1}(t)$ in Fig. 3.6 due to the short simulation duration of 2 ms. However, even with such a small time-step, error accumulation can lead to significant inaccuracies over longer simulations, as demonstrated in Figure 3.10. The frequency deviation of TR_4 Δf_{TR_4} relative to its analytical response can be estimated by the inverse of twice the period between two minima or two maxima. In this case, Δf_{TR_4} is approximately 104.2 Hz, which represents 0.66% of f_{max}.

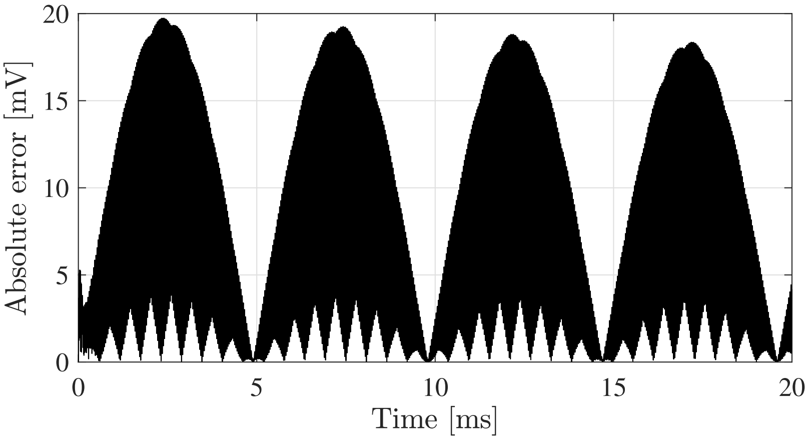

Fig. 3.9: Absolute error of TR_4 until $t = 20\,\mathrm{ms}$.

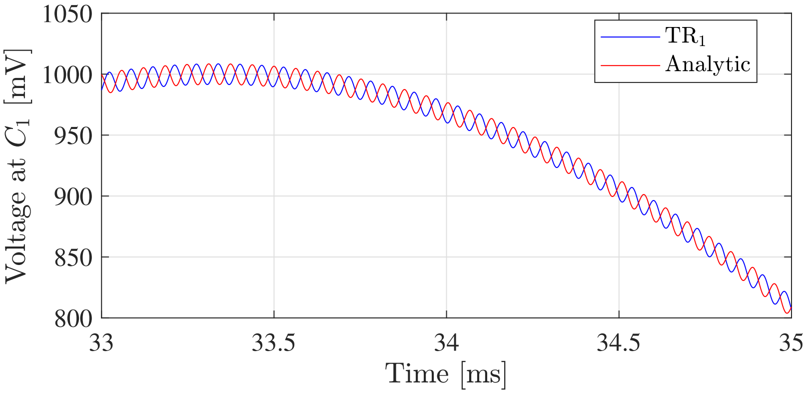

Fig. 3.10: Voltage at capacitor C_1, from 33 ms to 35 ms.

3.5.3 Recursive Convolutions as the Solution Method for State-space Equations

This section presents the results using recursive convolutions as the solution method for the state-space equations. The waveforms and analytical responses for RC_1, RC_2, and RC_4 are shown in Figs. 3.11, 3.12, and 3.13, respectively. The absolute error of each method relative to the analytical response is depicted in Figs. 3.11, 3.12, and 3.13, respectively.

In contrast to TR_1, as seen in Fig. 3.6, the absolute error of RC_1 shows a less pronounced peak at the beginning of the simulation, as depicted in Fig. 3.11.

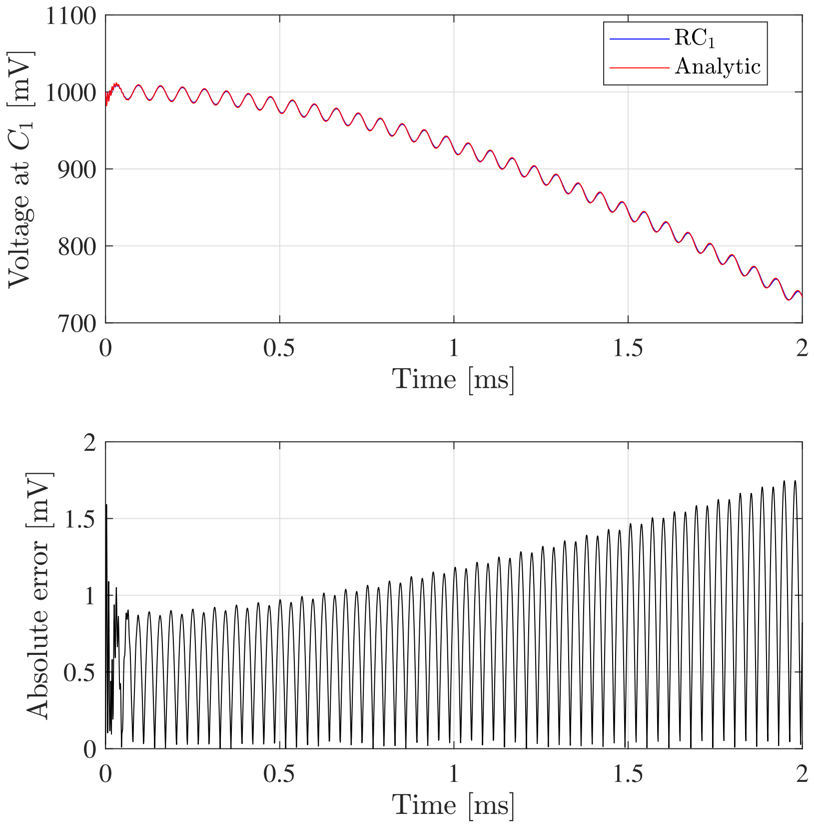

Fig. 3.11: Voltage at capacitor C_1 (top) and its absolute error (bottom) for RC_1.

Setting $h = 2\,\mu\text{s}$, the RC_2 waveform exhibits a slight decrease in amplitude and a phase shift due to a frequency deviation, as illustrated in Fig. 3.12. These numerical errors are evident in the absolute error behavior depicted, which begins with a larger amplitude compared to that observed for TR_2 in Fig. 3.7.

Increasing the time-step size to $4\,\mu\text{s}$ results in an initial phase inversion in the waveform of RC_4, as shown in Fig. 3.13. In this case, the waveform of $V_{C_1}(t)$ starts out-of-phase by 180^o and gradually realigns due to the frequency deviation induced by the frequency warping. A detailed mathematical analysis of this initial phase inversion in RC_4 is provided in Appendix A. The absolute error in Fig. 3.13 begins

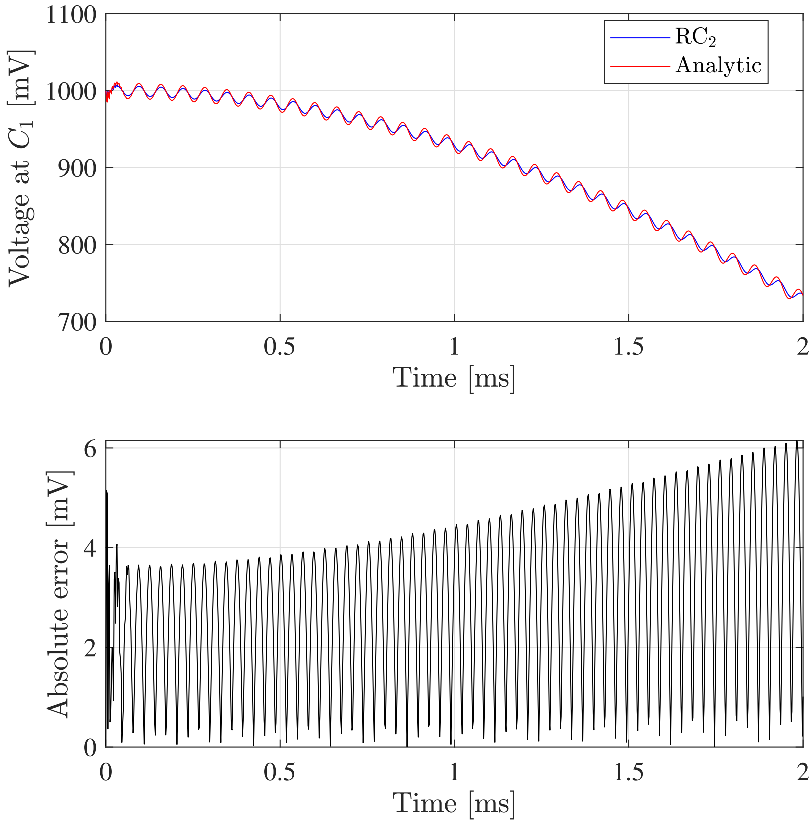

Fig. 3.12: Voltage at capacitor C_1 (top) and its absolute error (bottom) for RC$_2$.

at its maximum value due to the 180^o phase shift but diminishes as the waveform of RC$_4$ gets in phase.

The RMSE values for the state-space equations using recursive convolutions as the solution method are presented in Table 3.3. As expected, the RMSE exhibits a non-linear increase with the time-step size.

Table 3.3: RMSE for RC$_1$, RC$_2$, and RC$_4$, until $t = 2\,\text{ms}$

Nomenclature	h (µs)	RMSE (V)
RC$_1$	1	882.64×10^{-6}
RC$_2$	2	3.30×10^{-3}
RC$_4$	4	10.33×10^{-3}

The simulation time of RC$_4$ was extended from $t = 2\,\text{ms}$ to $t = 20\,\text{ms}$, as shown in Fig. 3.14. The pulsating trend of the absolute error begins with a maximum phase shift of 180^o. Using the same methodology applied for TR$_4$ in the previous section, the frequency deviation of RC$_4$ Δf_{RC_4} is approximately 102.5 Hz, corresponding to 0.65% of f_{max}.

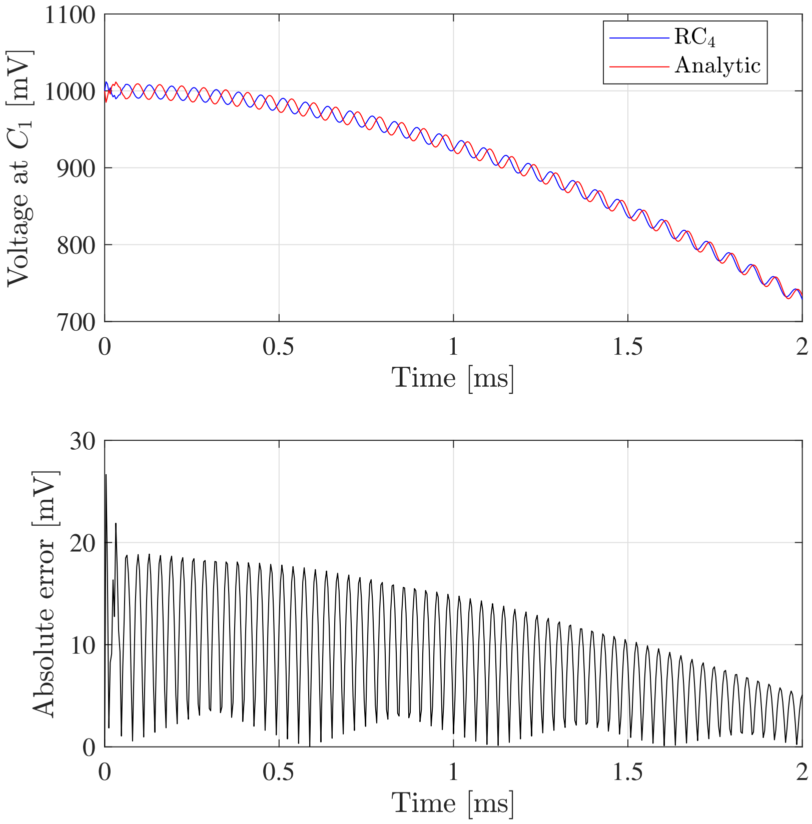

Fig. 3.13: Voltage at capacitor C_1 (top) and its absolute error (bottom) for RC$_4$.

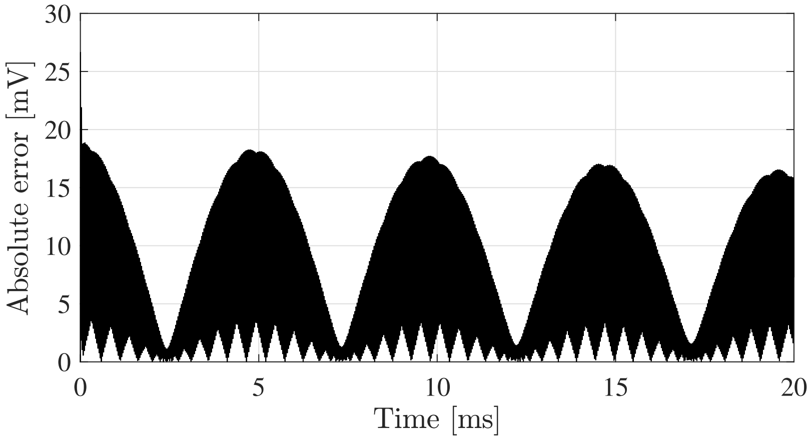

Fig. 3.14: Absolute error of RC$_4$ until $t = 20\,\text{ms}$.

3.6 General Remarks

This chapter explored the impact of a phenomenon known as frequency warping on the accuracy of EMT simulations.

Frequency warping arises from the behavior of inductances and capacitances in the discrete-time domain obtained through an integration method such as the trapezoidal rule, which is widely used in EMT-type simulators. It introduces a frequency deviation in the waveform, altering the natural oscillation frequency of the system. Over extended simulation periods, this deviation can lead to complete phase misalignment due to the accumulation of numerical errors. Furthermore, the frequency warping was observed even when a portion of the circuit was solved using the trapezoidal rule, as in the combined method, where the nodal part was solved with the trapezoidal rule and the state-space equations part was solved using recursive convolutions.

The numerical error introduced by the frequency warping was observed even for time-step sizes less than $1/(10f_{max})$, with simulations running up to 2 ms. This observation contradicts the conventional recommendation to mitigate frequency warping, as highlighted in MARTI and LIN (1989); PALMAL *et al.* (2023). Finally, the error increased non-linearly with the time-step size, affecting the accuracy of the overall simulation.

The next chapter will present frequency-domain modeling using rational functions with and without the complex conjugacy constraint.

Chapter 4

Rational Modelling

Building upon the state-space formulation introduced in the previous chapter, this chapter focuses on the frequency domain, exploring strategies to improve the rational modeling realization of frequency-dependent equivalents for EMT studies. It leverages the flexible CVF technique introduced in Chapter 1 and builds upon PAPER#2 and PAPER#5, following the nomenclature presented in Section 1.3.

4.1 Introduction

Accurate EMT simulations are critical for analyzing electromagnetic phenomena in power systems, supporting equipment design, system planning, and secure operation across a wide range of scenarios. However, their high computational burden poses significant challenges, especially when modeling large-scale power systems. To address this, a common approach divides the system into two subsystems: the study area and the external area (GUSTAVSEN, 2002). The former is modeled in detail, including its non-linearities, while a frequency-dependent equivalent characterizes the latter. The external area encompasses the remainder of the network and has linear and time-invariant characteristics tailored for analyzing EMT phenomena. The buses connecting the study and external systems are referred to as boundary buses (or equivalent ports). The selection of these ports considers the interest area where an EMT phenomenon or specific equipment will be analyzed (CAMPELLO *et al.*, 2023).

The external system is typically represented by a simplified short-circuit equivalent at grid frequency, preserving only its fundamental frequency (50 or 60 Hz) characteristics (CAMPELLO *et al.*, 2023). In contrast, frequency-dependent equivalents preserve their characteristics across a wide range of frequencies, offering higher accuracy (NODA, 2005). Rational models serve as universal approximators, capable of accurately representing various functions with arbitrary accuracy. These models are widely used to obtain frequency-dependent equivalents because they can accurately represent the frequency-dependent characteristics of linear time-invariant systems (GRIVET-TALOCIA and GUSTAVSEN, 2015). Approximating a frequency-dependent equivalent with rational functions simplifies the intricate admittance matrix, making it more manageable for computational analysis. A review of the methods for obtaining a frequency-dependent equivalent was detailed in Chapter 2.

Data-driven curve-fitting methods can synthesize a frequency-dependent equivalent using frequency response samples observed between ports of a system (TRIVERIO, 2021). These samples can be obtained through experimental measurements or EMT simulations. Data-driven curve-fitting methods produce closed-box models, which have the main disadvantage of providing less physical insight into the modeled system (TRIVERIO, 2021). The VF (GUSTAVSEN and SEMLYEN, 1999) is the most popular method for obtaining a frequency-dependent equivalent using rational models (GRIVET-TALOCIA and GUSTAVSEN, 2015).

However, regardless of the chosen approach, two common challenges arise. First, passivity is essential to ensure stable time-domain simulations, as the resulting rational model must absorb, not generate, active power under any given set of applied voltages (GUSTAVSEN and SEMLYEN, 2001). This constraint also ensures causality (GRIVET-TALOCIA and GUSTAVSEN, 2015). Therefore, a post-processing routine is necessary to enforce passivity (GUSTAVSEN, 2007). The second concern is the significant decrease in numerical performance as the number of ports increases. To address this, model-order reduction techniques can be applied (CAMPELLO *et al.*, 2020; RAHIMI PORDANJANI and XU, 2014). Alternatively, parallelizing the VF algorithm can improve numerical performance (CHINEA and GRIVET-TALOCIA, 2011).

This chapter explores strategies to improve the performance of rational models by leveraging CVF, model-order reduction, and parallelization. The application of CVF to synthesize a network characterized by its admittance parameters is thoroughly examined, as it has been applied to the modeling of photonic integrated circuits characterized by scattering parameters (SPINA *et al.*, 2021; ULLRICK *et al.*, 2023; YE *et al.*, 2019, 2022). A comprehensive performance comparison regarding accuracy, passivity, and computational burden highlights the effectiveness of CVF over VF. Furthermore, a parallel implementation of VF and CVF using freely available C-language libraries is demonstrated.

4.2 Admittance Synthesis

The frequency response of an N-port nodal admittance matrix $\mathbf{Y}(s) \in \mathbb{C}^{N\times N}$ can be approximated by a sum of rational functions $\overline{\mathbf{Y}}(s) \in \mathbb{C}^{N\times N}$. For the pole-residue formulation, the poles represent the system dynamics, the residues indicate the strength of each pole, and the constant terms describe the asymptotic behavior of the system. Thus,

$$\mathbf{Y}(s) \approx \overline{\mathbf{Y}}(s) = \sum_{n=1}^{N_p} \frac{\mathbf{R_n}}{s - p_n} + \mathbf{D} + s\mathbf{E}, \tag{4.1}$$

where $n = 1, 2, \ldots, N_p$; N_p is the number of poles (model order); $\mathbf{D} \in \mathbb{R}^{N\times N}$ is the constant term and $\mathbf{E} \in \mathbb{R}^{N\times N}$ is the term proportional to s, where both matrices are positive definite; p_n is the n-th pole; $\mathbf{R}_n \in \mathbb{C}^{N\times N}$ is the associated n-th residue matrix.

Irreducible quadratic terms (oscillatory modes) do not appear explicitly in (4.1), which contain only simple poles. However, they can be represented using complex-conjugate pole–residue pairs, a direct consequence of the partial fraction expansion and are mathematically equivalent to the quadratic form.

Repeated poles, which have higher-order multiplicity, are theoretically possible but uncommon in physical systems. They typically arise in degenerate and idealized scenarios involving perfectly symmetric structures, such as continuously transposed transmission lines or fully interconnected electrical networks, where all branches have the same poles and every node connects to all others and to ground (GUSTAVSEN and SEMLYEN, 2004). As noted by DESCHRIJVER and DHAENE (2007), the pole-residue basis functions of the VF (or CVF) do not account for repeated poles, as these induce severe ill-conditioning in the system equations due to rank deficiency during the pole-identification step. The spectral behavior of repeated poles can be approximated using a cluster of closely-spaced simple poles with large residues.

Equation (4.1) can be further expanded as

$$\overline{\mathbf{Y}}(s) = \begin{bmatrix} \sum\limits_{n=1}^{N_p} \frac{r_{11n}}{s-p_n} + D_{11} + sE_{11} & \cdots & \sum\limits_{n=1}^{N_p} \frac{r_{1Nn}}{s-p_n} + D_{1N} + sE_{1N} \\ \vdots & \ddots & \vdots \\ \sum\limits_{n=1}^{N_p} \frac{r_{N1n}}{s-p_n} + D_{N1} + sE_{N1} & \cdots & \sum\limits_{n=1}^{N_p} \frac{r_{NNn}}{s-p_n} + D_{NN} + sE_{NN} \end{bmatrix}, \tag{4.2}$$

where r_{mqn} is the residue associated with the transfer function from port m to q for the n-th pole, $m, q = 1, 2 \ldots N$; $D_{mq} \in \mathbb{R}$ and $E_{mq} \in \mathbb{R}$ are terms associated with the asymptotic behavior of the frequency response from port m to port q.

The expression (4.1) can be converted from the pole-residue realization to a state-space formulation (GUSTAVSEN and SEMLYEN, 1998), such as

$$\dot{\mathbf{x}}(t) = \mathbf{A}\mathbf{x}(t) + \mathbf{B}\mathbf{u}(t), \tag{4.3}$$

$$\mathbf{f}(t) = \mathbf{C}\mathbf{x}(t) + \mathbf{D}\mathbf{u}(t) + \mathbf{E}\dot{\mathbf{u}}(t), \tag{4.4}$$

where N is the number of ports; $\mathbf{A} \in \mathbb{C}^{N \cdot N_p \times N \cdot N_p}$ is the state matrix of the state-space model. In the complex modal form, $\mathbf{A}$ is strictly diagonal, with its main diagonal entries equal to the system poles. In both cases, its eigenvalues coincide with the poles of the rational model; $\mathbf{x}(t) \in \mathbb{C}^{N \cdot N_p \times 1}$ is the time-domain state variable vector; $\dot{\mathbf{x}}(t) \in \mathbb{C}^{N \cdot N_p \times 1}$ is the time derivative of $\mathbf{x}(t)$; $\mathbf{u}(t) \in \mathbb{C}^{N \times 1}$ is the input vector; $\mathbf{B} \in \mathbb{C}^{N \cdot N_p \times N}$ is a selection matrix with ones and zeros; $\mathbf{C} \in \mathbb{R}^{N \times N \cdot N_p}$ is a matrix having all $\mathbf{R_n}$; $\mathbf{f}(t) \in \mathbb{C}^{N \times 1}$ is the time-domain output vector.

Applying the Laplace transform to (4.3) and (4.4) yields

$$(s\mathbf{I} - \mathbf{A})\mathbf{X}(s) = \mathbf{B}\mathbf{U}(s), \tag{4.5}$$

$$\mathbf{F}(s) = \mathbf{C}\mathbf{X}(s) + \mathbf{D}\mathbf{U}(s) + s\mathbf{E}\mathbf{U}(s), \tag{4.6}$$

where $\mathbf{I} \in \mathbb{N}^{N \cdot N_p \times N \cdot N_p}$ is the identity matrix; $\mathbf{X}(s) \in \mathbb{C}^{N \cdot N_p \times 1}$ is the s-domain state vector; $\mathbf{F}(s) \in \mathbb{C}^{N \times 1}$ is the s-domain output vector.

By solving (4.5) for $\mathbf{X}(s)$, substituting the result into (4.6), and considering that the input $\mathbf{U}(s)$ are the voltages at boundary buses while the output $\mathbf{F}(s)$ denotes the injected currents in those buses, yields:

$$\overline{\mathbf{Y}}(s) = \mathbf{C}\left(s\mathbf{I} - \mathbf{A}\right)^{-1}\mathbf{B} + \mathbf{D} + s\mathbf{E}. \tag{4.7}$$

Similarly, the pole-residue formulation can be obtained from the state-space formulation as demonstrated in CAMPELLO *et al.* (2021).

The matrices in (4.7) are obtained using VF (or CVF) by solving, in the least squares sense, an overdetermined linear problem. The dimensions of this system are directly proportional to $N \cdot N_p$, and the complexity of the VF algorithm is at least $O(N^2)$ (CHINEA and GRIVET-TALOCIA, 2011).

4.2.1 Vector Fitting

VF is a well-known data-driven modeling technique for creating low-order rational models in the frequency domain, using frequency response samples of linear systems (TRIVERIO, 2021). It can be viewed as an enhanced reformulation of the Sanathanan-Koerner iteration with a pole-based basis (HENDRICKX and DHAENE, 2006). Electrical linear systems can have their transfer functions described by admittance, impedance, or scattering matrices (GUSTAVSEN and DE SILVA, 2013). Admittance and impedance matrices define the relationships between port voltages and currents. Scattering matrices, on the other hand, relate incident and reflected waves at ports. This representation is more common in high-speed electronics because of its improved accuracy at very high frequencies (GUSTAVSEN and DE SILVA, 2013). This section focuses on admittance-parameter modeling, as it is the common approach for power systems.

The input data for the VF framework is obtained by sampling the admittance seen between ports at several frequencies, forming $\mathbf{Y}(s_k) \in \mathbb{C}^{N \times N}$, such as

$$\mathbf{Y}(s_k) = \begin{bmatrix} Y_{11}(s_k) & \cdots & Y_{1N}(s_k) \\ \vdots & \ddots & \vdots \\ Y_{N1}(s_k) & \cdots & Y_{NN}(s_k) \end{bmatrix}, \quad k = 1, 2 \ldots, N_s, \tag{4.8}$$

where s_k is the k-th frequency sample in terms of s; $k = 1 \ldots N_s$; N_s is the number of frequency samples; $Y_{mq}(s_k)$ is the k-th frequency sample of the admittance between ports m and q.

As seen in (4.1), the VF approximates the model response $\overline{\mathbf{Y}}(s)$ to the samples $\mathbf{Y}(s)$ in the least-squares sense, using a common set of poles for all transfer functions. The problem unknowns are the residue matrices $\mathbf{R_n}$, the poles p_n, and the matrices $\mathbf{D}$ and $\mathbf{E}$. The model order N_p must be smaller than the number of samples; thus, $N_p < N_s$. Equation (4.1) is a nonlinear least-squares problem because the unknowns p_n lie in the denominator. The VF framework for solving (4.1) comprises two stages, each solved sequentially to address relaxed linearized problems.

The VF starts with an initial (guessed) set of poles $\overline{p}_n$. The first stage of the VF iterative process, known as *pole identification* (GUSTAVSEN and SEMLYEN, 1999), consists of refining a given set of $\overline{p}_n$. The linearization of (4.1) occurs by introducing a scaling rational function $\sigma(s)$ and then approximating the product $\sigma(s)\mathbf{Y}(s)$ as a rational function $\sigma\mathbf{Y}(s)$, which shares the same set of poles, such as

$$\underbrace{\left(\sum_{n=1}^{N_p} \frac{\overline{\mathbf{R}}_\mathbf{n}}{s - \overline{p}_n} + 1 \right)}_{\sigma(s)} \mathbf{Y}(s) \approx \underbrace{\left(\sum_{n=1}^{N_p} \frac{\breve{\mathbf{R}}_\mathbf{n}}{s - \overline{p}_n} + \breve{\mathbf{D}} + \mathbf{s}\breve{\mathbf{E}} \right)}_{\sigma\mathbf{Y}(s)}, \tag{4.9}$$

where $\overline{\mathbf{R}}_\mathbf{n} \in \mathbb{C}^{N \times N}$ and $\overline{z}_n \in \mathbb{C}^N$ are the n-th residue matrix and the zeroes of $\sigma(s)$, respectively; $\breve{\mathbf{R}}_\mathbf{n} \in \mathbb{C}^{N \times N}$; $\breve{\mathbf{D}} \in \mathbb{R}^{N \times N}$, and $\breve{\mathbf{E}} \in \mathbb{R}^{N \times N}$ represent the n-th residue matrix, the constant term, and the s-proportional term, respectively.

Equation (4.9) can be expressed using the following pole-zero formulation:

$$\underbrace{\left(\frac{\prod_{n=1}^{N_p}(s - \overline{z}_n)}{\prod_{n=1}^{N_p}(s - \overline{p}_n)} \right)}_{\sigma(s)} \mathbf{Y}(\mathbf{s}) \approx \underbrace{\left(\frac{\prod_{n=1}^{N_p}(s - \breve{\overline{z}}_n)}{\prod_{n=1}^{N_p}(s - \overline{p}_n)} \right)}_{\sigma\mathbf{Y}(s)}, \tag{4.10}$$

where $\overline{z}_n \in \mathbb{C}^N$ and $\breve{\overline{z}}_n \in \mathbb{C}^N$ are zeroes of $\sigma(s)$ and $\sigma\mathbf{Y}(s)$, respectively.

By isolating $\mathbf{Y}(s)$ in (4.10), $\overline{p}_n$ cancels out. Hence,

$$\mathbf{Y}(s) \approx \frac{\sigma\mathbf{Y}(s)}{\sigma(s)} = \frac{\prod_{n=1}^{N_p}(s - \overline{\overline{z}}_n)}{\prod_{n=1}^{N_p}(s - \overline{z}_n)}. \tag{4.11}$$

As a result, the zeros $\overline{z}_n$ of $\sigma(s)$ correspond to the $\overline{p}_n$ poles of $\mathbf{Y}(s)$. These zeros can be conveniently computed by solving the following eigenvalue problem:

$$\overline{z}_n = \text{eig}\left(\begin{bmatrix} \overline{p}_1 & & \\ & \ddots & \\ & & \overline{p}_{N_p} \end{bmatrix} - \begin{bmatrix} 1 \\ \vdots \\ 1 \end{bmatrix} \begin{bmatrix} \overline{\mathbf{R}}_\mathbf{1} & \cdots & \overline{\mathbf{R}}_{\mathbf{N_p}} \end{bmatrix}\right). \tag{4.12}$$

For the next iteration, the poles are updated with $\overline{z}_n$ computed in (4.12), so that $\overline{z}_n \rightarrow \overline{p}_n$. The process flips any unstable poles ($a_n < 0$) to the left complex s-plane. The algorithm repeats the pole relocation process until convergence ($\sigma(s) \approx 1$). Once the algorithm computes the dominant stable poles, the *residue identification* stage (GUSTAVSEN and SEMLYEN, 1999) entails solving an overdetermined linear least-squares problem based on (4.1) to find the unknowns $\mathbf{R_n}$, $\mathbf{D}$, and $\mathbf{E}$.

4.2.2 Complex Vector Fitting

Physical or band-pass systems exhibit real-valued impulse responses, and their spectrum inherently possesses Hermitian symmetry. That symmetry implies that the negative frequency spectrum $X(-\omega)$ equals the complex conjugate of its positive spectrum $X(\omega)$ (BOASHASH, 2003), as follows

$$X(-\omega) = X^*(\omega)\ \forall\omega, \tag{4.13}$$

where the superscript $*$ is the complex conjugate operator.

On the other hand, baseband systems present complex-valued impulse responses (KING and BRAZIL, 2017) and are thus non-physical, as complex-valued signals do not exist in the real world (GRIVET-TALOCIA and GUSTAVSEN, 2015). Nevertheless, this mathematical abstraction proves highly valuable for simulations. For example, although baseband systems do not have a direct physical interpretation, their shifted spectrum allows for a larger time-step size, without a loss of accuracy.

The synthesis of baseband systems cannot be obtained directly with the VF due to the complex conjugacy constraint imposed on VF poles and residues. This constraint forces poles and residues with nonzero imaginary parts to appear as complex conjugate pairs, such that

$$p_n = \mathrm{Re}(p_n) + j\mathrm{Im}(p_n) \text{ and } \quad p_{n+1} = \mathrm{Re}(p_n) - j\mathrm{Im}(p_n) \; \forall n, \tag{4.14}$$

$$\mathbf{R_n} = \mathrm{Re}(\mathbf{R_n}) + j\mathrm{Im}(\mathbf{R_n}) \quad \text{ and } \quad \mathbf{R_{n+1}} = \mathrm{Re}(\mathbf{R_n}) - j\mathrm{Im}(\mathbf{R_n}) \; \forall n, \tag{4.15}$$

where $\mathrm{Re}(\cdot)$ and $\mathrm{Im}(\cdot)$ is the real and imaginary parts of $(\cdot)$.

In YE *et al.* (2019), a variant of the VF framework, so-called CVF, is proposed to accommodate non-physical baseband modeling. This framework relaxes the complex conjugacy constraint, also known as the realness condition (TRIVERIO, 2021), imposed on poles and residues, allowing for more flexible modeling. Therefore, models obtained with CVF are complex-valued and produce complex-valued responses even for real-valued inputs (YE *et al.*, 2018).

CVF also incorporates improvements from VF, including the relaxation of the non-triviality constraint for enhanced convergence (GUSTAVSEN, 2006), and QR decomposition for better numerical performance (DESCHRIJVER *et al.*, 2008b).

Baseband modeling applies to electric power systems within a framework known as Shifted Frequency Analysis (ZHANG *et al.*, 2010). In this framework, voltages and currents in a power system are represented by frequency-shifted analytic signals. Similar to a frequency-dependent equivalent, such signals are inherently band-limited, offering advantages in accuracy and computational efficiency for simulations of complex electrical systems within their frequency band of interest (LIMA *et al.*, 2020). While complex-valued arithmetic increases computational and memory demands, baseband modeling reduces the maximum frequency of interest, enabling larger time-steps without compromising accuracy (ZHANG *et al.*, 2010).

Passivity Assessment

Stable time-domain simulations require both stable poles ($\mathrm{Re}(p_i) \geq 0 \; \forall i$) and a passive rational model (GUSTAVSEN, 2008a). Passivity ensures that the accumulated net energy $\mathcal{E}(t)$ remains non-negative, so the system absorbs energy without generating it, regardless of the applied excitation signal (GRIVET-TALOCIA and GUSTAVSEN, 2015). This condition can be expressed as

$$\mathcal{E}(t) = \int_{-\infty}^{t} p(\tau) d\tau \geq 0 \; \forall t, \tag{4.16}$$

where $p(\tau)$ is the instantaneous power evaluated at time τ.

A system is passive if the fitted conductance matrix $\overline{\mathbf{G}}(s) = \mathrm{Re}\left(\overline{\mathbf{Y}}(s)\right) \in \mathbb{R}^{N \times N}$ is a positive-definite matrix GUSTAVSEN and SEMLYEN (2001). This condition implies that $\overline{\mathbf{G}}(s)$ is symmetric and its eigenvalues $\lambda(s)$ satisfy:

$$\lambda(s) = \mathrm{eig}\left(\overline{\mathbf{G}}(s)\right) > 0, \tag{4.17}$$

A straightforward method to evaluate passivity involves sweeps $\lambda(s)$ for a wide frequency range. However, this approach is slow and does not guarantee sufficiently fine sampling to capture all regions where passivity violations ($\lambda(s) < 0$) occur. These regions indicate the frequencies where the equivalent model generates, rather than consumes, active power. This may cause instability in time-domain simulations, even if the rational model only contains stable poles ($\mathrm{Re}(p_n) < 0$) (GUSTAVSEN and SEMLYEN, 2001).

Analytically, the passivity violation regions can be identified through the crossover frequencies, computed via singular values (purely imaginary eigenvalues) of the Hamiltonian matrix $\mathbf{H} \in \mathbb{C}^{2N\cdot N_p \times 2N\cdot N_p}$ (YE *et al.*, 2018), where

$$\mathbf{H} = \begin{bmatrix} \mathbf{A} - \mathbf{B}(\mathbf{D}+\mathbf{D^h})^{-\mathbf{1}}\mathbf{C} & \mathbf{B}(\mathbf{D}+\mathbf{D^h})^{-\mathbf{1}}\mathbf{B^h} \\ -\mathbf{C^h}(\mathbf{D}+\mathbf{D^h})^{-\mathbf{1}}\mathbf{C} & -\mathbf{A^h} + \mathbf{C^h}(\mathbf{D}+\mathbf{D^h})^{-\mathbf{1}}\mathbf{B^h} \end{bmatrix}, \tag{4.18}$$

where the superscript **h** denotes the complex conjugate transpose operator.

The key difference between (4.18) and the Hamiltonian matrix employed in VF (GUSTAVSEN, 2008a) is the use of the complex conjugate transpose operator instead of the transpose operator, due to the complex-valued nature of systems without Hermitian symmetry (YE *et al.*, 2018). Consequently, CVF cannot use the efficient half-size singularity test used for passivity assessment in VF (GUSTAVSEN, 2008a), since it applies only to real-valued systems (YE *et al.*, 2019).

Passivity violations in a rational model may occur outside the frequency range of interest, regardless of model accuracy. Moreover, enforcing passivity may degrade the fitting of a rational model. The conditions under which passivity breaks down depend on the specific rational model. In low-order models, this issue arises from insufficient fitting precision, causing eigenvalues to poorly approximate the original eigenvalues of the frequency response. Consequently, passivity violations may occur anywhere within the fitting range. In high-order models, passivity violations may occur beyond the fitting range, as they incorporate poles with resonant frequencies outside this range, leading to uncontrolled responses (RODRÍGUEZ, 2019).

4.3 Parallelization

Although MATLAB® scripts for VF and CVF are freely available at GUSTAVSEN (2008b) and SPINA *et al.* (2021), they depend on commercial software for implementation. Parallelization strategies based on freely distributed C-language libraries were implemented to overcome this limitation.

A multi-port structure can be conceptualized as a series of interconnected yet distinct subsystems. Thus, a parallelization algorithm, whether for VF or CVF, can be applied by dividing the system into subsystems. Integrating these subsystems into a comprehensive model yields state-space realizations with increased sparsity, enabling parallel execution.

VF and CVF algorithms are implemented in C-language using LAPACK linear algebra functions from the Intel® oneAPI Math Kernel Library. This library is widely used for high-performance numerical computing and is freely accessible at INTEL (2023).

To enhance performance, the parallelism strategy in CHINEA and GRIVET-TALOCIA (2011) is adopted, which identifies QR decomposition as the most computationally intensive step of the VF, accounting for over 95% of its execution time. The same applies to CVF.

Given the nearly diagonal block structure of the matrix used in the pole identification step, QR decomposition can be executed in parallel for each block (DESCHRIJVER *et al.*, 2008b). OpenMP directives precede relevant for-loops for parallelization, requiring minimal modifications to the original code. This approach enables efficient parallel implementation of VF and CVF algorithms.

4.4 Electric Systems Under Analysis

Four test cases validate the results presented in this thesis. Case I, Case II, and Case III involve fitting scenarios concerning a power transformer, a transmission line, and a six-port frequency-dependent equivalent, respectively. These cases are easily reproducible since their frequency response data are publicly available at GUSTAVSEN (2008b), within the `VFIT3.zip` and `matrix_fitting_toolbox_1.zip` MATLAB-based packages. Case IV involves an eight-port frequency-dependent equivalent with an intricate frequency response characterized by multiple peaks and valleys. All cases involve fitting frequency-dependent admittance parameters.

4.4.1 Case I – Power Transformer

Case I fits the frequency response of the zero-sequence admittance of an 11 kV/230 V power transformer, measured at the low-voltage terminals with a resistive network connected to the high-voltage terminals (GUSTAVSEN and SEMLYEN, 1999). The frequency response consists of 401 points, ranging from 25 kHz to 4 MHz.

4.4.2 Case II – Transmission Line

Case II analyzes a 12 km, 132 kV, three-phase, overhead transmission line depicted in Fig. 4.1. The admittance matrix is computed at the beginning of the line while the end remains open-circuited, resulting in a three-port equivalent, covering 10 Hz to 100 kHz with 302 uniformly spaced points GUSTAVSEN (2008a). The dc resistance per unit length is $0.121\,\Omega\,\mathrm{km}^{-1}$ for the phase wire and $0.359\,\Omega\,\mathrm{km}^{-1}$ for the ground wire. The phase and ground wire diameters are 21.66 mm and 12.33 mm, respectively. The soil resistivity is $100\,\Omega\,\mathrm{m}$.

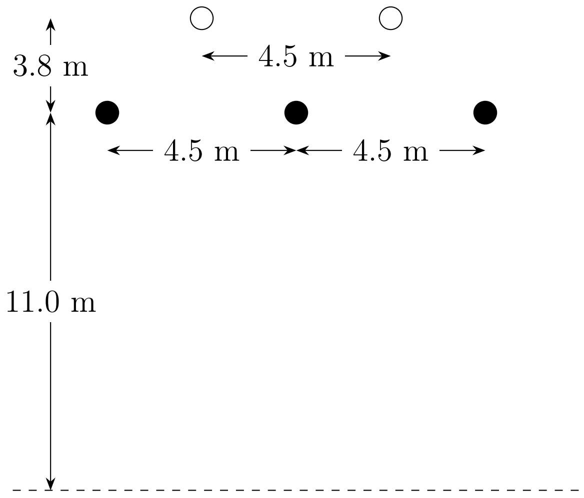

Fig. 4.1: 132 kV transmission line conductor configuration, Case II. The ground and phase wires are represented as white and black circles, respectively. Adapted from GUSTAVSEN (2008a).

4.4.3 Case III – Distribution Network

Case III pertains to a frequency-dependent equivalent of a distribution network with two three-phase terminals (A and B), as illustrated in Fig. 4.2. The model represents all lines and cables in the phase domain, incorporating frequency-dependent effects in both conductors and ground DESCHRIJVER *et al.* (2007). It has 21 unique transfer functions ($N = 6$) covering a frequency range from 10 Hz to 100 kHz, with a resolution of 334.4147 Hz ($N_s = 300$).

4.4.4 Case IV – Transmission System

Case IV refers to the transmission system depicted in Fig. 4.3. The entire system includes 107 buses, 104 transmission lines, 9 shunt branches (either capacitor or reactor banks), 67 transformers, 1 static compensator, 39 loads, and 24 synchronous generators (CAMPELLO *et al.*, 2020). The external area is modeled using an eight-port frequency-dependent equivalent, covering a frequency range from 10 Hz to 2 kHz

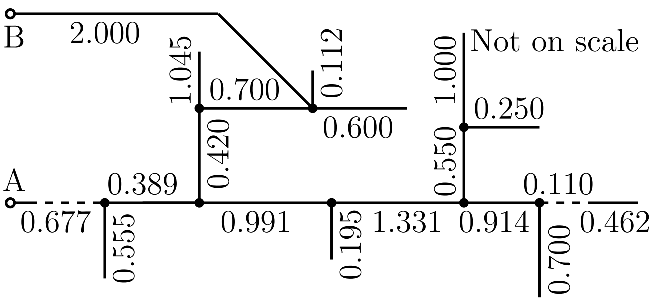

Fig. 4.2: Single-line diagram of the three-phase distribution system, Case III. The numbers are the line length in km. Continuous and dashed lines are overhead lines and underground cables, respectively. Adapted from DESCHRIJVER *et al.* (2007).

with sampling intervals of 1 Hz, totaling 1991 points, unless specified otherwise. The model encompasses 36 transfer functions of $\mathbf{Y}(s)$, with 15 of them being null. This reduces the problem to 21 unique frequency responses, similar to a six-port frequency-dependent equivalent, as the number of distinct transfer functions N_{TF} is

$$N_{TF} = \frac{N(N+1)}{2}. \tag{4.19}$$

4.5 Numerical Results and Discussion

This section highlights the main findings of the chapter. It first outlines the error metrics adopted for evaluation. Next, it provides an overview of the scenarios, called Cases, in which the fitting takes place. Additionally, it includes 1) a comparative analysis of the performance between VF- and CVF-derived models; 2) considerations regarding reduced-order models using CVF; and 3) the results of the parallelism implementation.

4.5.1 Accuracy Metrics

In this work, the accuracy of the model is evaluated using the multiple-input multiple-output versions of the Root Mean Square Error (RMSE).

The RMSE quantifies the average magnitude of errors between the fitted and reference values, providing a straightforward measure of model fitting accuracy. For fitting an admittance parameter matrix, the RMSE of $\overline{\mathbf{Y}}(s)$ is defined as:

$$\overline{Y}_{RMSE} = \sqrt{\frac{\sum_{q=1}^{N}\sum_{m=1}^{N}\sum_{k=1}^{N_S}|\overline{Y}_{mq}(s_k) - Y_{mq}(s_k)|^2}{N_{TF}N_S}}, \tag{4.20}$$

where $\overline{Y}_{mq}(s_k)$ is the fitted admittance value between ports m and q evaluated at s_k.

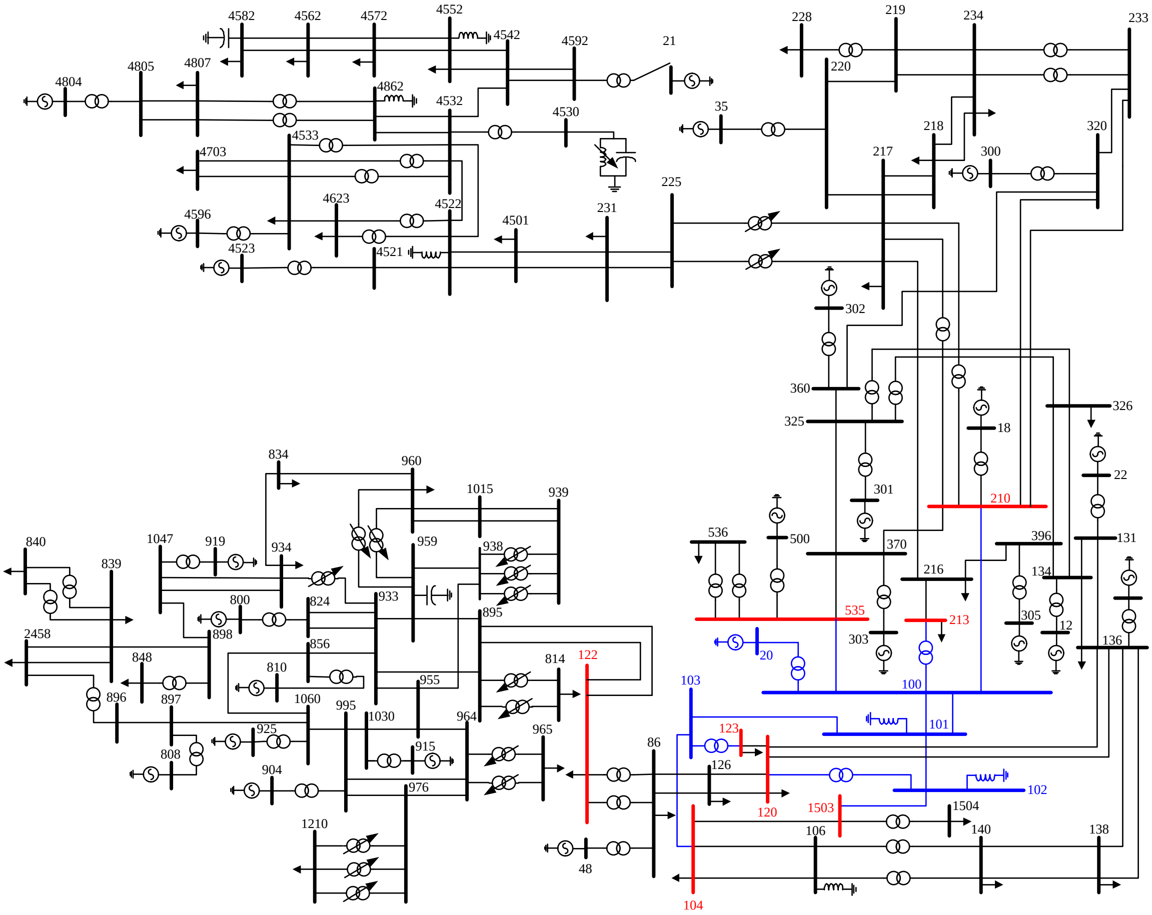

Fig. 4.3: Single-line diagram of Case IV. The external area, study area, and boundary buses are delineated in black, blue, and red, respectively. Adapted from CAMPELLO *et al.* (2020).

4.5.2 VF and CVF Performance Comparison

The performance of the rational models derived from VF and CVF will be evaluated in terms of accuracy, speed, and passivity for all cases. As mentioned in Section 4.2.2, passivity violations, if present, are identified by the singular values of $\mathbf{H}$ (analytically) or by a frequency sweep on the eigenvalues $\lambda(s)$ of $\overline{\mathbf{G}}(s)$. To ensure a fair comparison, identical parameters were employed for both VF and CVF, including the number of iterations N_{it}, N_p, and pole initialization[1], unless stated otherwise. A summary of all cases, along with the fitting parameters, is presented in Table 4.1. The iterative process halts when the RMSE shows negligible variation compared to the previous iteration (CAMPELLO *et al.*, 2020). The rational models meet the criterion for being proper ($\mathbf{D} \neq 0$ and $\mathbf{E} = 0$). Unless specified otherwise, computational tests were conducted in a MATLAB 2018a environment with a 4.4 GHz quad-core processor and 16 GB of RAM.

---

[1] Linearly-spaced complex-conjugate poles.

Table 4.1: Summary of scenarios parameters

Case	N	N_s	N_p	N_{it}
I	1	401	20	5
II	3	302	50	10
III	6	302	50	5
IV	8	1991	100	10

Case I – Power Transformer

The performance of the rational models obtained with VF and CVF for Case I is shown in Table 4.2. Regarding the fitting accuracy, the ratio of RMSE of CVF to VF was 7.53×10^{-2}. As for CPU times, those associated with CVF were 1.5 times greater than those obtained with VF. The magnitude frequency responses for both techniques are depicted in Fig. 4.4. It is noticeable that CVF achieves a lower RMSE than VF across most of the considered frequency ranges, especially around 1 MHz and 3 MHz.

Table 4.2: Comparison performance between VF and CVF, Case I

Method	RMSE (pu)	CPU time (µs)
VF	3.90×10^{-4}	160
CVF	2.94×10^{-5}	244

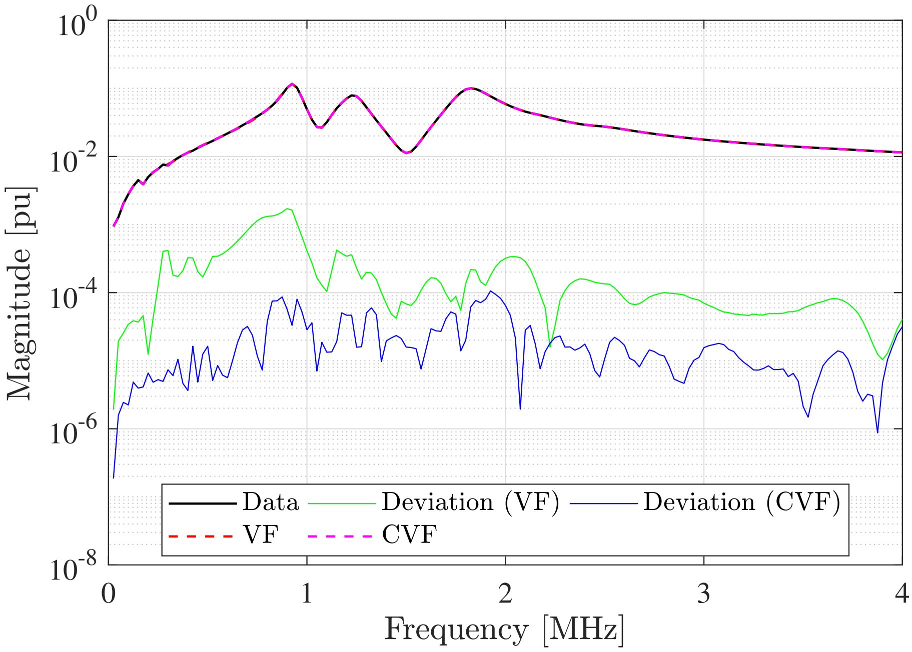

Fig. 4.4: Magnitude of the frequency response, Case I.

The 20 poles for the fitting process are presented in Fig. 4.5. All poles lie in the left half of the complex s-plane for system stability. As expected, the symmetry concerning the abscissa axis is verified only for the VF-derived model.

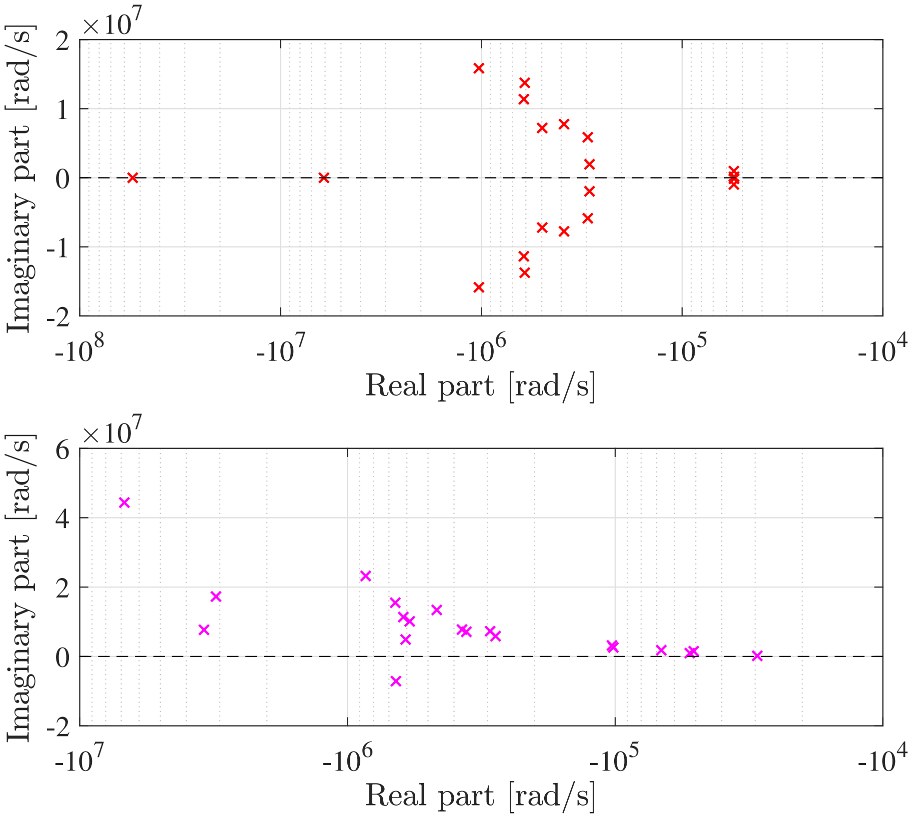

Fig. 4.5: Pole locations for the VF-derived model (top) and the CVF-derived model (bottom), Case I.

By analyzing the singular values of $\mathbf{H}$, two regions with passivity violations were identified for VF- and CVF-derived models. Table 4.3 illustrates these regions, where f_{start} and f_{end} are the starting and ending frequencies of the passivity violation region, respectively. Notably, all non-passive regions fall outside the frequency range utilized for the fitting process (25 kHz to 4 MHz). Therefore, for band-limited signals, the rational models of VF and CVF can be considered passive.

Table 4.3: Passivity violations regions, Case I

Method	Region	f_{start}	f_{end}
VF	1	0.00 Hz	18.39 kHz
	2	5.94 MHz	∞ Hz
CVF	1	0.00 Hz	8.75 kHz
	2	6.85 MHz	∞ Hz

Case II – Transmission Line

For the second case, the performance results are summarized in Table 4.4. The RMSE ratios for CVF were approximately eight orders of magnitude lower (1.39×10^{-8}) than those obtained with VF. However, the execution times for CVF were 1.9 times longer than those obtained for VF. The magnitude frequency responses are shown in Fig. 4.6. In addition to the lower RMSE, CVF exhibited significantly less deviation than VF across the entire frequency range.

Table 4.4: Comparison performance between VF and CVF, Case II

Method	RMSE (pu)	CPU time (µs)
VF	6.46×10^{-5}	207
CVF	8.97×10^{-13}	397

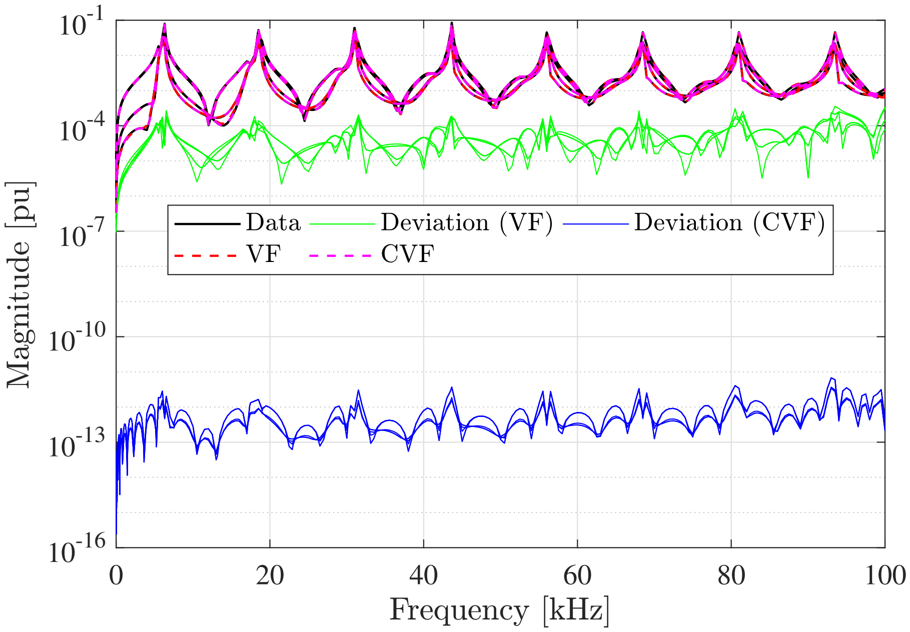

Fig. 4.6: Magnitude of the frequency response, Case II.

All poles of the VF- and CVF-derived models are located on the left-hand side of the s-plane, complying with the stability criterion, as illustrated in Fig. 4.7. Consistent with other cases, non-real poles obtained with CVF are not necessarily complex conjugate pairs.

The passivity-violations regions are detailed in Table 4.5. The fitting interval for both VF and CVF is 10 Hz to 100 kHz, covering both low- and high-frequency transients. For VF, the interval from 0 to 10 Hz in Region 1 lies outside the fitting range while Regions 2 and 3 lie within it. Notably, for CVF, the passivity violation occurs outside the frequency fitting range. Thus, the CVF-derived model can be considered passive for band-limited signals. Fig. 4.8 depicts the negative values of $\lambda(s)$,

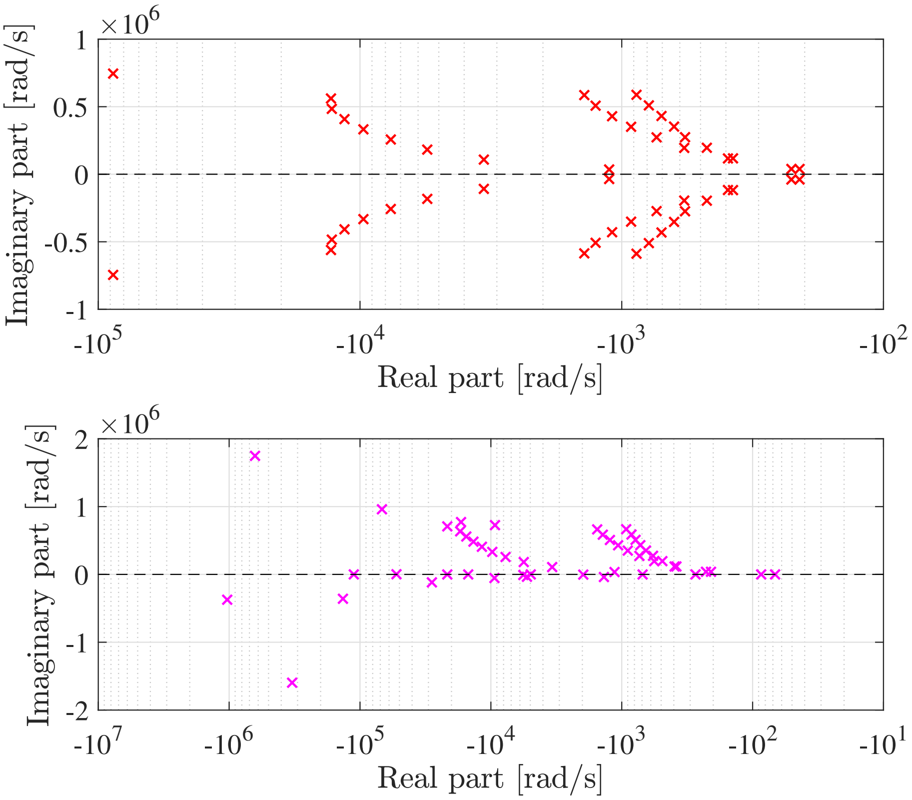

Fig. 4.7: Pole locations for the VF-derived model (top) and the CVF-derived model (bottom), Case II.

obtained from a scan with one million frequency points within the frequency fitting range. Note that all $\lambda(s)$ are real because $\overline{\mathbf{G}}_n$ is a real and symmetric matrix (GUSTAVSEN and SEMLYEN, 2001). The results shown in Fig. 4.8 are consistent with those verified in Table 4.5.

Table 4.5: Passivity violations regions, Case II

Method	Region	f_{start}	f_{end}
VF	1	0.00 Hz	395.25 Hz
	2	6.19 kHz	6.23 kHz
	3	258.56 kHz	∞ Hz
CVF	1	0.00 Hz	2.31 Hz

Case III – Distribution Network

Table 4.6 presents the fitting metrics for Case III. Like Case II, the RMSE achieved with CVF was approximately eight orders of magnitude lower (3.87×10^{-8}) than those obtained with VF. Regarding CPU times, those associated with CVF were 2.2 times greater than those obtained with VF. Fig. 4.9 shows that the RMSE of

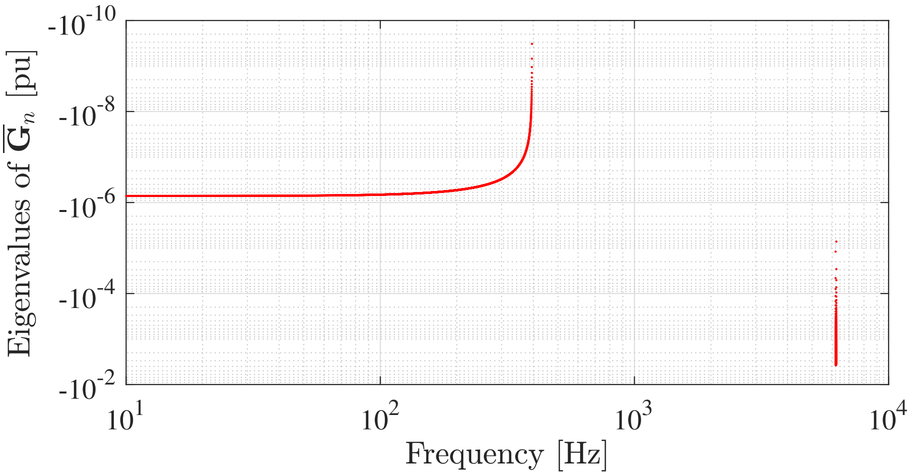

Fig. 4.8: Scanning of the negative eigenvalues of the conductance matrix using VF, Case II.

the latter is consistently smaller than that of the former across the entire considered frequency range.

Table 4.6: Comparison performance between VF and CVF, Case III

Method	RMSE (pu)	CPU time (µs)
VF	2.43×10^{-4}	134
CVF	9.39×10^{-12}	301

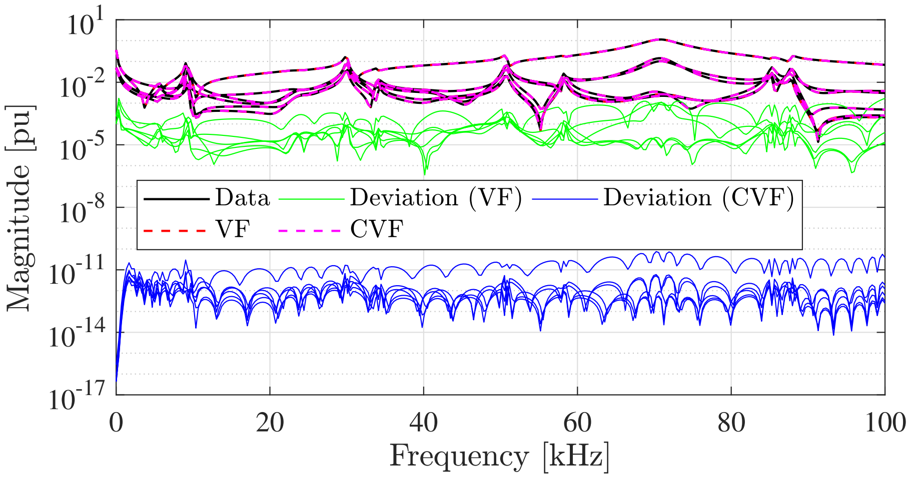

Fig. 4.9: Magnitude of the frequency response, Case III.

Fig. 4.10 illustrates that all 50 poles comply with the stability criterion and as anticipated, only the poles generated by VF are in complex conjugate pairs.

Analytically, the rational models obtained with VF and CVF exhibit two and three non-passive regions, respectively. These regions are detailed in Table 4.7.

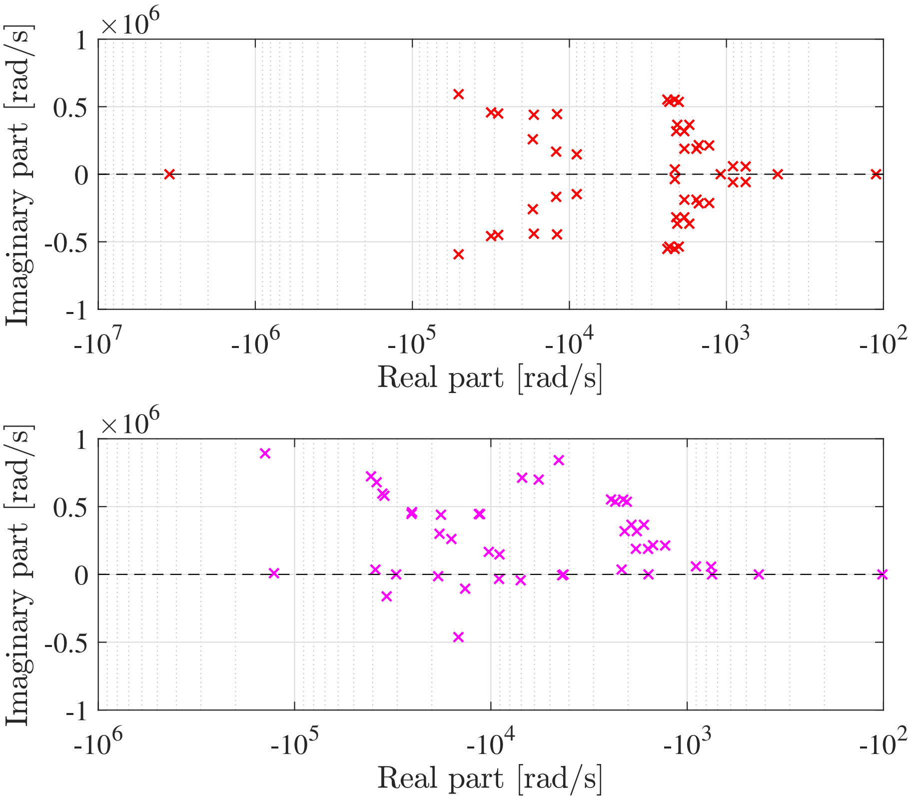

Fig. 4.10: Pole locations for the VF-derived model (top) and CVF-derived model (bottom), Case III.

The rational models exhibit the following passivity violations beyond the fitting frequency range (10 Hz to 100 kHz):

- Region 1 – from 0 Hz to 10 Hz for VF- and CVF-derived models;
- Region 2 – from 100 kHz to ∞ Hz for VF-derived model and from 100 kHz to 30.46 MHz for CVF-derived model;
- Region 3 – from 34.71 MHz to ∞ Hz for CVF-derived model.

Table 4.7: Passivity violations regions, Case III

Method	Region	f_{start}	f_{end}
VF	1	0.00 Hz	25.50 kHz
	2	28.13 kHz	∞ Hz
CVF	1	0.00 Hz	25.62 kHz
	2	28.12 kHz	30.46 MHz
	3	34.71 MHz	∞ Hz

A frequency scan is conducted on $\lambda(s)$, using one million frequency points spanning from 10 Hz to 100 kHz, and its negative values are illustrated in Fig. 4.11. These figures show that both rational models exhibit passivity violations across nearly the entire frequency range, consistent with the results outlined in Table 4.7.

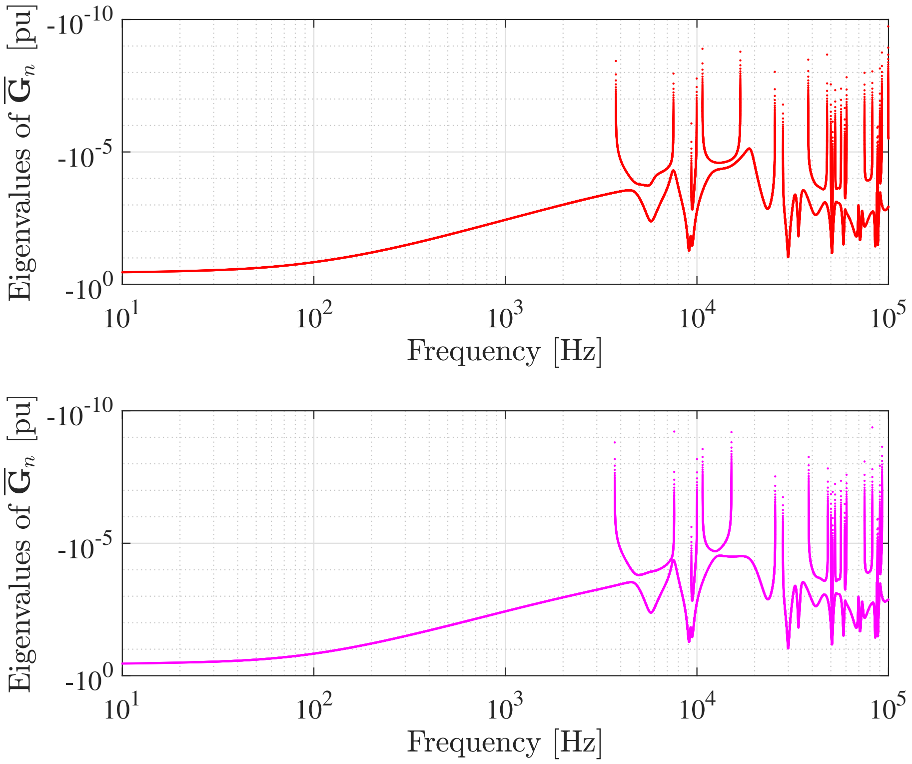

Fig. 4.11: Scanning of the negative eigenvalues of the conductance matrix using VF- (top) and CVF-derived models (bottom), Case III.

Although both techniques yield non-passive rational models within their fitting frequency range, they do not exhibit the same passivity characteristics. To illustrate this point, three passivity metrics have been developed to quantify passivity violations. The first metric, Min. $\lambda(s)$, indicates the most significant passivity violation. The second metric, Mean. $\lambda(s) < 0$, represents the average values of passivity violations. Finally, the last metric, Count $\lambda(s) < 0$, denotes the number of passivity violations. Table 4.8 presents the passivity metrics for both VF and CVF, considering the previously computed $\lambda(s)$ used to generate Fig. 4.11. Both VF and CVF exhibited similar peaks of passivity violation (first column). However, on average, CVF showed slightly more pronounced passivity violations (second column) and a narrower frequency band of passivity violation regions (third column) compared to VF.

Case IV – Transmission System

Table 4.9 presents the performance metrics for the rational models obtained with VF and CVF for Case IV. CVF achieved a RMSE of approximately three orders

Table 4.8: Passivity violations metrics, Case III

Method	Min. $\lambda(s)$	Mean $\lambda(s) < 0$	Count $\lambda(s) < 0$
VF	-3.48×10^{-1}	-3.54×10^{-3}	1.34×10^{6}
CVF	-3.48×10^{-1}	-3.57×10^{-3}	1.33×10^{6}

of magnitude lower (7.09×10^{-3}) than those obtained with VF. However, the CPU times for CVF were 2.1 times longer than those for VF. The magnitude frequency responses for VF and CVF are depicted in Fig. 4.12. These figures demonstrate that the CVF-derived model exhibits higher accuracy (i.e., lower deviation) compared to the VF-derived model across nearly the entire frequency range. Quantitatively, the accuracy metrics in Table 4.9 corroborate the observed discrepancy in error between the two rational models.

Table 4.9: Comparison performance between VF and CVF, Case IV

Method	RMSE (pu)	CPU time (µs)
VF	7.09×10^{-3}	771
CVF	5.70×10^{-1}	1653

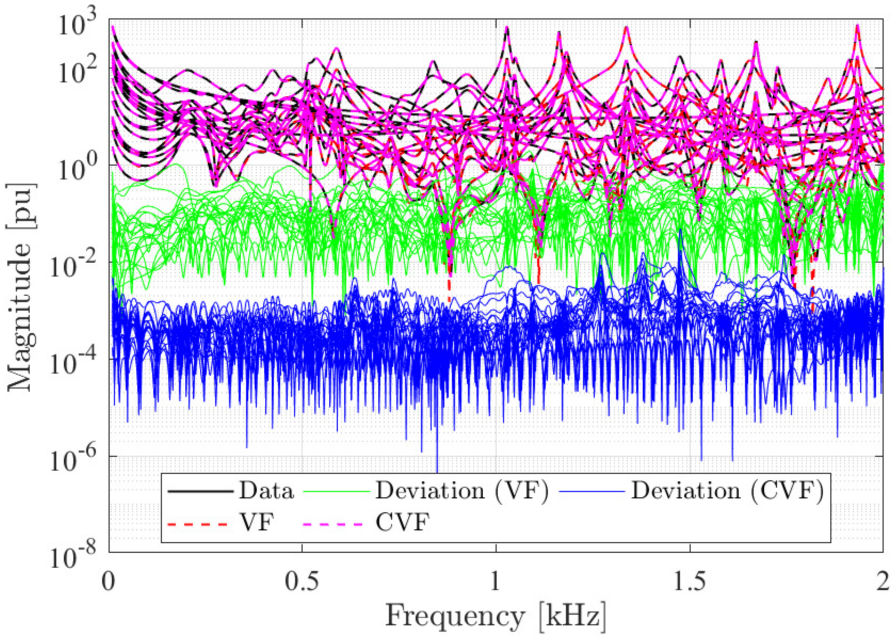

Fig. 4.12: Magnitude of frequency response, Case IV.

The resulting pole placements for VF and CVF are illustrated in Fig. 4.13. As anticipated, the poles of the former exhibit symmetry about the imaginary axis, whereas those of the latter do not.

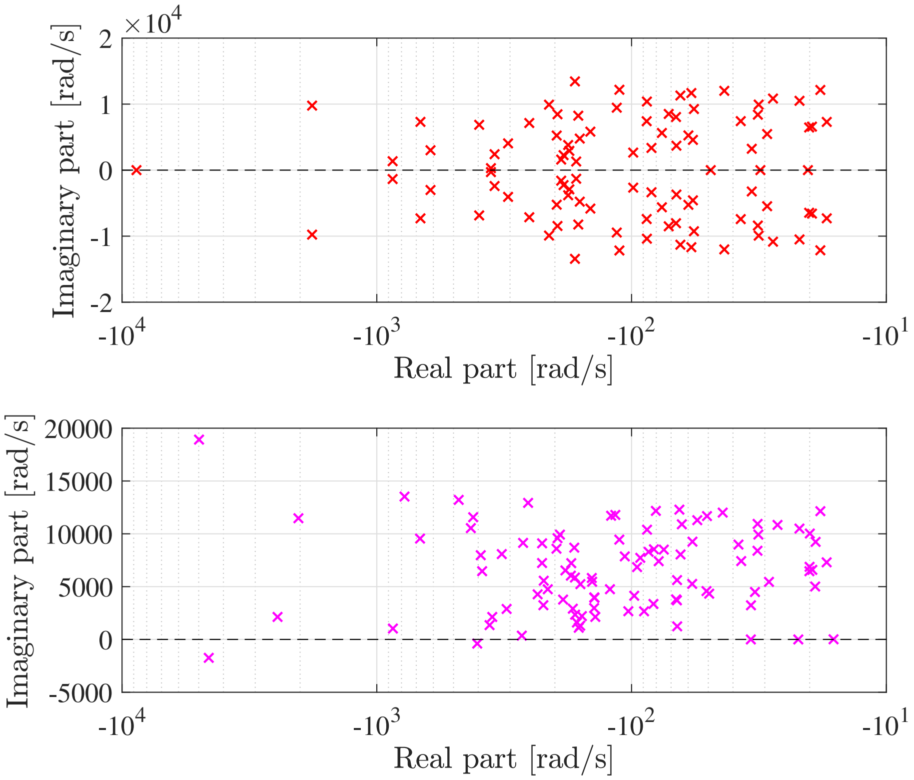

Fig. 4.13: Pole locations for the VF-derived model (top) and the CVF-derived model (bottom), Case IV.

Analytically, the synthesized equivalent models obtained with VF and CVF exhibit passivity violations across the entire fitting frequency range (10 Hz to 2 kHz). Fig. 4.14 depicts the passivity violations for VF and CVF, respectively, over a frequency sweep of $\lambda(s)$ ranging from 10 Hz to 2 kHz, with 10 000 frequency points. The CVF-derived model exhibited smaller, yet noticeable, passivity violations than the VF-derived model across the passivity metrics provided in Table 4.10.

Table 4.10: Passivity violations metrics

Method	Min. $\lambda(s)$	Mean $\lambda(s) < 0$	Count $\lambda(s) < 0$
VF	-2914.4	-39.656	25 501
CVF	-2889.6	-39.650	25 524

4.5.3 Model-order Reduction

CVF consistently reduced the RMSE compared to the VF across all cases shown in Section 4.5.2. Thus, the CVF-derived model can undergo a model-order reduction procedure to achieve similar accuracy to that of VF. This section presents the performance analysis for the most challenging scenario: Case IV.

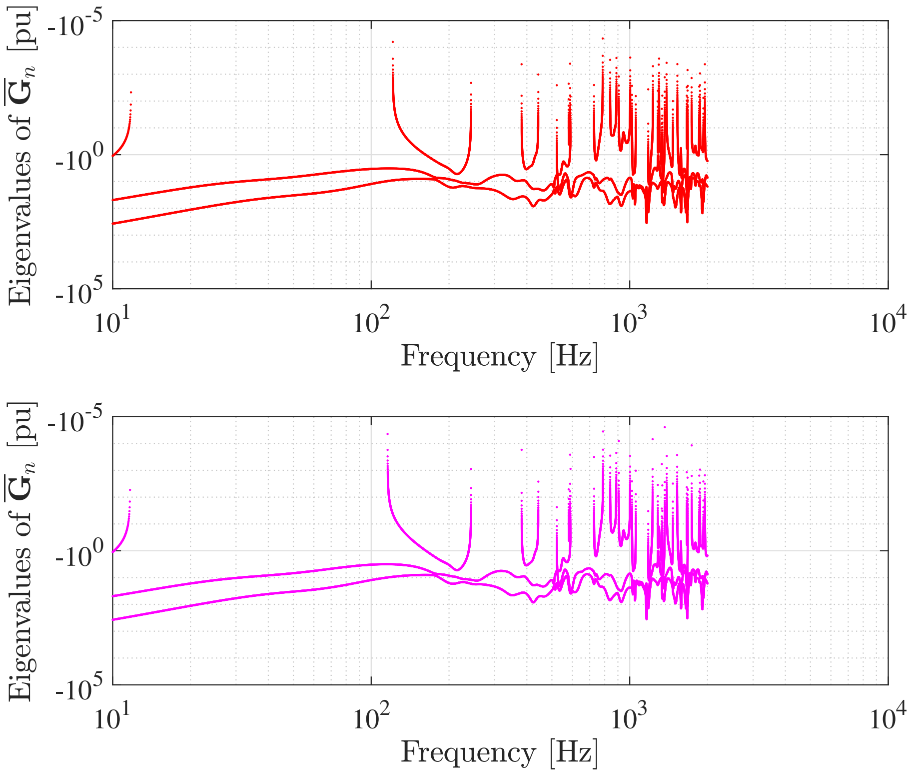

Fig. 4.14: Passivity of $\overline{\mathbf{G}}(s)$ using VF (top) and CVF (bottom) rational models, Case IV.

From an optimization standpoint, relaxing the complex conjugate constraint streamlines the optimization problem by increasing the solution search space. The effective number of variables for the VF (N_{VVF}) is

$$N_{VVF} = N_{RP} + \frac{N_{CP}}{2}, \tag{4.21}$$

where N_{RP} and N_{CP} denote the number of real and complex conjugate poles.

For VF, the N_{CP} is divided by two in (4.21), because complex poles must occur in complex conjugate pairs. In contrast, the effective number of variables for CVF N_{VCVF} is

$$N_{VCVF} = N_{RP} + N_{CP}. \tag{4.22}$$

The RMSE as a function of N_p is illustrated in Fig. 4.15, where $25 \leq N_p \leq 500$, in increments of 25. This depiction shows that the RMSEs attained with CVF are noticeably lower than those associated with VF for $25 \leq N_p \leq 300$. Both methodologies show similar RMSE values for $N_p \geq 325$.

Fig. 4.16 illustrates that the computational times required for both techniques increase nonlinearly with N_p. Additionally, CVF was consistently slower than VF for the same N_p. This discrepancy arises because $N_{VCVF} > N_{VVF}$ when complex poles are employed.

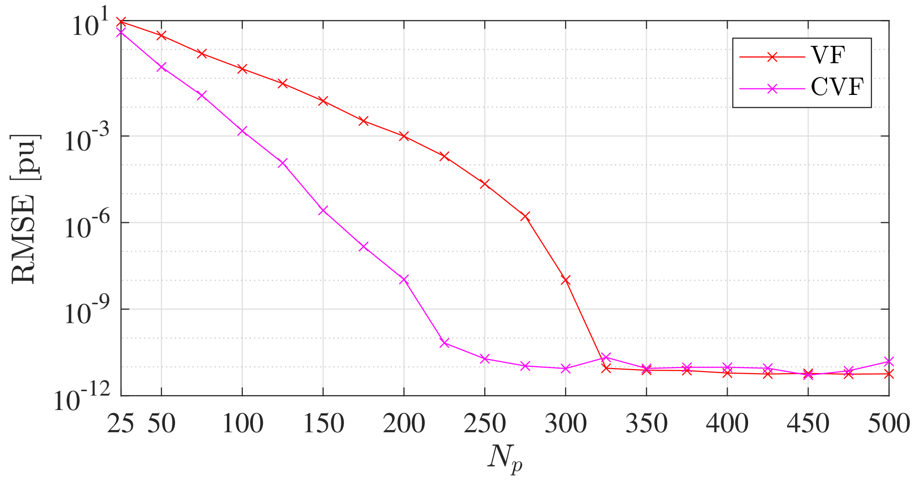

Fig. 4.15: RMSE vs model order for VF and CVF.

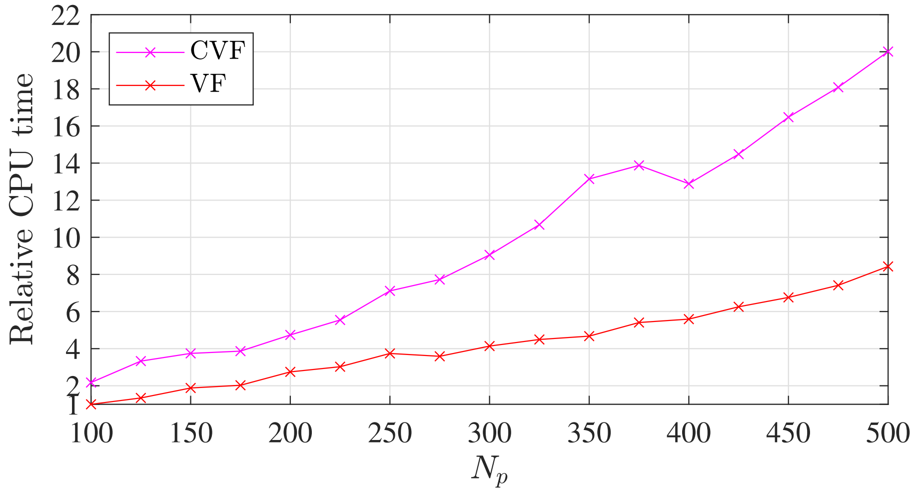

Fig. 4.16: Relative CPU time vs model order for VF and CVF, Case IV. Results are scaled to the CPU time of the VF with $N_p = 100$.

Specifically, $N_{VVF} = 52$ (with $N_{RP} = 4$ and $N_{CP} = 96$) and $N_{VCVF} = 100$ (with $N_{RP} = 0$ and $N_{CP} = 100$). To simplify the mathematical model while preserving its core characteristics, a model-order reduction is applied to the CVF-derived model, reducing N_p from 100 to 52 (with $N_{RP} = 4$ and $N_{CP} = 48$). Theoretically, the maximum achievable model-order reduction using CVF is 50%, when the rational model contains only complex poles. The results in Table 4.11 highlight that CVF achieves comparable performance to VF, despite having a reduced order.

The results depicted in Fig. 4.17 compare the magnitude frequency response of $\overline{Y}_{1,1}(s)$ obtained using VF ($N_p = 100$) and CVF ($N_p = 52$). There is consistent agreement across all frequencies between the fitting obtained with VF and CVF, despite the reduced order of the latter.

Table 4.11: Comparison between VF and CVF with model-order reduction, Case IV

Method	N_p	RMSE (pu)	$\frac{\text{RMSE CVF}}{\text{RMSE VF}}$	$\frac{\text{CPU time CVF}}{\text{CPU time VF}}$
VF	100	2.13×10^{-1}	–	–
CVF	52	2.11×10^{-1}	0.99	1.1

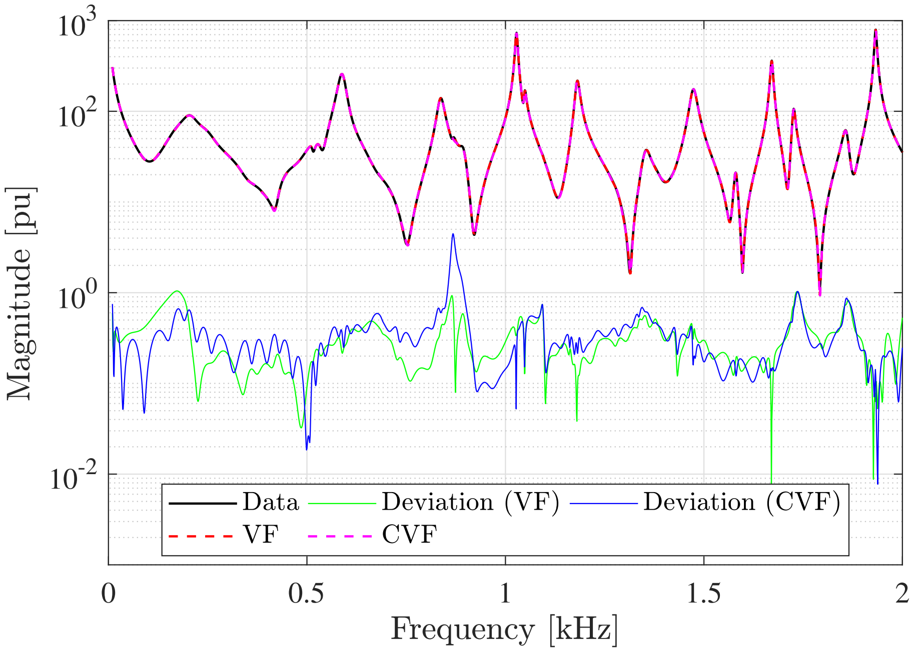

Fig. 4.17: Magnitude of frequency response for the element $\overline{Y}_{1,1}$ using a different number of poles for VF and CVF, Case IV.

4.5.4 Parallelism

The CVF implementation introduces a trade-off: it enhances accuracy but slows the fitting process. To overcome this issue, Parallel Vector Fitting (PVF) and Parallel Complex Vector Fitting (PCVF) were implemented in C-language using the methodology described in Section 4.3. In this section, the numerical computations were executed on a more powerful PC, containing an 8-core Ryzen 7 5800X @ 3.80 GHz with 16 GB of RAM, to reduce thread bottlenecks.

Eighteen new cases (Case IV-A, Case IV-B, . . ., Case IV-R) were employed to investigate the scalability of the proposed methodology. These cases are based on Case IV and were generated by altering the number of poles ($100 \leq N_p \leq 300$), the effective number of ports ($2 \leq N \leq 6$), and the frequency samples ($1991 \leq N_s \leq 19\,991$).

Table 4.12 summarizes the performance results of the MATLAB® scripts (for VF and CVF) and the proposed implementation (for PVF and PCVF). Notably, MATLAB® has multi-threaded linear algebra and numerical functions such as *eig*,

Table 4.12: Summary of the computational performance for VF, PVF, CVF, and PCVF, considering one iteration

Case	N_p	N	N_s	VF[1] (s)	PVF[2] (s)	Speed-up[3]	CVF[1] (s)	PCVF[2] (s)	Speed-up[4]
IV–A	100	2	1991	0.18	0.06	3.00	0.28	0.15	1.87
IV–B	100	4	1991	0.28	0.17	1.65	0.80	0.46	1.74
IV–C	100	6	1991	0.64	0.36	1.78	1.52	0.91	1.67
IV–D	200	2	1991	0.32	0.16	2.00	0.77	0.43	1.79
IV–E	200	4	1991	0.81	0.45	1.80	2.28	1.31	1.74
IV–F	200	6	1991	1.68	0.93	1.81	4.51	2.68	1.68
IV–G	300	2	1991	0.55	0.30	1.83	1.51	0.87	1.74
IV–H	300	4	1991	1.58	0.88	1.80	4.52	2.77	1.63
IV–I	300	6	1991	2.94	1.75	1.68	8.98	5.70	1.58
IV–J	100	2	19 991	1.20	0.50	2.40	2.41	1.39	1.73
IV–K	100	4	19 991	2.52	1.40	1.80	6.74	4.85	1.39
IV–L	100	6	19 991	4.92	2.97	1.66	13.40	8.65	1.55
IV–M	200	2	19 991	2.70	1.43	1.89	8.10	4.82	1.68
IV–N	200	4	19 991	6.70	4.36	1.54	21.54	14.95	1.44
IV–O	200	6	19 991	13.58	8.78	1.55	43.65	30.50	1.43
IV–P	300	2	19 991	5.55	2.97	1.87	16.22	10.61	1.53
IV–Q	300	4	19 991	13.86	8.77	1.58	45.58	32.17	1.42
IV–R	300	6	19 991	29.89	17.90	1.67	90.68	68.75	1.32

[1] MATLAB® implementation.
[2] Proposed implementation.
[3] Computed by VF/PVF.
[4] Computed by CVF/PCVF.

svd, and *sort* since version R2008a (MATHWORKS, 2023).

Three main observations emerge upon analyzing the effects of individually increasing N_p, N, or N_s in Table 4.12. First, execution times grew alongside these variables. This behavior is expected, as the computational complexity scales quadratically with the number of poles and linearly with the number of transfer functions (4.19), frequency samples, and iterations (CHINEA and GRIVET-TALOCIA, 2011).

Second, the speed-up observed for most PVF and PCVF cases was more pronounced for smaller N_p, N, or N_s. For instance, when comparing Case IV–A with Case IV–C (where N increases from 2 to 6), the speed-up (VF/PVF) decreases from 3.00 to 1.78. Similarly, comparing Case IV–E with Case IV–N (where N_s increases from 1991 to 19991), the speed-up (CVF/PCVF) decreases from 1.74 to 1.44. Also, when comparing Case IV–A with Case IV–G (where N_p increases from 100 to 300), the speed-up (VF/PVF) decreases from 3.00 to 1.83. In such instances, more mathematical operations are required. Thus, communication overhead between parallel processes can cause dependency bottlenecks that limit parallelization efficiency.

Finally, parallelization consistently reduced CPU times across all cases. In worst-case scenarios, Case IV–N and Case IV–R, speed-up reached 1.54 (VF/PVF) and 1.32 (CVF/PCVF), respectively. Conversely, the best-case scenario (Case IV–A) yielded speed-up values of 3.00 (VF/PVF) and 1.87 (CVF/PCVF).

4.6 General Remarks

Regarding computational burden, CVF consistently required longer execution times than VF in all cases. This behavior is anticipated since, for the same N_p, CVF involves additional variables due to the relaxation of the complex conjugate pairs constraint on poles and residues when employing complex poles, resulting in $N_{VCVF} > N_{VVF}$. The increase in computational time during the CVF fitting process becomes more pronounced for larger and more intricate systems since more poles are needed for proper fitting, as seen in Fig. 4.16.

Regarding passivity, CVF exhibited different characteristics than VF due to the use of distinct poles and residues in the modeling process. Notably for Case II, CVF produced a passive model, whereas VF did not.

CVF can achieve accuracy comparable to VF while employing fewer poles (up to 50%). The results in Section 4.5.3 demonstrate that even with a 48% reduction in model order, CVF maintained the fitting accuracy and computational performance similar to VF.

Finally, the parallel implementations of VF and CVF (PVF and PCVF) in C using LAPACK and OpenMP directives enhanced computational speed across all tested cases. Furthermore, it eliminates the necessity to depend on proprietary software such as MATLAB®.

This chapter demonstrated that CVF can enhance the accuracy in the frequency domain. The next chapter will present methodologies to improve the accuracy in the time domain.

Chapter 5

Strategies for Frequency-Warping Mitigation

This chapter builds on the demonstration of frequency warping errors in Chapter 3 and the enhanced rational modeling flexibility and accuracy achieved through CVF in Chapter 4, presenting novel strategies to reduce frequency warping by directly compensating the poles and residues of existing rational models. The work presented here incorporates and expands upon the research presented in PAPER#3 and PAPER#4, following the nomenclature introduced in Section 1.3.

5.1 Introduction

The increasing complexity of power systems is accelerated by the energy transition from fossil-based to low-carbon and renewable sources (GONZALEZ-LONGATT, 2015). As a result, in-depth analysis of new dynamic interactions between their components and subsystems is crucial (JI and XING, 2023). In this context, EMT simulations are an essential tool that can be tuned to provide sufficient accuracy to anticipate the new dynamics within modern power grids, ensuring reliable and efficient power system planning and operation. Therefore, the need for accurate and reliable simulations is paramount.

Time-domain simulations require careful consideration regarding discretization techniques. The trapezoidal rule is widely employed in commercial EMT-type simulators (AMETANI, 2015) due to its superior accuracy among linear multi-step integration methods with A-stability (DAHLQUIST, 1963). The nonlinear frequency mapping between the analog and digital frequencies compresses the discrete-time frequency scale, introducing the frequency warping error (BRAMBILLA and STORTI-GAJANI, 2003). Frequency warping is not unique to the trapezoidal rule but affects all linear multi-step integration methods (YANG *et al.*, 2009). Chapter 3 showed how frequency warping degrades the accuracy of time-domain simulations. This degradation results from the distortion of the discretized behavior of inductances and capacitances.

Accurate time-domain simulations require high-fidelity modeling of power system components, including lines, cables, power electronic devices, transformers, switchgear, generators, and loads. Such modeling must capture the dynamic behavior of these components over a broad frequency spectrum. However, a detailed representation of all components in large-scale power systems is computationally prohibitive for EMT studies. To address this challenge, frequency-dependent equivalents approximated by rational functions are widely used to enable accurate and efficient time-domain simulations while preserving frequency behavior beyond the grid frequency (GRIVET-TALOCIA and GUSTAVSEN, 2015). In that regard, Chapter 4 demonstrated that CVF yields more accurate representations of frequency-dependent equivalents than VF for the same model order. This improvement stems from the increased flexibility in the pole relocation step, achieved by removing the realness constraint of the rational model.

5.2 The Pole-Residue Compensation Algorithm

As discussed in Chapter 3, solving the differential network equations using the trapezoidal rule method introduces frequency-dependent behavior in capacitances and inductances due to frequency warping (DOMMEL, 1995). Hence,

$$L_{DT} = \Psi L, \tag{3.20}$$

$$\Psi = \frac{2}{\omega h}\tan\left(\frac{\omega h}{2}\right), \tag{3.21}$$

$$C_{DT} = \Psi C. \tag{3.25}$$

In the discrete-time domain, the expected (analog) behavior of inductors and capacitors for a target frequency ω' (the pre-warping frequency) can be retrieved by scaling L_{DT} in (3.20) and C_{DT} in (3.25) for a factor ξ.

Hence,

$$\xi = \frac{1}{\Psi} = \frac{\omega' h}{2}\cot\left(\frac{\omega' h}{2}\right), \tag{5.1}$$

$$L' = \xi L_{DT} = \frac{\omega' h L_{DT}}{2}\cot\left(\frac{\omega' h}{2}\right), \tag{5.2}$$

$$C' = \xi C_{DT} = \frac{\omega' h C_{DT}}{2}\cot\left(\frac{\omega' h}{2}\right), \tag{5.3}$$

where L' and C' are the frequency-warped-compensated inductance and capacitance, respectively.

Consider a single entry of $\overline{\mathbf{Y}}(s)$, $\overline{Y}(s)$, where its pole-residue formulation is given by (3.33):

$$\overline{Y}(s) = \sum_{i=1}^{N_p} \frac{r_i}{s - p_i} + D + sE. \tag{3.33}$$

$\overline{Y}(s)$ can be synthesized using basic circuit components such as resistors, inductors, and capacitors (GUSTAVSEN, 2002), as shown in Fig. 5.1. The equivalent network depicted in that figure has the following admittance:

$$\overline{Y}(s) = \underbrace{\sum_{j=1}^{N_{RP}} \frac{1}{R_j + sL_j}}_{\text{Real poles}} + \underbrace{\sum_{k=1}^{N_{CP}} \frac{1}{R_k + sL_k + \dfrac{1}{sC_k + G_k}}}_{\text{Complex poles}} + \underbrace{\frac{1}{R_0}}_{D} + s\underbrace{C_0}_{E}. \tag{5.4}$$

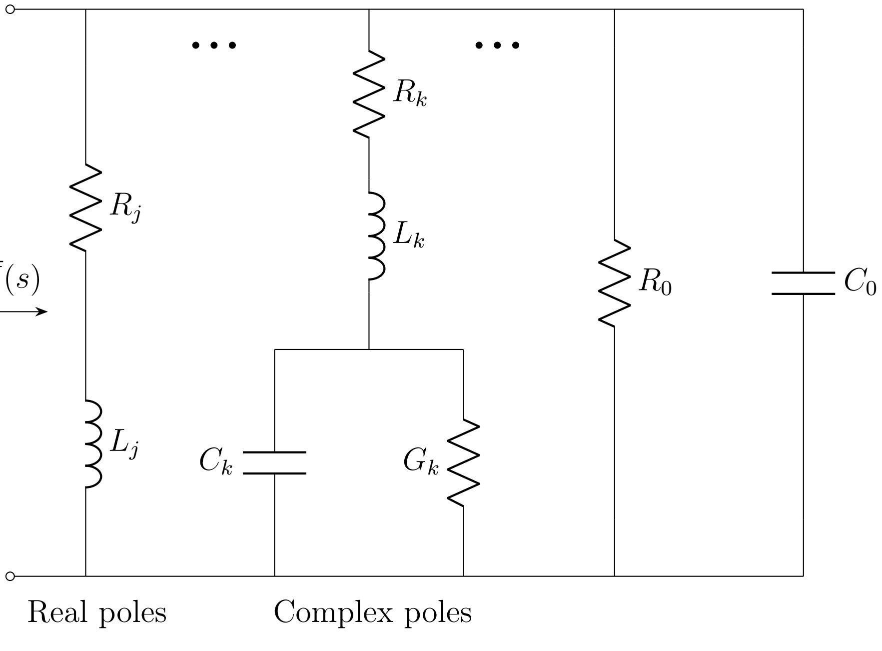

Fig. 5.1: Electrical network synthesis. Adapted from (GUSTAVSEN, 2002).

Effect of the Pre-warping on Real Poles

Each real pole (and its residue) of a rational model can be represented by an RL branch (GUSTAVSEN, 2002). Since frequency warping does not affect resistances, compensation is applied only to the inductances. Consider a rational model with a single real pole represented by R_1 and L_1, such that:

$$Y(s) = \frac{1}{R_1 + sL_1}. \tag{5.5}$$

The root of the denominator of (5.5) is the pole p, thus,

$$p = \frac{-R_1}{L_1}. \tag{5.6}$$

The corresponding residue r of $Y(s)$ in (5.5) is:

$$r = \lim_{s \to p}(s-p)Y(s) = \lim_{s \to \frac{-R_1}{L_1}} \frac{s + \dfrac{R_1}{L_1}}{R_1 + sL_1}. \tag{5.7}$$

As both numerator and denominator of the right-hand side of (5.7) approach zero as s tends to $\frac{-R_1}{L_1}$, the limit becomes indeterminate. Thus,

$$r = \lim_{s \to \frac{-R_1}{L_1}} \frac{\dfrac{d}{ds}\left(s + \dfrac{R_1}{L_1}\right)}{\dfrac{d}{ds}\left(R_1 + sL_1\right)} = \frac{1}{L_1}. \tag{5.8}$$

Consider that L_1 is pre-warped by ξ, so the frequency-warped-compensated admittance is

$$Y'(s) = \frac{1}{R_1 + sL_1'} = \frac{1}{R_1 + s\xi L_1}. \tag{5.9}$$

The new frequency-warped-compensated pole p' of $Y'(s)$ is:

$$p' = \frac{-R_1}{\xi L_1} = \frac{p}{\xi}. \tag{5.10}$$

Now, the frequency-warped-compensated residue of $Y'(s)$ is:

$$r' = \lim_{s \to p'}(s-p')Y(s) = \lim_{s \to \frac{-R_1}{\xi L_1}} \frac{s + \dfrac{R_1}{\xi L_1}}{R_1 + s\xi L_1}. \tag{5.11}$$

The limit in (5.11) is indeterminated, thus:

$$r' = \lim_{s \to \frac{-R_1}{\xi L_1}} \frac{\dfrac{d}{ds}\left(s + \dfrac{R_1}{\xi L_1}\right)}{\dfrac{d}{ds}\left(R_1 + s\xi L_1\right)} = \frac{1}{\xi L_1} = \frac{r}{\xi}. \tag{5.12}$$

In conclusion, if L_1 is scaled by ξ, both the corresponding pole and residue are scaled by $1/\xi$.

Effect of the Pre-warping on Complex Poles

Consider the complex pole-residue modeled using an RLCG branch (GUSTAVSEN, 2002) depicted in Fig. 5.1. Therefore, frequency warping can be reduced by updating $L \leftarrow L'$ (5.2) and $C \leftarrow C'$ (5.3). Thus,

$$Y(s) = \frac{1}{R_1 + sL_1 + \dfrac{1}{sC_1 + G_1}} = \frac{sC_1 + G_1}{s^2 L_1 C_1 + s(R_1 C_1 + L_1 G_1) + R_1 G_1 + 1}, \quad (5.13)$$

The roots of $Y(s)$ in (5.13) are its poles p, so:

$$p = \frac{-K \pm \sqrt{K^2 - 4L_1 C_1 (R_1 G_1 + 1)}}{2L_1 C_1}, \quad (5.14)$$

where $K = R_1 C_1 + L_1 G_1$.

The corresponding residue r of (5.13) is:

$$r = \lim_{s \to p} (s - p) Y(s) = \lim_{s \to p} (s - p) \frac{sC_1 + G_1}{s^2 L_1 C_1 + sK + R_1 G_1 + 1}, \quad (5.15)$$

The limit in (5.15) is indeterminate, thus:

$$\begin{aligned} r = \lim_{s \to p} \frac{\dfrac{d}{ds}\left[(s - p)(sC_1 + G_1)\right]}{\dfrac{d}{ds}\left(s^2 L_1 C_1 + sK + R_1 G_1 + 1\right)} &= \lim_{s \to p} \frac{(s - p)C_1 + (sC_1 + G_1)}{2sL_1 C_1 + K} \\ &= \frac{pC_1 + G_1}{2pL_1 C_1 + K}. \end{aligned} \quad (5.16)$$

A frequency-warped-compensated version of (5.13), denoted as $Y'(s)$, can be obtained by substituting L_1 and C_1 with their corresponding pre-warped versions. Hence,

$$Y'(s) = \frac{1}{R_1 + sL_1' + \dfrac{1}{sC_1' + G_1}}, \quad (5.17)$$

By substituting (5.2) and (5.3) in (5.17) yields:

$$Y'(s) = \frac{1}{R_1 + s\xi L_1 + \dfrac{1}{s\xi C_1 + G_1}} = \frac{s\xi C_1 + G_1}{s^2 \xi^2 L_1 C_1 + s\xi K + R_1 G_1 + 1}. \quad (5.18)$$

The poles p' of $Y'(s)$ are the roots of its denominator, hence:

$$\begin{aligned} p' &= \frac{-\xi K \pm \sqrt{(\xi K)^2 - 4\xi^2 L_1 C_1 (R_1 G_1 + 1)}}{2\xi^2 L_1 C_1}, \\ &= \frac{-K \pm \sqrt{K^2 - 4 L_1 C_1 (R_1 G_1 + 1)}}{2\xi L_1 C_1}. \end{aligned} \tag{5.19}$$

Thus, by expressing (5.19) in terms of (5.14) leads to:

$$p' = \frac{p}{\xi}. \tag{5.20}$$

The corresponding residue r' associated with p' is:

$$r' = \lim_{s \to p'} (s - p') Y'(s) = \lim_{s \to p'} \frac{(s - p')(s\xi C_1 + G_1)}{s^2 \xi^2 L_1 C_1 + s\xi K + R_1 G_1 + 1}. \tag{5.21}$$

Therefore,

$$\begin{aligned} r' = \lim_{s \to p'} \frac{\dfrac{d}{ds}\left[(s - p')(s\xi C_1 + G_1)\right]}{\dfrac{d}{ds}\left(s^2 \xi^2 L_1 C_1 + s\xi K + R_1 G_1 + 1\right)} &= \lim_{s \to p'} \frac{(s - p')C_1 + (s\xi C_1 + G_1)}{2s\xi^2 L_1 C_1 + \xi K} \\ &= \frac{p'\xi C_1 + G_1}{2p'\xi^2 L_1 C_1 + \xi K}. \end{aligned} \tag{5.22}$$

By substituting (5.20) in (5.22) results in:

$$r' = \frac{p C_1 + G_1}{2p\xi L_1 C_1 + \xi K}. \tag{5.23}$$

Finally, replacing (5.16) in (5.23) results in:

$$r' = \frac{r}{\xi}. \tag{5.24}$$

The scaling of L_1 and C_1 by ξ implies scaling of p' and r' by $1/\xi$.

Effect of the Pre-warping on the Asymptotic Terms

The result of the pre-warping in D is straightforward as it is not affected by frequency warping, thus

$$D' = D_0 = \frac{1}{R_0}. \tag{5.25}$$

Although the poles and residues were scaled by the factor $1/\xi$, the frequency-warped-compensated value of E, denoted as E', is

$$E' = sC'_0 = s\xi C_0, \tag{5.26}$$

where C'_0 is the frequency-warped-compensated C_0.

E' represents a frequency-dependent contribution. Thus, compensating this term for frequency warping is only feasible for a specific frequency of interest, not the entire frequency range. Therefore, the PRC is better suited to strictly proper rational models, where $D \neq 0$ and $E = 0$.

Pre-warped Rational Model

The strictly proper multiple-input multiple-output form of $\overline{Y'}(s)$ is given by

$$\overline{\mathbf{Y}'}(s) = \sum_{i=1}^{N_p} \frac{\mathbf{r'_i}}{s - p'_i} + \mathbf{D}, \tag{5.27}$$

where $\mathbf{r'_i}$ is the pre-warped residue matrix associated with the i-th pole.

5.2.1 The Proposed Algorithm

The challenge lies in selecting an appropriate value for ω' to effectively reduce the frequency warping. In the ideal scenario, the simulated signal contains a single known frequency component, which allows setting ω' accordingly and fully eliminating frequency warping. However, this scenario is seldom encountered in EMT simulations. Moreover, the exact frequency content of a transient response is typically unknown a priori. Therefore, an effective compensation strategy should neither require prior spectral knowledge nor assume a single-tone signal.

Frequency warping manifests as a disturbance of the original linearized eigenvalues of the simulated system (BRAMBILLA and STORTI-GAJANI, 2003). While these eigenvalues are typically unknown, frequency response data sampled between ports can be acquired through measurements or simulations. As a result, the equivalent system and its eigenvalues can be approximated (identified) with a rational model using data-driven curve-fitting techniques (GRIVET-TALOCIA and GUSTAVSEN, 2015), such as the VF and CVF presented in Chapter 4.

Following system identification, the proposed Pole-Residue Compensation (PRC) algorithm compensates the poles and residues of a rational model to compensate for the eigenvalue perturbations caused by frequency warping. The method establishes a direct mapping between discrete and continuous-time domains for both poles and residues.

Pseudocode 1 presents the PRC algorithm, which uses the imaginary components of the system poles as pre-warping frequencies due to their role in oscillatory dynamics. Each pole-residue pair, p_i in (5.20) and $\mathbf{r_i}$ (5.24), scales according to its pre-warping frequency ω'_i, defined as:

$$\omega'_i = \mathrm{Im}(p_i)\ \forall i, \tag{5.28}$$

where $\mathrm{Im}(p_i)$ is the imaginary frequency component of p_i.

Pseudocode 1 The PRC algorithm

```
for all $i$ do                                        ▷ All poles
$\omega'_i \leftarrow \mathrm{Im}(p_i)$                                 ▷ Eq. (5.28)
    if $|\omega'_i| < \pi/h$ then                             ▷ Nyquist limit
        $\xi_i \leftarrow (\omega'_i h/2)\cot(\omega'_i h/2)$                   ▷ Eq. (5.1)
        $p'_i \leftarrow p_i/\xi_i$                                 ▷ Eq. (5.20)
        $\mathbf{r'_i} \leftarrow \mathbf{r_i}/\xi_i$                                 ▷ Eq. (5.24)
    end if
end for
```

Figure 5.2 illustrates the PRC framework as a post-processing step for frequency warping compensation. This approach enables frequency warping compensation of existing rational models, making it particularly valuable in closed-box modeling scenarios where the original frequency response data is inaccessible.

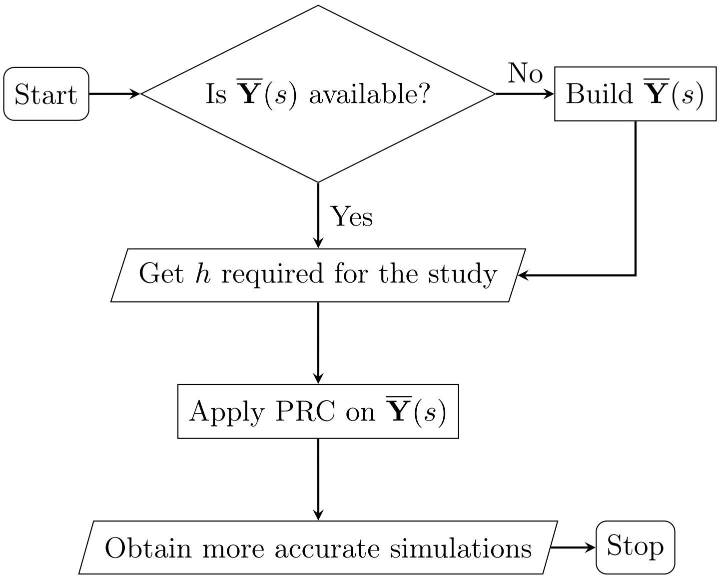

Fig. 5.2: Framework of the PRC algorithm.

5.2.2 Test-circuit Setup

Fig. 5.3 illustrates the test-circuit configuration, where all ports are grounded except for port 1. A single-phase voltage source $e(t) = cos(2\pi f_e t)$ pu, modulated through a ramp from 0 s to 50 µs to attenuate high-frequency transients beyond the fitting bandwidth of 100 kHz, excites port 1. This approach guarantees that accuracy differences stem solely from the trapezoidal rule discretization, not from inherent model mismatches.

High-frequency transients are simulated by varying the excitation frequency f_e. The outputs are the currents $i_j(t)$ for $j = 1, \ldots, N$, following the terminology of the original data in (GUSTAVSEN, 2008b). To compute these currents, the voltage input vector is convolved with the frequency-dependent equivalent using the trapezoidal rule.

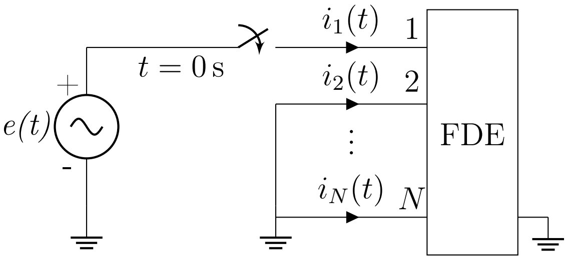

Fig. 5.3: Test-circuit configuration. FDE is the frequency-dependent equivalent.

5.2.3 Numerical Results and Discussion

The performance of the PRC is validated using two frequency-dependent equivalents: a transmission line (Case A) and a distribution network (Case B). A total of 50 poles are used for the fitting process in both cases.

Although Chapter 4 demonstrates the superior performance of the CVF over VF, this section deliberately employs the conventional VF approach to obtain the rational models. This choice aims to isolate and evaluate the performance of the PRC algorithm itself, without interference from the fitting technique. By using the well-established VF method as a baseline, any improvement observed in the time-domain simulations can be directly attributed to the proposed PRC algorithm rather than to an enhanced fitting process. This strategy ensures a clear and fair assessment of the contribution toward mitigating frequency warping errors.

High-frequency transients are simulated with five scenarios, considering f_e ranging from 10 kHz to 90 kHz in 20 kHz intervals. The simulation duration is 0.5 ms.

Frequency responses are obtained by directly evaluating $\overline{\mathbf{Y}}(s)$ and $\overline{\mathbf{Y}'}(s)$. The reference frequency response is generated by mapping $\overline{\mathbf{Y}}(s)$ onto the warped frequency axis over the fitting range, using the following transformation:

$$\omega_a = \frac{2}{h} \tan\left(\frac{\omega h}{2}\right), \tag{3.5}$$

which accounts for the frequency warping effects introduced by the trapezoidal rule.

In all scenarios of a given case, $h = 1\,\mu\text{s}$ was adopted unless stated otherwise. This value complies with the criterion (3.45), considering that $f_{max} = 100\,\text{kHz}$ is the highest frequency component of the frequency response data used to build the rational model.

In the absence of an analytical solution, a reference waveform $i_{ref}(t)$ is generated by simulating the system with $h = 1\,\mu\text{s}/10000 = 100\,\text{ps}$, as the frequency warping is negligible for such a small time-step size.

In addition to the RMSE, the accuracy of the proposed algorithm is evaluated using the Normalized Maximum Absolute Error (NMAE) , denoted as I_{NMAE}. This metric quantifies the largest deviation between the simulated and reference signals, normalized by the peak value of the reference signal, thereby providing a measure of the relative significance of the worst-case error. Thus,

$$I_{\text{NMAE}} = \frac{\max\left(|i(n) - i_{ref}(n)|\right)}{\max\left(|i_{ref}(n)|\right)}, \tag{5.29}$$

where $n = t/h$ and N_T is the total number of simulation steps.

Case A: Transmission Line

The first case models the 132 kV overhead three-phase transmission line in Fig. 5.4. $\overline{\mathbf{Y}}(s)$ is obtained with calculations performed at the sending-end of the line while the receiving-end of the line is open-circuited. More details regarding the modeling are shown in Section 4.4.2. The output is the current at port 1 $i_1(t)$, considering the circuit configuration in Fig. 5.3.

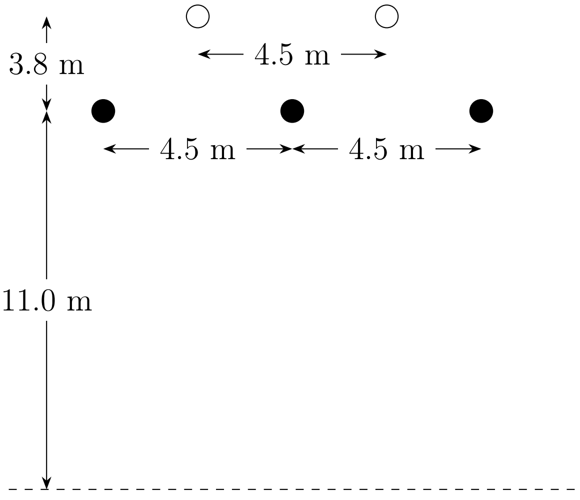

Fig. 5.4: 132 kV transmission line conductor configuration, Case A. The ground and phase wires are represented as white and black circles, respectively. Adapted from GUSTAVSEN (2008a). Repeated from Fig. 4.1.

In the frequency domain, the PRC modifies the uncompensated frequency response to compensate for the frequency warping distortion, as shown in Fig. 5.5. This compensation significantly improves the agreement between the PRC and the reference responses. Differences between the uncompensated and the reference frequency responses become more pronounced at higher frequencies due to the stronger compressing effect of the frequency warping.

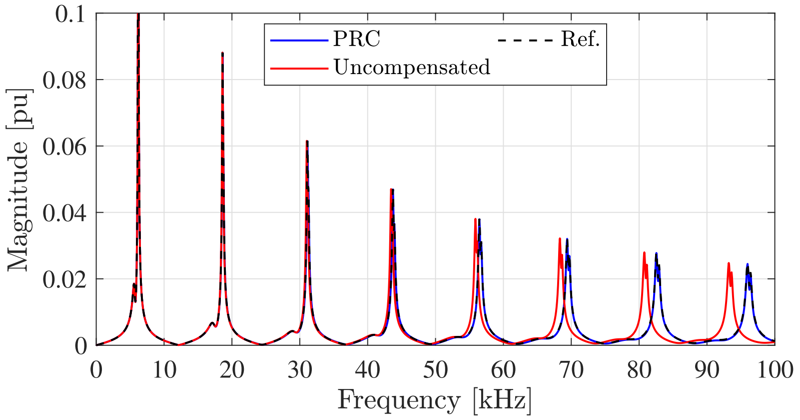

Fig. 5.5: Magnitude of frequency responses, $h = 1\,\mathrm{us}$, Case A.

The pole plot shown in Fig. 5.6 reveals that poles with larger imaginary components, corresponding to higher-frequency system dynamics, undergo more significant pre-warping. This effect is a direct consequence of the pole perturbation introduced by the frequency warping.

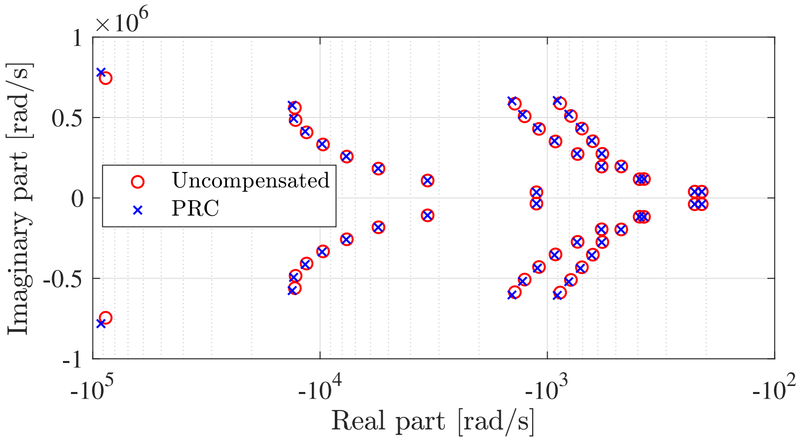

Fig. 5.6: Pole placement of the rational approximations, Case A.

The accuracy-enhancing feature of PRC can be leveraged either to improve accuracy for a given time-step size or to enable more efficient simulations, as demonstrated in Table 5.1 for the RMSE metric. For $h = 1\,\mu\mathrm{s}$, the PRC method consistently improves accuracy across all tested scenarios, yielding enhancements between

3.6 and 24.4 times. To achieve similar RMSE as the simulation using PRC with $h = 1\,\mu s$, the uncompensated simulation must be held with a significantly smaller time-step size, ranging from 0.5 µs (2 times smaller) for $f_e = 10$ kHz to 0.18 µs (5.6 times smaller) for $f_e = 70$ kHz. The benefit in time-step size is less pronounced at lower frequencies, as the influence of frequency warping becomes more significant at higher frequencies.

Table 5.1: RMSE values (pu) for time-domain simulations in Case A

f_e	$h = 1\,\mu s$			*Reduced h		
(kHz)	Uncompensated	PRC	Ratio[1]	h^* (µs)	Uncompensated*	Ratio[2]
10	2.38×10^{-5}	6.57×10^{-6}	3.62	0.50	7.37×10^{-6}	1.12
30	5.71×10^{-4}	6.61×10^{-5}	8.64	0.35	6.96×10^{-5}	1.05
50	5.61×10^{-4}	4.77×10^{-5}	11.76	0.30	5.31×10^{-5}	1.11
70	3.12×10^{-3}	1.49×10^{-4}	20.94	0.18	1.61×10^{-4}	1.08
90	4.36×10^{-3}	1.79×10^{-4}	24.36	0.22	1.92×10^{-4}	1.07

[1] Uncompensated over PRC.
[2] Uncompensated* over PRC.

For the NMAE metric, the results in Table 5.2 highlight the effectiveness of the PRC method in enhancing simulation accuracy across all tested scenarios. The technique consistently reduces errors by factors ranging from 5.5 to 21.6 times. Notably, it performs better at higher frequencies, lowering the NMAE from 231.64% to 10.75% at 90 kHz (a 21.6 times improvement), and from 88.84% to 4.32% at 70 kHz (a 20.6 times improvement).

Table 5.2: NMAE for time-domain simulations in Case A

f_e (kHz)	Uncompensated (%)	PRC (%)	Ratio[1]
10	2.14	0.39	5.49
30	16.67	1.35	12.35
50	63.88	3.60	17.74
70	88.84	4.32	20.56
90	231.64	10.75	21.55

[1] Uncompensated over PRC.

Qualitatively, the time-domain waveforms for the excitation frequencies of 50 kHz and 90 kHz are displayed in Figs. 5.7 and 5.8, respectively. It is clear that, even for the same time-step size, the uncompensated waveform exhibited significant deviations from the reference, whereas the PRC results closely matched the reference. The oscillation of the absolute error arises from the amplitude error being more pronounced at peak values and less severe near zero values.

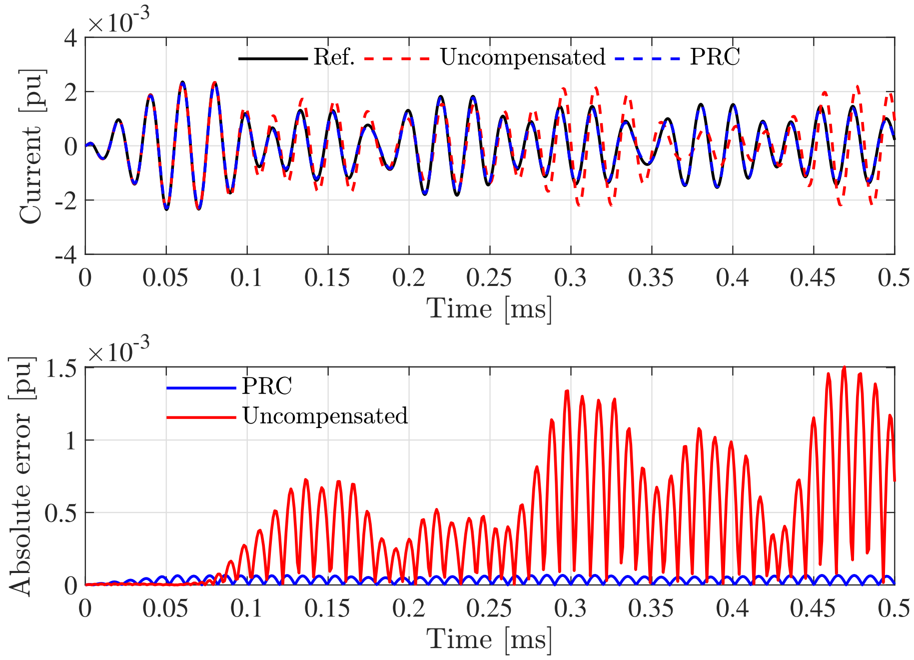

Fig. 5.7: Time-domain responses of the reference, uncompensated, and PRC waveforms (top), along with their absolute error (bottom) with $f_e = 50\,\text{kHz}$, Case A.

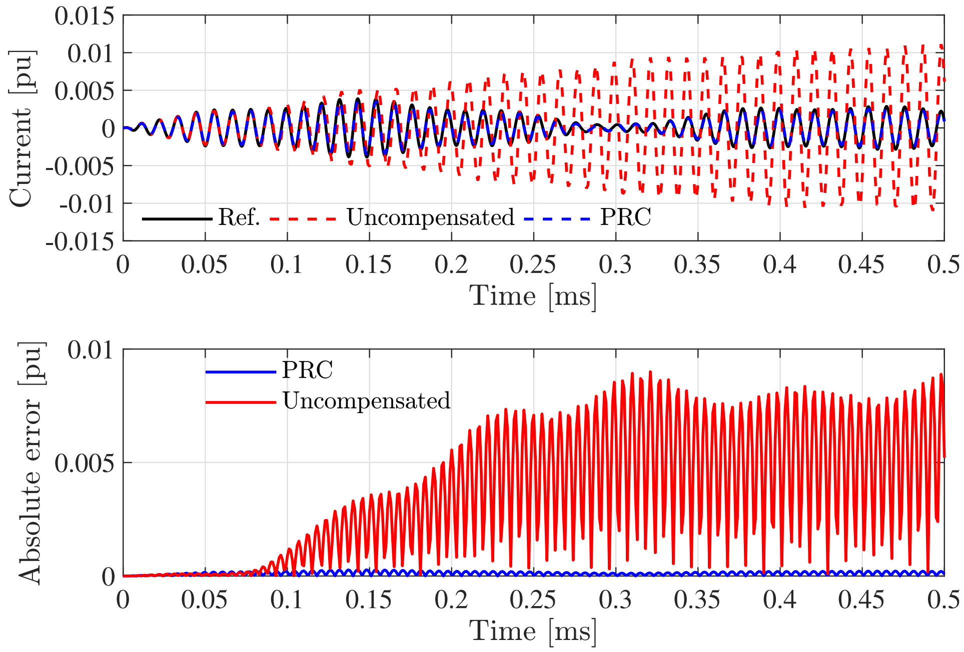

Fig. 5.8: Time-domain responses of the reference, uncompensated, and PRC waveforms (top), along with their absolute error (bottom) with $f_e = 90\,\text{kHz}$, Case A.

For the 50 kHz source, the frequency warping increased the amplitude of the uncompensated waveform in around 0.15 ms, 0.30 ms, and 0.45 ms. In contrast, the amplitude of the uncompensated signal was reduced around 0.40 ms. This behavior can be understood by analyzing the spectrum near 50 kHz in Fig. 5.5. Depending on the frequency, the amplitude of the uncompensated frequency response may be either lower or higher than that obtained with PRC.

Fig. 5.8 illustrates that, for an excitation frequency of 90 kHz, the frequency warping introduces substantial amplitude errors in the uncompensated signal after 0.15 s. This distortion arises from the frequency mapping induced by frequency warping, which shifts the dominant resonance peak, originally at a higher frequency in Fig. 5.5, towards the excitation frequency. In contrast, the PRC waveform remains well-aligned with the reference, effectively preserving the accuracy of the signal.

Case B: Distribution Network

The second case, illustrated in Fig. 5.9, represents a distribution network with two three-phase buses, for which the admittance $\overline{\mathbf{Y}}(s)$ is computed with respect to both bus-bars. More information regarding this system is provided in Section 4.4.3. The output is defined as the current at port 2, $i_2(t)$, following the configuration shown in Fig. 5.3.

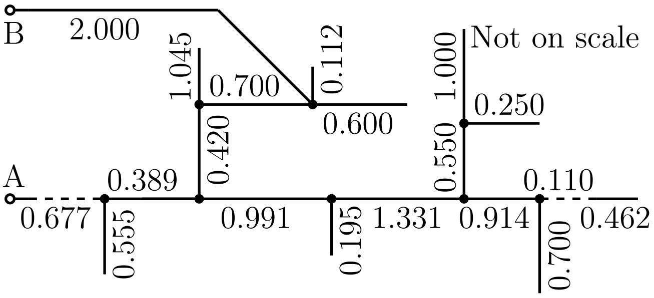

Fig. 5.9: Single-line diagram of the three-phase distribution system, Case III. The numbers are the line length in km. Continuous and dashed lines are overhead lines and underground cables, respectively. Adapted from DESCHRIJVER *et al.* (2007). Repeated from Fig. 4.2.

Fig. 5.10 demonstrates the effectiveness of the PRC method in compensating frequency warping as its frequency response shows excellent agreement with the reference, particularly at higher frequencies where warping effects are more pronounced. As expected, spectral components in this region undergo more substantial pre-warping to compensate for the nonlinear frequency scaling introduced by the frequency warping. The pole placement shown in Fig. 5.11 reinforces this observation, as the high-frequency poles undergo a more pronounced shift due to frequency warping compensation.

The PRC achieved an accuracy improvement ranging from 4.8 to 23.7 times, as outlined in Table 5.3. To match the RMSE obtained by the PRC with $h = 1\,\mu\text{s}$, the uncompensated simulation requires significantly smaller time-step size, ranging from 0.4 µs (2.5 times smaller) at $f_e = 10\,\text{kHz}$ to 0.15 µs (6.67 times smaller) at $f_e =$

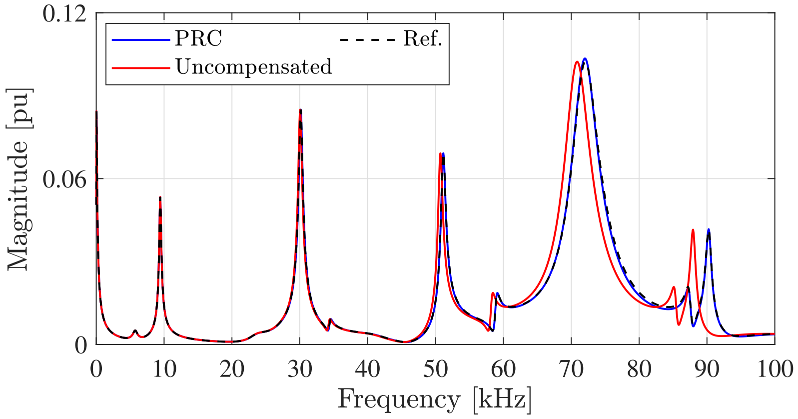

Fig. 5.10: Magnitude of frequency responses, $h = 1\,\mathrm{us}$, Case B.

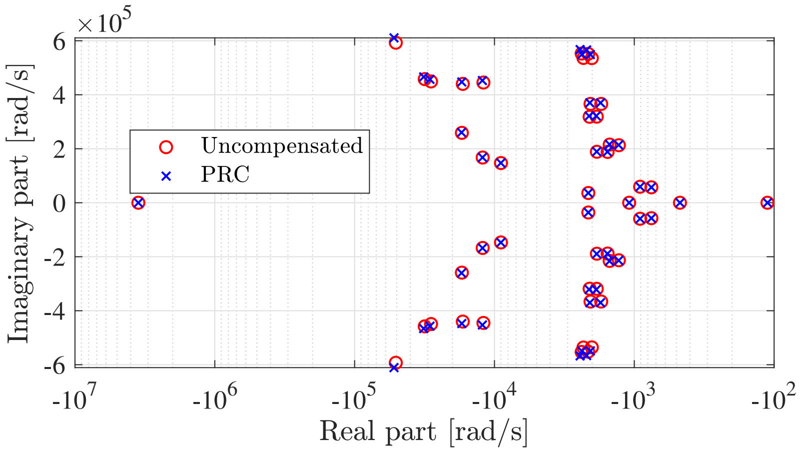

Fig. 5.11: Pole placement of the rational approximation, Case B.

90 kHz. The advantage in time-step size is more pronounced at higher frequencies, due to the spectral compression effect introduced by frequency warping. As a result, PRC enables fewer model evaluations (due to the larger time-step size), reduced memory usage, and negligible computational overhead, since the scaling factors are computed only once per pole–residue pair.

Table 5.4 presents the NMAE reduction obtained with the PRC method, showing improvement factors between 4.1 and 28.5 times. Notably, the PRC method consistently maintains NMAE values below 7%, while the uncompensated waveforms exhibit errors up to 128%.

Time-domain waveforms for $f_e = 70\,\mathrm{kHz}$ and $f_e = 90\,\mathrm{kHz}$ are shown in Figs. 5.12 and 5.13, respectively. Fig. 5.12 shows a significant mismatch after 0.2 ms, where the maximum absolute error of the uncompensated waveform exceeds the peak amplitude of the reference signal. Fig. 5.13 shows a similar trend: the uncompensated waveform suffers notable distortion between 0.1 ms and 0.4 ms, whereas the PRC result remains closely aligned with the reference. This discrepancy is attributed to

Table 5.3: RMSE values (pu) for time-domain simulations in Case B

f_e	$h = 1\,\mu s$			*Reduced h		
(kHz)	Uncompensated	PRC	Ratio[1]	h^* (µs)	Uncompensated*	Ratio[2]
10	3.39×10^{-5}	7.03×10^{-6}	4.82	0.40	6.18×10^{-6}	0.88
30	1.92×10^{-3}	1.53×10^{-4}	12.55	0.30	1.73×10^{-4}	1.13
50	7.27×10^{-3}	3.07×10^{-4}	23.68	0.20	2.89×10^{-4}	0.94
70	5.37×10^{-2}	2.40×10^{-3}	22.38	0.20	2.24×10^{-3}	0.93
90	4.94×10^{-3}	2.55×10^{-4}	19.37	0.15	2.43×10^{-4}	0.95

[1] Uncompensated over PRC.

[2] Uncompensated* over PRC.

Table 5.4: NMAE values for time-domain simulations in Case B

f_e (kHz)	Uncompensated (%)	PRC (%)	Ratio[1]
10	0.49	0.12	4.08
30	11.26	0.79	14.25
50	61.56	2.16	28.50
70	127.98	5.46	23.44
90	114.05	6.10	18.70

[1] Uncompensated over PRC.

frequency warping shifting the resonance peak near 90 kHz in Fig. 5.10 to a value lower than the excitation frequency.

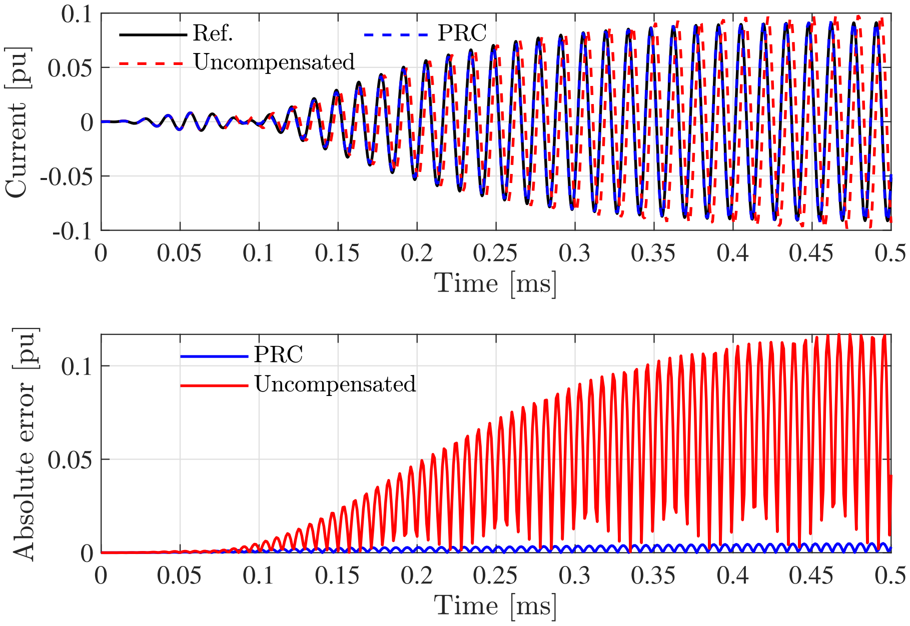

Fig. 5.12: Time-domain responses of the reference, uncompensated, and PRC waveforms (top), along with their absolute error (bottom) with $f_e = 70\,\mathrm{kHz}$, Case B.

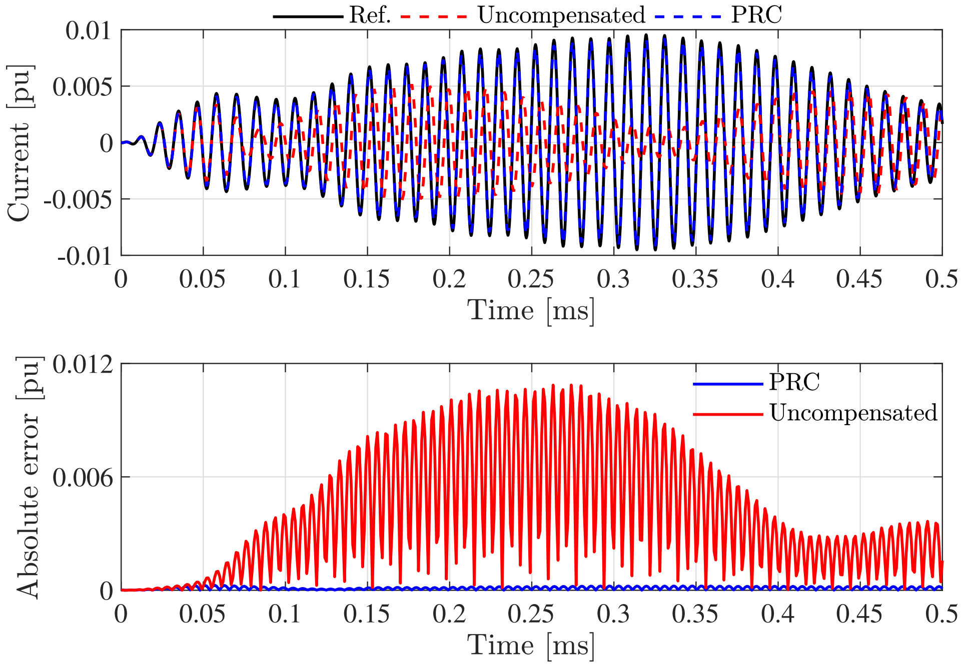

Fig. 5.13: Time-domain responses of the reference, uncompensated, and PRC waveforms (top), along with their absolute error (bottom) with $f_e = 90\,\mathrm{kHz}$, Case B.

5.3 The Frequency-Shifted Pole-Residue Frequency Warping Compensation

Consider the mathematical definition of the frequency warping for the trapezoidal rule:

$$\Psi = \frac{2}{\omega h}\tan\left(\frac{\omega h}{2}\right). \tag{3.21}$$

The conventional approach to reducing Ψ is by decreasing h. In contrast, the PRC algorithm presented in Section 5.2 reduces this error through mapping of the poles and residues of a rational model. This section proposes a complementary strategy to reduce the frequency warping error in (3.21) by reducing the maximum frequency ω through frequency shifts. Therefore, this section presents the Frequency-shifted Pole-Residue Compensation (FPRC), which leverages analytical signals, frequency shifts, CVF, interpolation, and PRC to further enhance accuracy.

5.3.1 Analytic Signal

The synthesized frequency-dependent equivalent using the CVF framework exhibits a complex impulse response, even for real-valued inputs (KING and BRAZIL, 2017).

While such responses do not occur in the physical systems (GRIVET-TALOCIA and GUSTAVSEN, 2015), they offer the potential for enhancing simulation efficiency (SPINA *et al.*, 2021).

Time-domain simulations utilizing the CVF framework employ analytic signals (YE *et al.*, 2019), which are a class of complex-valued functions that satisfy the Cauchy-Riemann conditions for differentiability (COHEN, 1995).

An analytic signal $u_A(t)$ provides a complex-valued representation of a real-valued signal $u(t)$ and is defined as (YANG *et al.*, 2009):

$$u_A(t) = u(t) + j\mathcal{H}\{u(t)\}, \tag{5.30}$$

$$\mathcal{H}\{u(t)\} = \frac{1}{\pi}\int_{-\infty}^{\infty}\frac{u(\tau)}{t-\tau}d\tau, \tag{5.31}$$

where $\mathcal{H}\{\cdot\}$ is the Hilbert transform of $\{\cdot\}$.

The Hilbert transform is a linear operator that shifts the phase of each frequency component of $u(t)$ by -90^o (positive frequencies) or 90^o (negative frequencies). This transformation ensures that $u_A(t)$ retains only the non-negative frequency components $u(t)$, scaled by a factor of two.

The spectrum of $u_A(t)$ can be shifted toward 0 Hz by an arbitrary frequency offset Δf, resulting in the frequency-shifted analytic signal:

$$u_{A,sh}(t) = \exp(-j2\pi\Delta f t)u_A(t). \tag{5.32}$$

For example, the cosine signal $x(t)$, expressed in both trigonometric and complex exponential forms, yields

$$x(t) = V_p\cos(2\pi f_e t) = V_p\frac{\exp(j2\pi f_e t) + \exp(-j2\pi f_e t)}{2}, \tag{5.33}$$

where V_p is the peak voltage (amplitude).

Eliminating the negative frequency component of (5.33) and multiplying by two yields its analytic representation:

$$x_A(t) = 2V_p\frac{\exp(j2\pi f_e t)}{2} = V_p\exp(j2\pi f_e t). \tag{5.34}$$

Applying a frequency shift of Δf in (5.34) yields:

$$x_{A,sh}(t) = V_p\exp(-j2\pi\Delta f t)\exp(j2\pi f_e t). \tag{5.35}$$

When $\Delta f = f_e$, the shifted analytic signal $x_{A,sh}(t)$ in (5.35) reduces to a DC signal with amplitude V_p. The corresponding magnitude spectra of $x(t)$, $x_A(t)$, and $x_{A,sh}(t)$ are illustrated in Fig. 5.14.

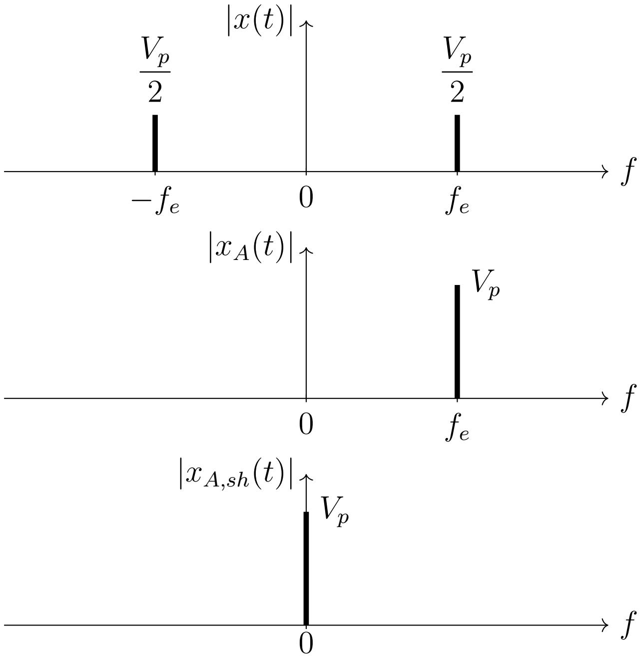

Fig. 5.14: Magnitude spectra of the cosine signal $x(t)$, showing three representations: real-valued (top), analytic (middle), and frequency-shifted analytic (bottom).

5.3.2 Proposed Framework

The FPRC algorithm integrates PRC and CVF to improve EMT simulation accuracy. As shown in Chapter 4, CVF achieves better fitting than VF for a given model order. Relaxing the realness constraint allows CVF to support baseband modeling and simulation (YE *et al.*, 2019), thereby allowing simulations to be conducted in a frequency-shifted domain. FPRC constructs rational models in a frequency-shifted domain, where a user-defined shift Δf reduces the maximum frequency component by Δf. Since Ψ in (3.21) grows nonlinearly with frequency, the frequency-shifted domain reduces frequency warping and thereby improves overall simulation accuracy.

Fig. 5.15 illustrates the workflow of the proposed framework, where the voltage $e(t)$ and current $i(t)$ serve as the original input and output real-valued signals, respectively. Their corresponding analytic representations, $e_A(t)$ and $i_A(t)$, are defined as (5.30). Subsequently, the frequency-shifted analytic signals, $e_{A,sh}(t)$ and $i_{A,sh}(t)$, are obtained using (5.32). Because the complex envelope $|i_{A,sh}(t)|$ varies more slowly than $i(t)$, interpolation with a smaller h improves numerical accuracy before applying the inverse transformation. The actual time-domain simulation uses a coarser h, and the finer interpolation serves only to reconstruct the real-valued signal with higher resolution.

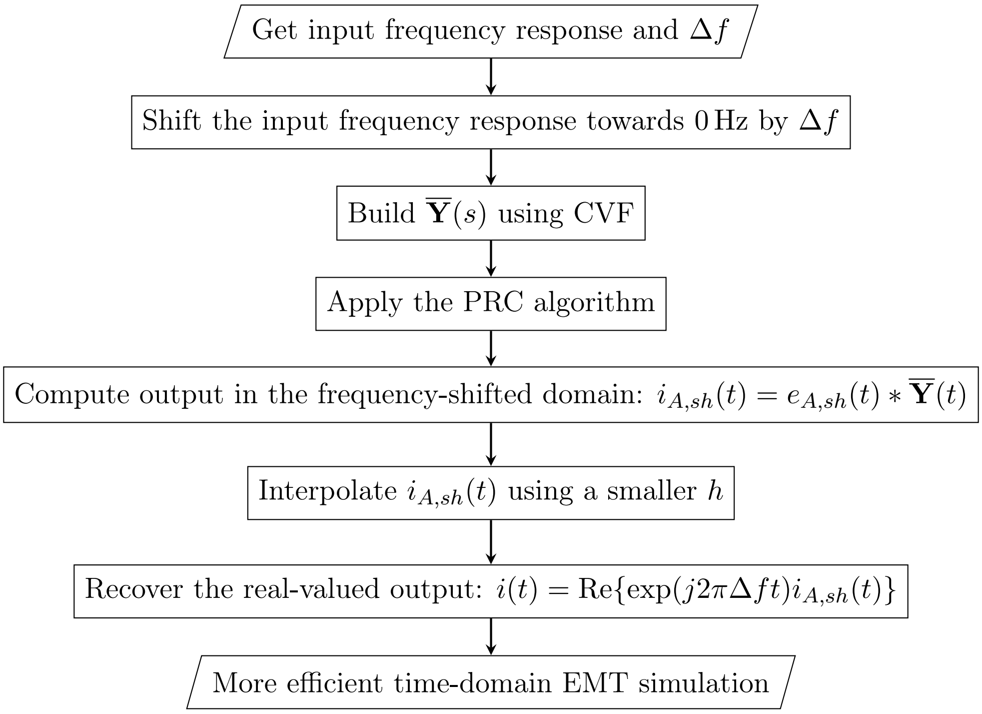

Fig. 5.15: Framework of the FPRC algorithm.

5.3.3 Results and Discussion

Two numerical examples, Case A and Case B, previously introduced in Section 5.2, validate the proposed framework Case A models a transmission line, while Case B represents a distribution network. Each case includes three CVF-derived models, constructed with distinct frequency shifts. All rational models, regardless of frequency shift, share the same model order, iteration count, weighting function, and pole initialization.

The test-circuit configuration used to compute time-domain responses is identical to the one shown in Fig. 5.3 in Section 5.2.2. In the proposed methodology, EMT simulations leverage analytic signals and frequency shifts, so $e(t)$ is replaced by $e_{A,sh}(t)$ in that illustration. The simulation length is set to 0.5 ms.

To investigate high-frequency transient behavior, the excitation frequency f_e is set to either 50 kHz (Case A) or 60 kHz (Case B). The resulting currents $i_j(t)$ are computed using the framework shown in Fig. 5.15, using the trapezoidal rule for discretization. Accuracy is evaluated through the RMSE and NMAE metrics. The reference frequency response is determined using the same methodology outlined in Section 5.2.3.

Case A – Transmission Line

The first case involves modeling a 132 kV overhead three-phase transmission line shown in Fig. 4.1, using 50 poles. The output is evaluated as the current at port

1 $i_1(t)$, considering $f_e = 50\,\text{kHz}$. Three CVF-derived models are constructed with frequency shifts of 0 Hz, 25 kHz, and 50 kHz.

Table 5.3.3 summarizes the fitting RMSEs using CVF-derived models under different values of Δf. The consistently low and similar RMSE values indicate a high-quality fit for systems lacking Hermitian symmetry, regardless of the applied frequency shift.

Table 5.5: Fitting RMSEs for CVF-derived models with different Δf, Case A.

Δf (kHz)	RMSE (pu)
0	8.97×10^{-13}
25	1.08×10^{-12}
50	1.07×10^{-12}

Figs. 5.16, 5.17, and 5.18 show the frequency responses of $\overline{Y}_{1,1}(s)$ obtained using $h = 4\,\mu\text{s}$, considering Δf of 0 Hz, 25 kHz, and 50 kHz, respectively. The results demonstrate the CVF ability to model frequency responses without Hermitian symmetry. The reduced mismatch between the model and reference responses near the effective excitation frequencies of 50 kHz, 25 kHz, and 0 Hz for $\Delta f = 0\,\text{Hz}$, 25 kHz, and 50 kHz, respectively, indicates that the frequency shift alone contributes to mitigating frequency warping effects. The application of PRC further improves the agreement with the reference across all values of Δf.

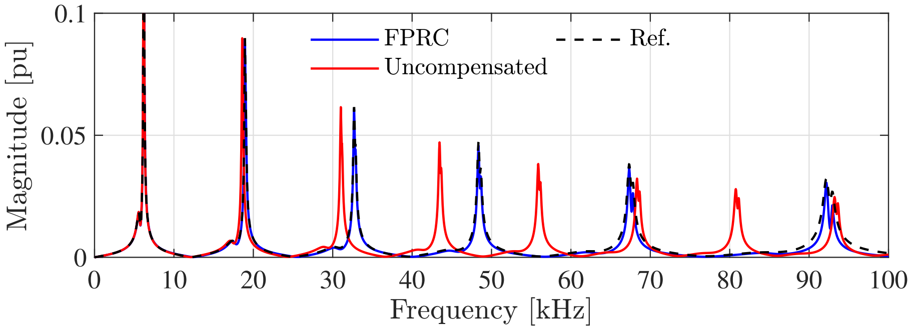

Fig. 5.16: Frequency response for Case A using $h = 4\,\mu\text{s}$ and $\Delta f = 0\,\text{Hz}$.

Figure 5.19 illustrates the complex-valued analytic signal of the output obtained from the CVF-derived model, highlighting the characteristic properties of the analytic representation, including its real component, imaginary component, and magnitude. The imaginary component is in quadrature with the real component, exhibiting a 90^o phase lag to the real component. This is an inherent property of analytic signals, since the imaginary component is obtained by applying the Hilbert transform to the real component, as expressed in (5.30). The real component corresponds to the physical, measurable signal in the time domain, while the magnitude

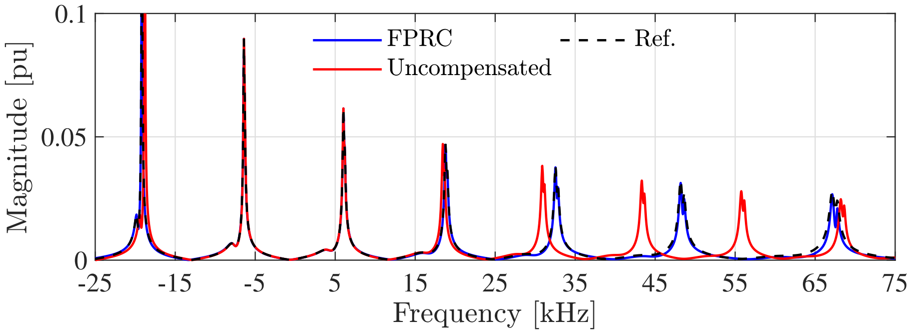

Fig. 5.17: Frequency response for Case A using $h = 4\,\mu s$ and $\Delta f = 25\,kHz$.

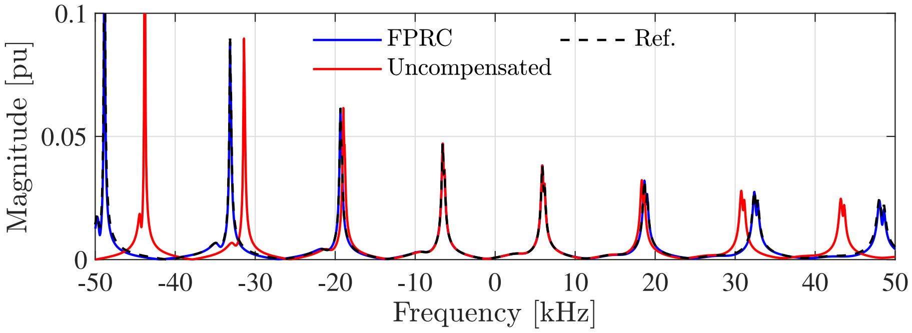

Fig. 5.18: Frequency response for Case A using $h = 4\,\mu s$ and $\Delta f = 50\,kHz$.

(i.e., the absolute value) represents the complex envelope, which characterizes the instantaneous amplitude of the analytical signal.

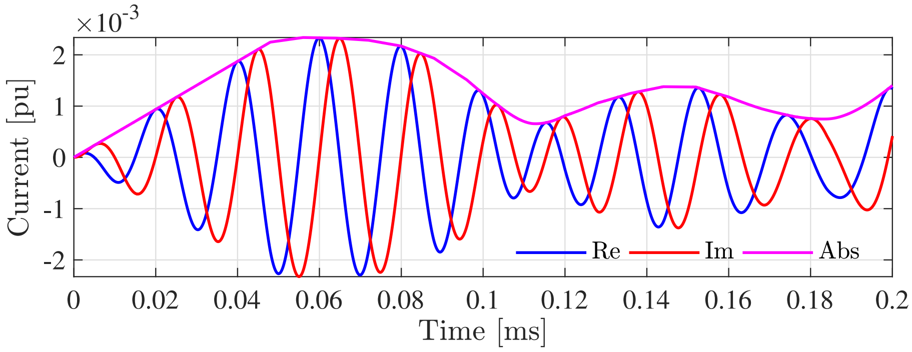

Fig. 5.19: Real component, imaginary component, and the magnitude of the output at port 1, considering $h = 4\,\mu s$ and $\Delta f = 50\,kHz$, Case A.

Table 5.6 presents the RMSE-based simulation accuracy for $\Delta f = 0\,Hz, 25\,kHz, 50\,kHz$, with and without the PRC approach, considering h in the range $0.25\,\mu s \leq h \leq 8\,\mu s$. Fig. 5.20 illustrates the accuracy degradation as the time-step size increases. The RMSE for the non-shifted simulation with $h = 0.25\,\mu s$ (3.66×10^{-5} pu) is comparable to that obtained with $h = 8\,\mu s$ (2.88×10^{-5} pu) using the PRC with $\Delta f = 50\,kHz$, indicating that proposed approach enables a 32 times increase in the time-step size without compromising accuracy. Remarkably, for $h = 4\,\mu s$ the FPRC simulation leads to an improvement in RMSE by a factor of 293.1 in comparison to the non-shifted and uncompensated simulation. When isolating the improvements attributable solely to the frequency shift, the RMSE obtained with $h = 0.25\,\mu s$ and $\Delta f = 0\,\text{Hz}$ (3.66×10^{-5} pu) is comparable to those obtained with $h = 0.6\,\mu s$ and $\Delta f = 25\,\text{kHz}$ (3.32×10^{-5} pu) and $h = 2\,\mu s$ and $\Delta f = 50\,\text{kHz}$ (3.01×10^{-5} pu), corresponding to improvements of 2.4 times and 8 times in time-step size, respectively.

Table 5.6: Summary of RMSEs (in pu) from time-domain simulations with $f_e = 50\,\text{kHz}$ for different Δf and h, Case A.

h	Δf (kHz)					
(µs)	0	0*	25	25*	50	50*
0.25	3.66×10^{-5}	5.95×10^{-6}	6.49×10^{-6}	3.48×10^{-6}	3.04×10^{-6}	3.02×10^{-6}
0.6	2.10×10^{-4}	3.44×10^{-5}	3.32×10^{-5}	9.92×10^{-6}	3.86×10^{-6}	3.02×10^{-6}
1	5.57×10^{-4}	9.64×10^{-5}	9.11×10^{-5}	2.64×10^{-5}	8.56×10^{-6}	3.16×10^{-6}
2	1.32×10^{-3}	1.34×10^{-4}	3.45×10^{-4}	1.06×10^{-4}	3.01×10^{-5}	5.10×10^{-6}
3	2.67×10^{-3}	2.82×10^{-4}	6.98×10^{-4}	1.87×10^{-4}	4.57×10^{-5}	1.09×10^{-5}
4	3.40×10^{-3}	3.73×10^{-4}	9.63×10^{-4}	2.62×10^{-4}	5.70×10^{-5}	1.16×10^{-5}
8	–	–	2.36×10^{-3}	3.80×10^{-4}	8.67×10^{-5}	2.88×10^{-5}

*Frequency shift + PRC.

–Aliasing due to the Nyquist frequency limit.

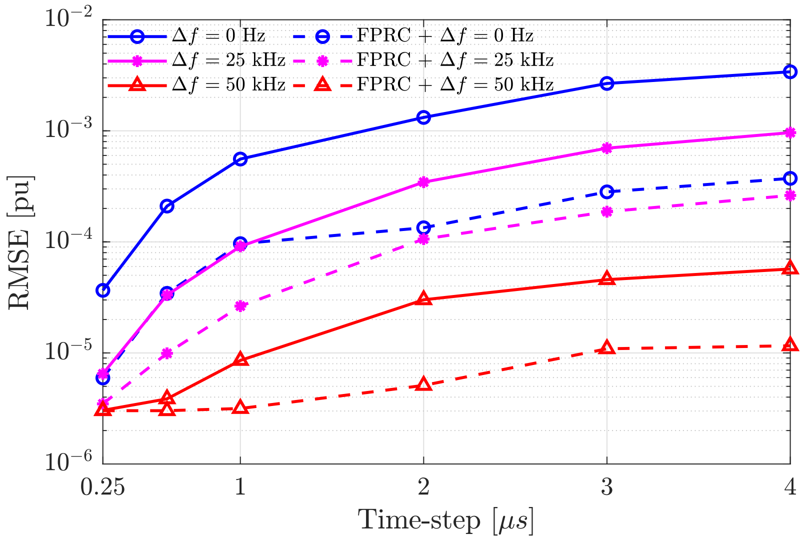

Fig. 5.20: Error trend regarding h, Case A.

The NMAE results in Table 5.7 demonstrate how frequency shifting and the PRC method enable larger simulation time-steps while maintaining low error. For a target NMAE of 4.38% (achieved at $h = 0.25\,\mu s$ with $\Delta f = 0\,\text{Hz}$), applying only frequency shifting allows increasing h to $0.6\,\mu s$ ($\Delta f = 25\,\text{kHz}$, NMAE = 4.23%)

or even 2 µs (Δf = 50 kHz, NMAE = 4.01%). Without mitigation, errors escalate drastically, peaking at 338.11% for the unshifted and uncompensated simulation with $h = 4$ µs. At this time-step, applying PRC alone reduces the NMAE to 38.14% (an improvement of 8.9 times). Using only frequency shifting of 50 kHz, the NMAE drops to 6.78% (an improvement of 49.9 times). Combining this frequency shift with PRC further decreases the NMAE to 3.35%, an improvement of 100.9 times in this metric. The FPRC method achieves a NMAE of 5.74% at $h = 8$ µs, closely matching the 4.38% obtained with $h = 0.25$ µs in the unshifted and uncompensated case.

Table 5.7: Summary of NMAE, expressed in %, from time-domain simulations with $f_e = 50$ kHz for different Δf and h, Case A.

h (µs)	Δf (kHz)					
	0	0*	25	25*	50	50*
0.25	4.38	0.42	0.77	0.61	0.49	0.49
0.6	25.54	2.43	4.23	1.15	0.49	0.49
1	63.97	6.75	10.99	2.32	1.39	0.48
2	140.37	11.81	37.33	7.89	4.01	0.91
3	245.70	24.29	72.93	13.77	6.30	2.87
4	338.11	38.14	109.52	19.47	6.78	3.35
8	–	–	238.76	38.82	11.00	5.74

*Frequency shift + PRC.

–Aliasing due to the Nyquist frequency limit.

Qualitative evidence of the effectiveness of the PRC method appears in the time-domain waveforms shown in Fig. 5.21, corresponding to $h = 4$ µs for $\Delta f = 0$ Hz and $h = 8$ µs for $\Delta f = 50$ kHz with PRC. Note that, although these simulations run at the indicated time-step sizes, the plotted results are obtained by interpolating the frequency-shifted analytic signal back onto a much finer resolution $h = 100$ ps before extracting its real part. These results highlight a substantial reduction in both amplitude and waveform fidelity when using the FPRC method, even at larger time-step sizes.

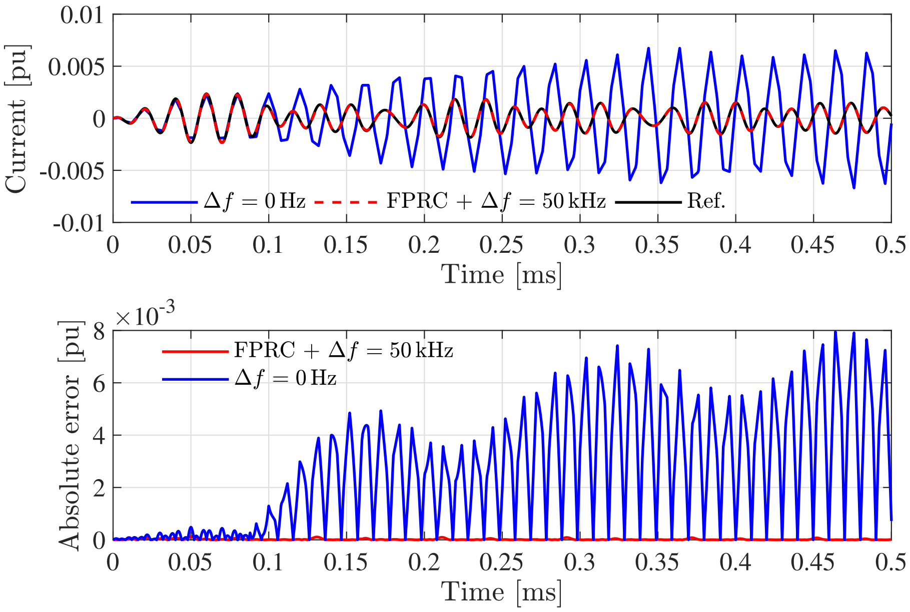

Fig. 5.21: Time-domain comparison of simulations (top) and its absolute errors (bottom) for Case A with $f_e = 50\,\mathrm{kHz}$, using $h = 4\,\mu\mathrm{s}$ for $\Delta f = 0\,\mathrm{Hz}$ and $h = 8\,\mu\mathrm{s}$ for $\Delta f = 50\,\mathrm{kHz}$.

Case B – Distribution Network

Case B refers to the modeling of a distribution system with two three-phase buses as terminals, as illustrated in Fig. 4.2. The rational model uses 50 poles for fitting. The output is evaluated as the current at port 2 $i_2(t)$, considering $f_e = 60\,\mathrm{kHz}$.

Time-domain simulations are performed using three CVF-derived models, constructed using Δf as 0 Hz, 30 kHz, and 60 kHz. The RMSE values obtained for each case are summarized in Table 5.3.3. The low RMSE values confirm the capability of the CVF to accurately model non-Hermitian frequency-shifted systems.

Table 5.8: Fitting RMSEs for CVF-derived models with different Δf, Case B.

Δf (kHz)	RMSE (pu)
0	9.39×10^{-12}
30	2.01×10^{-12}
60	2.27×10^{-12}

Figs. 5.22, 5.23, and 5.24 illustrates the frequency responses of $\overline{Y}_{1,2}(s)$ computed with $h = 3\,\mu\mathrm{s}$, for $\Delta f = 0\,\mathrm{Hz}$, 30 kHz, and 60 kHz, respectively. Introducing a frequency shift attenuates frequency warping effects, as evidenced by the reduced discrepancy between modeled and reference responses near the effective excitation frequencies: 60 kHz (for $\Delta f = 0\,\mathrm{Hz}$), 30 kHz (for $\Delta f = 30\,\mathrm{kHz}$), and 0 Hz (for $\Delta f = 60\,\mathrm{kHz}$). The application of PRC further minimizes this discrepancy across all frequency-shift scenarios.

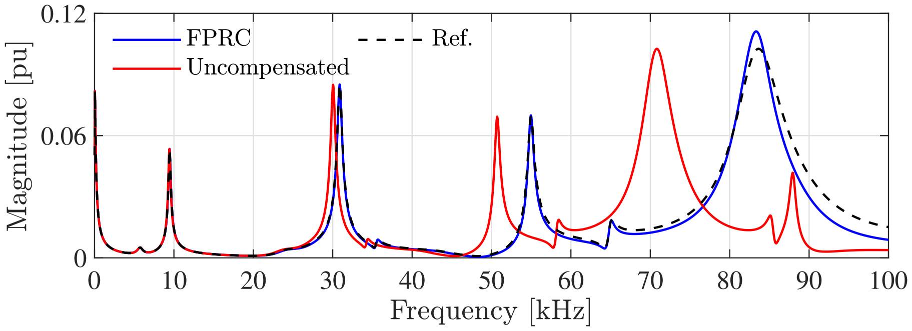

Fig. 5.22: Frequency response for Case B using $h = 3\,\mu\text{s}$ and $\Delta f = 0\,\text{Hz}$.

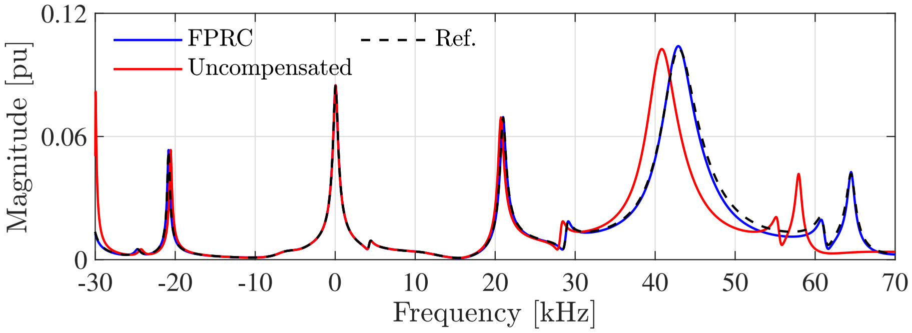

Fig. 5.23: Frequency response for Case B using $h = 3\,\mu\text{s}$ and $\Delta f = 30\,\text{kHz}$.

Figure 5.25 shows the complex-valued analytic signal produced by the CVF-derived model. In this representation, the real part corresponds to the original time-domain waveform, the imaginary part denotes its quadrature component, and the magnitude, also referred to as the complex envelope, provides the instantaneous amplitude of the complex-valued signal.

Table 5.9 summarizes RMSE-based accuracy metric for simulations performed with frequency shifts of 0 Hz, 30 kHz, and 60 kHz, both with and without the PRC enhancement, for time-step sizes ranging from 0.1 µs to 10 µs. Fig. 5.26 shows the RMSE as a function of h, clearly illustrating the loss of accuracy as the time step increases. Notably, the non-shifted simulation at $h = 0.2\,\mu\text{s}$ achieves an RMSE of 1.07×10^{-4} pu, which matches the RMSE obtained at $h = 7\,\mu\text{s}$ when using

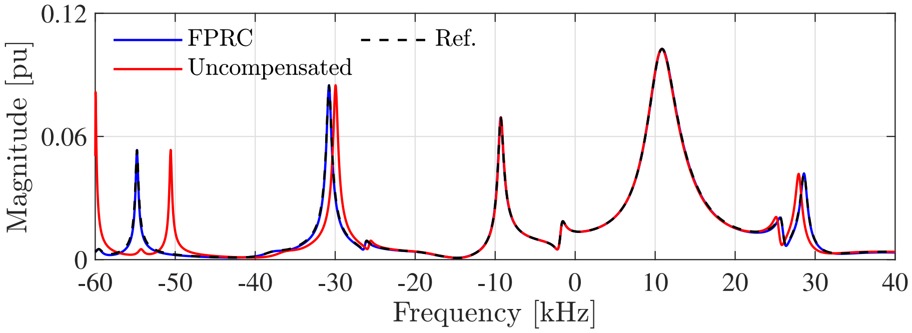

Fig. 5.24: Frequency response for Case B using $h = 3\,\mu\text{s}$ and $\Delta f = 60\,\text{kHz}$.

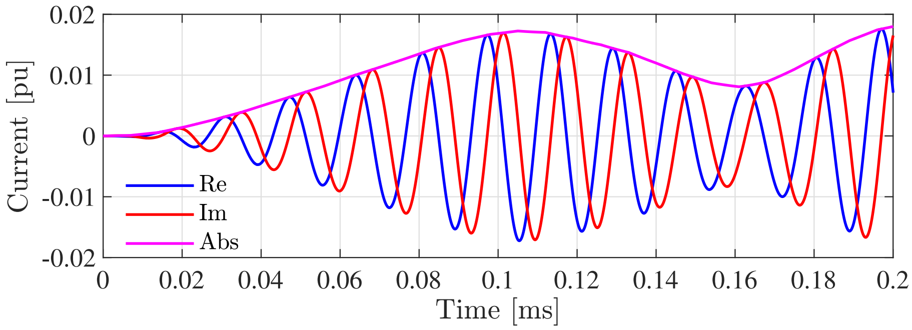

Fig. 5.25: Real component, imaginary component, and the magnitude of the output at port 1, considering $h = 7\,\mu s$ and $\Delta f = 60\,kHz$, until 0.2 ms, Case B.

$\Delta f = 60\,kHz$ in conjunction with PRC. This demonstrates that, by applying the PRC method, the time step can be increased by a factor of 35, without sacrificing accuracy. Moreover, at $h = 3\,\mu s$, the RMSE of the uncompensated and non-shifted model is 2.38×10^{-2} pu, whereas introducing a 60 kHz shift combined with PRC reduces the error to 2.64×10^{-5} pu, an improvement factor of approximately 901 times. Isolating the benefit of frequency shifting alone reveals that the baseline RMSE of 1.07×10^{-4} pu at $h = 0.2\,\mu s$ and $\Delta f = 0\,Hz$ can be approximately obtained with a simulation considering $h = 0.5\,\mu s$ and $\Delta f = 30\,kHz$ (RMSE of 1.17×10^{-4} pu), and even by $h = 3\,\mu s$ with $\Delta f = 60\,kHz$ (RMSE of 1.17×10^{-4} pu). These results correspond to 2.5 times and 15 times increases in allowed time-step size, respectively, solely through the application of a frequency shift.

Table 5.9: Summary of RMSEs (in pu) from time-domain simulations with $f_e = 60\,kHz$ for different Δf and h, Case B.

h (μs)	Δf (kHz) 0	0*	30	30*	60	60*
0.2	1.07×10^{-4}	1.29×10^{-5}	2.46×10^{-5}	1.47×10^{-5}	2.01×10^{-5}	1.92×10^{-5}
0.5	6.62×10^{-4}	8.04×10^{-5}	1.17×10^{-4}	2.52×10^{-5}	2.44×10^{-5}	1.92×10^{-5}
1	2.46×10^{-3}	3.19×10^{-4}	4.49×10^{-4}	8.41×10^{-5}	3.51×10^{-5}	1.93×10^{-5}
2	6.08×10^{-3}	1.22×10^{-3}	1.74×10^{-3}	3.35×10^{-4}	6.68×10^{-5}	2.09×10^{-5}
3	2.38×10^{-2}	2.61×10^{-3}	3.41×10^{-3}	7.42×10^{-4}	1.17×10^{-4}	2.64×10^{-5}
7	–	–	1.09×10^{-2}	3.58×10^{-3}	3.84×10^{-4}	1.07×10^{-4}

*Frequency shift + PRC.
–Aliasing due to the Nyquist frequency limit.

Table 5.10 presents the accuracy metric through NMAEs. Consider the baseline configuration obtained with $h = 0.2\,\mu s$ and $\Delta f = 0\,Hz$, which results to a NMAE of 1.54%. By applying frequency shifting alone, it is possible to increase the time step to $0.5\,\mu s$ with $\Delta f = 30\,kHz$ (NMAE = 1.83%), or even to $3\,\mu s$ with $\Delta f = 60\,kHz$ (NMAE = 1.69%), while maintaining comparable accuracy. In the absence of any

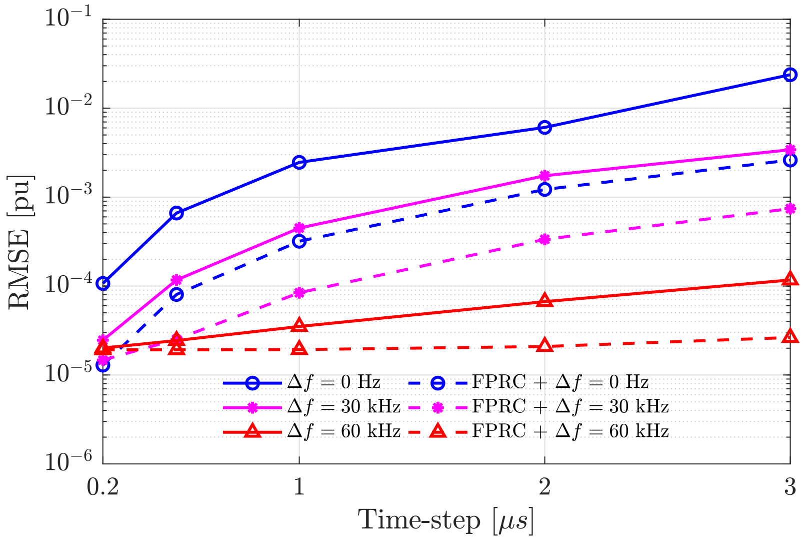

Fig. 5.26: Error trend regarding h, Case B.

mitigation, however, simulation errors increase dramatically, with NMAE reaching 289.50% at $h = 3\,\mu\text{s}$. Applying $\Delta f = 60\,\text{kHz}$ results in an NMAE of 1.69%, which corresponds to 171.3 times improvement over the unshifted and uncompensated simulation. When combined with PRC, the NMAE is further reduced to 0.48%, yielding a total improvement factor of approximately 603.1 times. Remarkably, the FPRC method achieves an NMAE of 3.76% at $h = 7\,\mu\text{s}$, yielding results similar to those obtained with $h = 0.2\,\mu\text{s}$ in the unshifted and uncompensated simulation.

Table 5.10: Summary of NMAE, expressed in %, from time-domain simulations with $f_e = 60\,\text{kHz}$ for different Δf and h, Case B.

h (µs)	Δf (kHz)					
	0	0*	30	30*	60	60*
0.2	1.54	0.19	0.37	0.17	0.25	0.24
0.5	9.69	1.17	1.83	0.39	0.32	0.25
1	36.43	4.61	6.41	1.35	0.55	0.27
2	115.72	17.36	24.76	5.25	1.08	0.36
3	289.50	36.73	50.86	11.52	1.69	0.48
7	–	–	233.29	81.94	10.34	3.76

*Frequency shift + PRC.
–Aliasing due to the Nyquist frequency limit.

Fig. 5.27 provide qualitative evidence of the effectiveness of the FPRC method, displaying time-domain waveforms obtained with $h = 3\,\mu\text{s}$ for $\Delta f = 0\,\text{Hz}$, and $h = 7\,\mu\text{s}$ for $\Delta f = 60\,\text{kHz}$ with PRC. After each simulation, the frequency-shifted analytic signals are interpolated to a finer temporal resolution of 100 ps before extracting their real parts. The application of FPRC yields clear improvements, significantly reducing amplitude and phase errors, even at a larger time-step size.

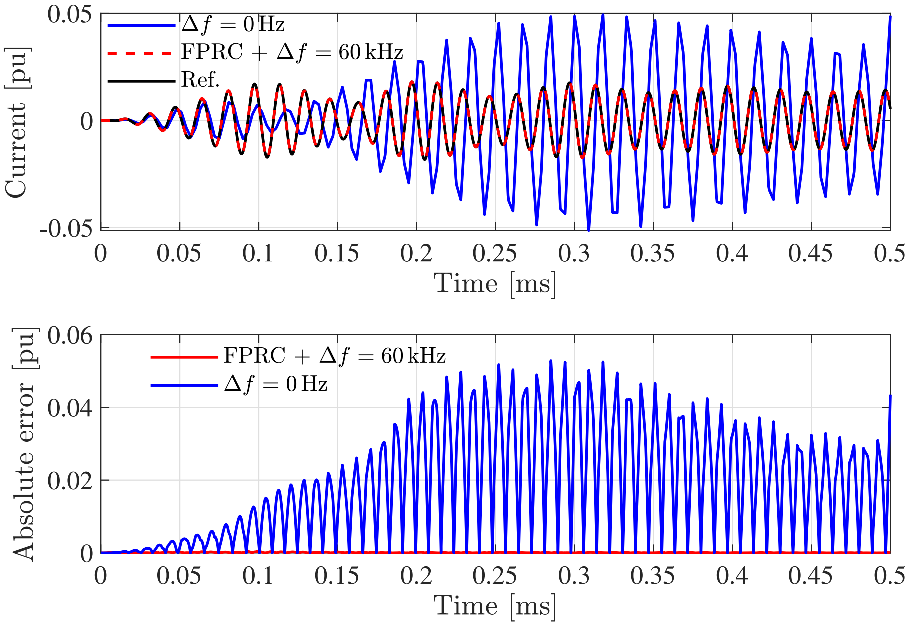

Fig. 5.27: Time-domain comparison of simulations (top) and its absolute errors (bottom) for Case B with $f_e = 60\,$kHz, using $h = 3\,\mu$s for $\Delta f = 0\,$Hz and $h = 7\,\mu$s for $\Delta f = 60\,$kHz.

5.4 General Remarks

This chapter presented two novel strategies, PRC and FPRC, for mitigating frequency warping errors in EMT simulations without reducing the time-step size, building on the frequency warping error analysis of Chapter 3 and the pole-residue rational modeling methods of Chapter 4.

PRC compensates frequency warping errors by scaling the poles and residues of a pole-residue rational model based on their imaginary frequency. This compensation targets eigenvalue perturbations caused by trapezoidal rule discretization. Case studies on transmission lines and distribution networks demonstrated improvements of up to 24 times in RMSE and 28.5 times in NMAE. In terms of simulation efficiency, the PRC enabled time-step sizes up to 6.7 times larger than those required by the uncompensated signals, without compromising accuracy. Its simplicity, computational efficiency, and accuracy make it a practical post-processing step for data-driven curve fitting, as it operates directly on existing rational models.

FPRC further reduces frequency warping by reducing the system effective bandwidth using frequency shifts and analytic signals. Frequency-shifted simulations are enabled through the realness constraint relaxation of the CVF. Results demonstrate that the FPRC method allows time-step sizes up to 35 times larger than those of uncompensated models, significantly reducing computational costs while preserving accuracy. For a given time-step size, the improvements in RMSE and NMAE metrics reach up to 901 times and 603 times, respectively.

Chapter 6

Conclusions

This thesis addresses frequency warping errors in electromagnetic transient (EMT) simulations for power system applications. Through rigorous analysis and novel compensation techniques, it establishes both a theoretical framework and practical solutions to enhance the simulation reliability and computational efficiency.

The study began by identifying frequency warping as a critical numerical artifact introduced by the trapezoidal rule, the most widely used integration method in EMT simulators. It revealed how frequency warping manifests in combined state-space and nodal analysis formulations, highlighting that even small frequency warping errors can accumulate over time, resulting in significant distortion in the output waveform. This occurs despite adherence to conventional time-step size h guidelines such as $h \leq 1/(10f_{\max})$ (MARTI and LIN, 1989; PALMAL *et al.*, 2023).

This thesis investigated modeling approaches based on rational models derived from data-driven curve-fitting techniques to enhance frequency-domain accuracy. Most significantly, it introduced the Complex Vector Fitting (CVF) method to power system applications (Y-parameters) for the first time. Originally developed for baseband modeling of photonic systems described by S-parameters, CVF enables the representation of non-Hermitian systems by relaxing the conjugacy constraint on poles and residues presented on the rational model. This added modeling flexibility resulted in accuracy improvements of up to eight orders of magnitude compared to traditional Vector Fitting (VF). Furthermore, CVF required up to 50% fewer poles and, in a certain case, achieved passive models where VF failed. Although the CVF fitting process incurs additional computational cost due to a greater number of decision variables, this was effectively alleviated by a parallel implementation using LAPACK routines and OpenMP directives.

Building on insights into frequency warping and non-Hermitian system modeling, two novel compensation techniques were developed: Pole-Residue Compensation (PRC) and Frequency-Shifted Pole-Residue Compensation (FPRC). These methods depart from traditional strategies that rely solely on reducing time-step size, which increases computational cost, and instead offer targeted approaches that directly address the frequency warping error.

By scaling the poles and residues of a rational model according to their imaginary frequency, the PRC method compensates for eigenvalue perturbation introduced by the trapezoidal rule discretization. Consequently, this scaling "stretches" the model's frequency response counteracting the spectrum compression introduced by frequency warping. Therefore, the method achieves high accuracy even for wide-band signals, making it ideal for EMT applications. Quantitatively, PRC reduced the Root Mean Square Error (RMSE) by up to 24 times and the Normalized Mean Absolute Error (NMAE) by up to 28.5 times relative to the uncompensated model.

A notable advantage of the PRC method is its post-processing nature, as it is applied after fitting but prior to simulation, enabling seamless integration into EMT software or existing simulation workflow. For example, the method can be directly implemented as an optional checkbox in the pre-simulation interface, which applies the compensation to all rational models within the simulation workspace. Another advantage of the pos-processing nature is that it can be applied to pre-existing models without any need for re-fitting, being particularly suitable for closed-box scenarios, where only the terminal behavior of the system is accessible. Another feature of the PRC method is its independence from prior knowledge of the excitation signal, allowing it to be applied generically without requiring specific input characteristics. Because VF and especially CVF yield reduced-order models, the PRC method, which performs a simple loop with a few basic mathematical operations per pole, has minimal computational overhead. For this reason, PRC should be adopted as a standard pre-simulation step to substantially increase accuracy at a minimal cost.

The FPRC is a hybrid method that combines the high accuracy and flexibility modeling of CVF with the error-compensation mechanism of PRC to improve simulation accuracy. Its distinctive feature is the use of the frequency shift as an additional optimization parameter. Unlike PRC, which can be seen as a single parameter (time-step size) optimization, FPRC additionally allows users to specify the frequency range of interest where accuracy must be maximized. This allowed the FPRC method to achieve the most significant accuracy improvement, with reductions up to 901 times in RMSE and 603 times in NMAE compared with the uncompensated model. This characteristic is especially valuable when specific oscillatory modes dominate system behavior that require precise representation. However, introducing the frequency-shift parameter turns the simulation into a multi-parameter optimization problem, where both the time-step size and the frequency shift must be tuned to balance accuracy and computational efficiency. Despite the increased setup complexity, it permits fine-tuned simulations customized for the specific requirements of each study.

A key advantage of the PRC and FPRC methods is that their accuracy improvements can be exploited to achieve more computationally efficient simulations. Results show that these methods allow significantly larger time-step sizes, up to 6.7 times for PRC and 35 times for FPRC, without compromising simulation accuracy, compared to uncompensated models. This reduction in numerical operations and memory accesses accelerates simulations and enables longer or more detailed analyses with the same computational resources. For instance, in real-time applications, the computational savings enable the simulation of larger networks or systems with higher levels of detail, which would otherwise be infeasible due to hardware limitations.

Together, the proposed PRC and FPRC methods provide advanced tools for performing efficient and reliable EMT simulations, with significant potential for parametric studies, large-scale simulations, long-duration analyses, and real-time applications. These methods enable broader and more detailed system-level studies, an essential capability for analyzing and planning modern power grids.

6.1 Future work

Future research endeavors include:

1. generalizing the proposed techniques to other numerical integration methods, expanding their applicability across diverse EMT simulation platforms;
2. evaluate the impact of frequency warping in the propagation constant of transmission lines and cables with distributed parameters to assess the implications for modeling and simulation;
3. implementing passivity enforcement routines for non-Hermitian admittance models to ensure stable time-domain simulations;
4. extending the proposed methods to multiscale systems, particularly for co-simulation scenarios with multiple time-step sizes, to enhance simulation efficiency;
5. investigating the integration of the proposed PRC and FPRC methods, into real-time simulation frameworks to assess their feasibility viability for Hardware-In-the-Loop applications;
6. designing adaptive algorithms to dynamically compensate parameters based on real-time frequency estimation of the system, thereby reducing frequency warping errors during simulation.

References

ABDEL-RAHMAN, M., SEMLYEN, A., REZA IRAVANI, M., 2003, "Two-layer network equivalent for electromagnetic transients", *IEEE Transactions on Power Delivery*, v. 18, n. 4, pp. 1328–1335.

AMETANI, A., 2015, *Numerical Analysis of Power System Transients and Dynamics*. Energy Engineering. UK, Institution of Engineering and Technology.

BEZA, M., BONGIORNO, M., 2020, "Impact of converter control strategy on low- and high-frequency resonance interactions in power-electronic dominated systems", *International Journal of Electrical Power and Energy Systems*, v. 120, pp. 105978.

BOASHASH, B., 2003, "Chapter 4 - Time-Frequency Signal and System Analysis". In: *Time Frequency Analysis*, Elsevier Science, pp. 85–158, Oxford.

BRADDE, T., GRIVET-TALOCIA, S., ZANCO, A., et al., 2022, "Data-Driven Extraction of Uniformly Stable and Passive Parameterized Macromodels", *IEEE Access*, v. 10, pp. 15786–15804.

BRAMBILLA, A., D'AMORE, D., 1993, "The simulation errors introduced by the spice transient analysis", *IEEE Transactions on Circuits and Systems I: Fundamental Theory and Applications*, v. 40, n. 1, pp. 57–60.

BRAMBILLA, A., STORTI-GAJANI, G., 2003, "Frequency warping in time-domain circuit simulation", *IEEE Transactions on Circuits and Systems I: Fundamental Theory and Applications*, v. 50, n. 7, pp. 904–913.

BRANDWAJN, V., 1977, *Synchronous generator models for the simulation of electromagnetic transients*. Ph.D. Thesis, University of British Columbia.

CAMPELLO, T., VARRICCHIO, S., TARANTO, G., et al., 2020, "Enhancements in vector fitting implementation by using stopping criterion, frequency partitioning and model order reduction", *International Journal of Electrical Power & Energy Systems*, v. 120, pp. 105905.

CAMPELLO, T., VARRICCHIO, S., TARANTO, G., 2021, "Three-Phase Frequency-Dependent Network Equivalents in the ATP for Lumped Parameter Systems Using Descriptor Formulation, Rational Models, and Symmetrical Component Data", *Journal of Control, Automation and Electrical Systems*, v. 32, pp. 1690–1703.

CAMPELLO, T., DICLER, F., VARRICCHIO, S., et al., 2023, "Reviewing the large electrical network equivalent methods under development for electromagnetic transient studies in the Brazilian Interconnected power system", *International Journal of Electrical Power & Energy Systems*, v. 151, pp. 109033.

CHEN, L., XIE, X., HE, J., et al., 2023, "Wideband oscillation monitoring in power systems with high-penetration of renewable energy sources and power electronics: A review", *Renewable and Sustainable Energy Reviews*, v. 175, pp. 113148.

CHINEA, A., GRIVET-TALOCIA, S., 2011, "On the parallelization of vector fitting algorithms", *IEEE Transactions on Components, Packaging and Manufacturing Technology*, v. 1, n. 11, pp. 1761–1773.

CHOU, C. C., SCHUTT-AINE, J. E., 2021, "On the Acceleration of the Vector Fitting for Multiport Large-Scale Macromodeling", *IEEE Microwave and Wireless Components Letters*, v. 31, n. 1, pp. 1–4.

COHEN, L., 1995, *Time-frequency analysis: theory and applications.* USA, Prentice-Hall, Inc.

CONSTANTINESCU, F., GHEORGHE, A. G., NIŢESCU, M., 2010, "THE ENERGY BALANCE ERROR FOR CIRCUIT TRANSIENT ANALYSIS", *Revue Roumaine des Sciences Techniques, Série Électrotechnique et Énergétique*, v. 54, n. 3, pp. 243–250.

DAHLQUIST, G. G., 1963, "A special stability problem for linear multistep methods", *BIT*, v. 3, n. 1, pp. 27–43.

DESCHRIJVER, D., DHAENE, T., DE ZUTTER, D., 2008a, "Robust Parametric Macromodeling Using Multivariate Orthonormal Vector Fitting", *Microwave Theory and Techniques, IEEE Transactions on*, v. 56, n. 7 (Jul.), pp. 1661 –1667.

DESCHRIJVER, D., MROZOWSKI, M., DHAENE, T., et al., 2008b, "Macromodeling of Multiport Systems Using a Fast Implementation of the Vector Fitting Method", *IEEE Microwave and Wireless Components Letters*, v. 18, n. 6 (Jun.), pp. 383–385.

DESCHRIJVER, D., DHAENE, T., 2007, "A Note on the Multiplicity of Poles in the Vector Fitting Macromodeling Method", *IEEE Transactions on Microwave Theory and Techniques*, v. 55, n. 4, pp. 736–741.

DESCHRIJVER, D., GUSTAVSEN, B., DHAENE, T., 2007, "Advancements in Iterative Methods for Rational Approximation in the Frequency Domain", *IEEE Transactions on Power Delivery*, v. 22, n. 3, pp. 1633–1642.

DICLER, F., 2021, *Contributions to the FPGA and CPU implementation of Frequency-Dependent Network Equivalents for real-time and offline electromagnetic transient power system simulators.* Masters Thesis, PEE/-COPPE/UFRJ, Nov.

DOMMEL, H. W., 1995, *Electromagnetic Transients Program Reference Manual (EMTP Theory Book).* Branch of System Engineering - Bonneville Power Administration.

DOMMEL, H. W., 1996, *Electromagnetic Transients Program Reference Manual, Theory Book.* Vancouver, Canada, Department of Electrical Engineering, The University of British Columbia.

DOMMEL, H., 1969, "Digital Computer solution of electromagnetic transients in single and multi-phase networks", *IEEE Transactions on PAS*, v. 88, n. 2 (Apr.), pp. 734–741.

DUFOUR, C., MAHSEREDJIAN, J., BÉLANGER, J., 2011, "A Combined State-Space Nodal Method for the Simulation of Power System Transients", *IEEE Transactions on Power Delivery*, v. 26, n. 2, pp. 928–935.

EVANGELISTA, G., CAVALIERE, S., 2001, "Audio Effects Based on Biorthogonal Time-Varying Frequency Warping", *EURASIP Journal on Advances in Signal Processing*, v. 2001, n. 1 (Mar.), pp. 289319.

GAD, E., NAKHLA, M., ACHAR, R., et al., 2009, "A-stable and L-stable high-order integration methods for solving stiff differential equations", *IEEE Transactions on Computer-Aided Design of Integrated Circuits and Systems*, v. 28, n. 1 (Jan.), pp. 1359–1372.

GANESHAN, S., ELUMALAI, N. K., ACHAR, R., et al., 2020, "GVF: GPU-Based Vector Fitting for Modeling of Multiport Tabulated Data Networks", *IEEE Transactions on Components, Packaging and Manufacturing Technology*, v. 10, n. 8, pp. 1375–1387.

GAO, K., 2015, *A Study in the Frequency Warping of Time-Domain Methods.* Master, University of Ottawa, Ottawa.

GHEORGHE, A. G., CONSTANTINESCU, F., NITESCU, M., 2009, "Error control in circuit transient analysis". In: *2009 16th IEEE International Conference on Electronics, Circuits and Systems - (ICECS 2009)*, pp. 207–210, Dec.

GONZALEZ-LONGATT, F. M., 2015, "Activation schemes of synthetic inertia controller on full converter wind turbine (type 4)". In: *2015 IEEE Power & Energy Society General Meeting*, pp. 1–5, Jul.

GRIVET-TALOCIA, S., GUSTAVSEN, B., 2015, *Passive Macromodeling: Theory and Applications*, v. 239, *Wiley Series in Microwave and Optical Engineering.* New York, US, John Wiley & Sons.

GRIVET-TALOCIA, S., GUSTAVSEN, B., 2016, "Black-Box Macromodeling and its EMC Applications", *IEEE Electromagnetic Compatibility Magazine*, v. 5, pp. 71–78.

GUSTAVSEN, B., 2002, "Rational approximation of frequency-dependent admittance matrices", *IEEE Transactions on Power Delivery*, v. 17, n. 4, pp. 1093–1098.

GUSTAVSEN, B., 2006, "Relaxed Vector Fitting Algorithm for Rational Approximation of Frequency Domain Responses". In: *Signal Propagation on Interconnects, 2006. IEEE Workshop on*, pp. 97 –100, May.

GUSTAVSEN, B., 2007, "Computer Code for Passivity Enforcement of Rational Macromodels by Residue Perturbation", *Advanced Packaging, IEEE Transactions on*, v. 30, n. 2 (May), pp. 209–215.

GUSTAVSEN, B., 2008a, "Fast Passivity Enforcement for Pole-Residue Models by Perturbation of Residue Matrix Eigenvalues", *IEEE Transactions on Power Delivery*, v. 23, n. 4, pp. 2278–2285.

GUSTAVSEN, B., 2010, "Study of Transformer Resonant Overvoltages Caused by Cable-Transformer High-Frequency Interaction", *IEEE Transactions Power Delivery*, v. 25, n. 2 (Apr.), pp. 770–779.

GUSTAVSEN, B., MO, O., 2007, "Interfacing convolution based linear models to an electromagnetic transients program". In: *Proc. Int. Conf. Power Systems Transients*, pp. 4–7, Jun.

GUSTAVSEN, B., NORDSTROM, J., 2008, "Pole Identification for The Universal Line Model Based on Trace Fitting", *IEEE Transactions on Power Delivery*, v. 23, n. 1 (Jan.), pp. 472 –479.

GUSTAVSEN, B., SEMLYEN, A., 1999, "Rational approximation of frequency domain responses by vector fitting", *IEEE Transactions on Power Delivery*, v. 14, n. 3 (Jul.), pp. 1052–1061.

GUSTAVSEN, B., SEMLYEN, A., 2009, "Admittance-Based Modeling of Transmission Lines by a Folded Line Equivalent", *IEEE Transactions on Power Delivery*, v. 24, n. 1 (Jan), pp. 231–239.

GUSTAVSEN, B., SEMLYEN, A., 1998, "Simulation of Transmission Line Transients Using Vector Fitting and Modal Decomposition", *IEEE Transactions on Power Delivery*, v. 13, pp. 605–614.

GUSTAVSEN, B., 2013, "Avoiding Numerical Instabilities in the Universal Line Model by a Two-Segment Interpolation Scheme", *IEEE Transactions on Power Delivery*, v. 28, n. 3 (Jul.), pp. 1643–1651.

GUSTAVSEN, B., 2008b. "The Vector Fitting Website". b. Available at: <`https://www.sintef.no/projectweb/vectorfitting/`>.

GUSTAVSEN, B., DE SILVA, H. M., 2013, "Inclusion of rational models in an electromagnetic transients program: Y-Parameters, Z-Parameters, S-parameters, transfer functions", *IEEE Transactions on Power Delivery*, v. 28, n. 2, pp. 1164–1174.

GUSTAVSEN, B., SEMLYEN, A., 2001, "Enforcing Passivity for Admittance Matrices Approximated by Rational Functions", *IEEE Transactions on Power Systems*, v. 16, n. 1 (Feb.), pp. 97–104.

GUSTAVSEN, B., SEMLYEN, A., 2004, "A Robust Approach for System Identification in the Frequency Domain", *IEEE Transactions on Power Delivery*, v. 3, pp. 1167–1173.

GUSTAVSEN, B., 2021, "Passivity Enforcement by Residue Perturbation via Constrained Non-Negative Least Squares", *IEEE Transactions on Power Delivery*, v. 36, n. 5, pp. 2758–2767.

HENDRICKX, W., DHAENE, T., 2006, “A discussion of "Rational approximation of frequency domain responses by vector fitting"”, *IEEE Transactions on Power Systems*, v. 21, n. 1, pp. 441–443.

HØIDALEN, H. K., 2024. “ATPDraw News”. Available at: <`https://www.atpdraw.net/news.php`>.

IHLENFELD, L. P. R. K., OLIVEIRA, G. H. C., 2021, “Completion-Based Passivity Enforcement for Multiport Networks Rational Models”, *IEEE Transactions on Power Delivery*, v. 36, n. 4, pp. 2213–2220.

INTEL, 2023. “Intel oneAPI Math Kernel Library”. Available at: <`https://www.intel.com/content/www/us/en/developer/tools/oneapi/onemkl.html`>.

JI, Y., XING, Y., 2023, “Highly Accurate and Efficient Time Integration Methods with Unconditional Stability and Flexible Numerical Dissipation”, *Mathematics*, v. 11, n. 3.

KABIR, M., KHAZAKA, R., 2012, “Macromodeling of Distributed Networks From Frequency-Domain Data Using the Loewner Matrix Approach”, *IEEE Transactions on Microwave Theory and Techniques*, v. 60, n. 12, pp. 3927–3938.

KING, J. B., BRAZIL, T. J., 2017, “Time-domain simulation of passband S-parameter networks using complex baseband vector fitting”. In: *2017 Integrated Nonlinear Microwave and Millimetre-wave Circuits Workshop (INMMiC)*, pp. 1–4. IEEE, Apr.

KUROKAWA, S., YAMANAKA, F. N., PRADO, A. J., et al., 2009, “Inclusion of the frequency effect in the lumped parameters transmission line model: State space formulation”, *Electric Power Systems Research*, v. 79, n. 7, pp. 1155–1163.

LEE, L., ROSE, R., 1998, “A frequency warping approach to speaker normalization”, *IEEE Transactions on Speech and Audio Processing*, v. 6, n. 1, pp. 49–60.

LEI, C.-U., CHEUNG, C.-M., KWAN, H.-K., et al., 2008, “Efficient Complex Continuous-Time IIR Filter Design via Generalized Vector Fitting”. In: *Proceedings of the International MultiConference of Engineers and Computer Scientists*, v. II, pp. 19–21, Mar.

LIMA, A. C., CAMARA, F., SALVADOR, J. P., et al., 2020, "Frequency-dependent equivalent based on idempotent decomposition and grouping", *Electric Power Systems Research*, v. 189, pp. 106800.

MARTI, J., LIN, J., 1989, "Suppression of numerical oscillations in the EMTP", *IEEE Transactions on Power Systems*, v. 4, n. 2, pp. 739–747.

MATHWORKS, 2023. "The MATLAB Multicore". Available at: <`https://www.mathworks.com/discovery/matlab-multicore.html`>.

MOORMANN, D., LOOYE, G., 2002, "The Modelica flight dynamics library". In: *Proceedings of the 2nd International Modelica Conference*, pp. 275–284, Mar.

MORALES RODRIGUEZ, J., MEDINA, E., MAHSEREDJIAN, J., et al., 2020, "Frequency-Domain Fitting Techniques: A Review", *IEEE Transactions on Power Delivery*, v. 35, n. 3, pp. 1102–1110.

MORCHED, A., GUSTAVSEN, B., TARTIBI, M., 1999, "A universal model for accurate calculation of electromagnetic transients on overhead lines and underground cables", *IEEE Transactions on Power Delivery*, v. 14, n. 3 (Jul.), pp. 1032–1038.

NAREDO, J., MAHSEREDJIAN, J., GUTIERREZ-ROBLES, J., et al., 2011, "Improving the numerical performance of transmission line models in EMTP". In: *Proceedings of the International Conference on Power Systems Transients*, pp. 1–8, Jun.

NODA, T., 2005, "Identification of a multiphase network equivalent for electromagnetic transient calculations using partitioned frequency response", *IEEE Transactions on Power Delivery*, v. 20, n. 2 (Apr.), pp. 1134 – 1142.

OMAR FARUQUE, M. O., DINAVAHI, V., 2010, "Hardware-in-the-loop simulation of power electronic systems using adaptive discretization", *IEEE Transactions on Industrial Electronics*, v. 57, n. 4, pp. 1146–1158.

OPPENHEIM, A., JOHNSON, D., 1972, "Discrete representation of signals", *Proceedings of the IEEE*, v. 60, n. 6, pp. 681–691.

PALMAL, M., ROJA, P., JOHN, V., 2023, "Revisiting Numerical Integration Methods for Digital Implementation in Power Electronics Applications". In: *2023 11th National Power Electronics Conference (NPEC)*, pp. 1–6. IEEE, Dec.

PAOLONE, M., GAUNT, T., GUILLAUD, X., et al., 2020, "Fundamentals of power systems modelling in the presence of converter-interfaced generation", *Electric Power Systems Research*, v. 189, n. Apr., pp. 106811.

PERŠIČ, B., 1994, "SPICE transient analysis errors estimated in frequency space", *Electronics Letters*, v. 30, n. 8 (Apr.), pp. 617–618.

PERŠIČ, B., BASARIČ, N., 2001, "Frequency Warping and Chaotic Behaviour Generated by SPICE", *Informacije MIDEM*, v. 1, n. 31, pp. 26–32.

PRESTI, L. L., 1983, "Prewarping techniques in filter simulation by bilinear transformation", *Signal Processing*, v. 5, n. 6, pp. 523–529.

RAHIMI PORDANJANI, I., XU, W., 2014, "Improvement of vector fitting by using a new method for selection of starting poles", *Electric Power Systems Research*, v. 107, pp. 206–212.

RAHKONEN, T., ANDREANI, P., 2005, "Numerical effects in time-domain simulations of electronic circuits - A reminder", *23rd NORCHIP Conference 2005*, v. 2005, pp. 28–31.

RAMIREZ, A., 2008, "Vector fitting-based calculation of frequency-dependent network equivalents by frequency partitioning and model-order reduction", *IEEE Transactions on Power Delivery*, v. 24, n. 1, pp. 410–415.

RODRÍGUEZ, J. M., 2019, *Computation of Frequency Dependent Network Equivalents Using Vector Fitting, Matrix Pencil Method and Loewner Matrix*. Ph. d. thesis, Université de Montréal, Montreal, Canada.

SALARIEH, B., DE SILVA, H., 2021, "Review and comparison of frequency-domain curve-fitting techniques: Vector fitting, frequency-partitioning fitting, matrix pencil method and Loewner matrix", *Electric Power Systems Research*, v. 196, pp. 107254.

SEMLYEN, A., DABULEANU, A., 1975, "Fast and accurate switching transient calculations on transmission lines with ground return using recursive convolutions", *IEEE Transactions on Power Apparatus and Systems*, v. 94, n. 2, pp. 561–571.

SHESHYEKANI, K., KARAMI, H. R., DEHKHODA, P., et al., 2012, "Application of the Matrix Pencil Method to Rational Fitting of Frequency-Domain Responses", *IEEE Transactions on Power Delivery*, v. 27, n. 4, pp. 2399–2408.

SPINA, D., YE, Y., DESCHRIJVER, D., et al., 2021, “Complex vector fitting toolbox: a software package for the modelling and simulation of general linear and passive baseband systems”, *Electronics Letters*, v. 57, n. 10, pp. 404–406.

TAN, L., 2008, *Digital Signal Processing: Fundamentals and Applications.* 1 ed. Decatur, Georgia, Academic Press.

TENG, W., ZHANG, X., ZHANG, Y., et al., 2016, “Iterative tuning notch filter for suppressing resonance in ultra-precision motion control”, *Advances in Mechanical Engineering*, v. 8, n. 11, pp. 1687814016674097.

TIAN, X., LEE, S. W., WU, Z., et al., 2017, “An exemplar-based approach to frequency warping for voice conversion”, *IEEE/ACM Transactions on Audio, Speech, and Language Processing*, v. 25, n. 10, pp. 1863–1876.

TRIVERIO, P., 2021, “Vector fitting”, *System- and Data-Driven Methods and Algorithms*, v. 1, pp. 275–310.

ULLRICK, T., SPINA, D., BOGAERTS, W., et al., 2023, “Wideband parametric baseband macromodeling of linear and passive photonic circuits via complex vector fitting”, *Scientific Reports*, v. 13, n. 1, pp. 1–22.

UPADHYAY, N., ROSALES, H. G., 2018, “Robust recognition of English speech in noisy environments using frequency warped signal processing”, *National Academy Science Letters*, v. 41, n. 1, pp. 15–22.

VARRICCHIO, S. L., GOMES, S., 2018, “Electrical network dynamic models with application to modal analysis of harmonics”, *Electric Power Systems Research*, v. 154, pp. 433–443.

WANG, J., WANG, J., LUO, X., 2019, “Novel PLL for power converters under unbalanced and distorted grid conditions”, *The Journal of Engineering*, v. 2019, n. 17, pp. 3895–3899.

YANG, W. Y., SONG, T. G. C. I. H., HEO, Y. S. C. J., et al., 2009, *Signals and Systems with MATLAB.* Berlin, Heidelberg, Springer.

YE, Y., SPINA, D., XING, Y., et al., 2018, “Numerical modeling of a linear photonic system for accurate and efficient time-domain simulations”, *Photonics Research.*, v. 6, n. 6 (Jun.), pp. 560–573.

YE, Y., SPINA, D., DESCHRIJVER, D., et al., 2019, “Time-domain compact macromodeling of linear photonic circuits via complex vector fitting”, *Photonics Research*, v. 7, n. 7, pp. 771.

YE, Y., ULLRICK, T., BOGAERTS, W., et al., 2022, "SPICE-Compatible Equivalent Circuit Models for Accurate Time-Domain Simulations of Passive Photonic Integrated Circuits", *Journal of Lightwave Technology*, v. 40, n. 24, pp. 7856–7868.

YEUNG, G., FAN, R., ALWAN, A., 2021, "Fundamental frequency feature warping for frequency normalization and data augmentation in child automatic speech recognition", *Speech Communication*, v. 135, pp. 1–10.

ZHANG, P., MARTI, J. R., DOMMEL, H. W., 2010, "Shifted-Frequency Analysis for EMTP Simulation of Power-System Dynamics", *IEEE Transactions on Circuits and Systems I: Regular Papers*, v. 57, n. 9, pp. 2564–2574.

ZOU, C., RAO, H., XU, S., et al., 2018, "Analysis of Resonance Between a VSC-HVDC Converter and the AC Grid", *IEEE Transactions on Power Electronics*, v. 33, n. 12, pp. 10157–10168.

Appendix A

Analysis of the Initial Phase Inversion in RC$_4$

In the beginning of the simulation, $n = 0$ and the initial voltage at capacitor C$_1$ is 1 V ($V_{C_1}(0) = 1\,\mathrm{V}$). In the next time step ($n = 1$), a phase inversion is observed as the voltage at RC$_4$ increases and the analytic response decreases, as seen in Fig. 3.13. Per-unit values will be used in this section to simplify the notation. $V_{C_1}(n)$ can be computed with

$$V_{C_1}(n) = G_A^{-1}\left(I_A(n) - G_{L1}\cos(120\pi nh)\right), \tag{A.1}$$

where

$$G_A = G_{C_1} + G_{SS} + G_{L_1} \quad \text{and} \tag{A.2}$$

$$I_A(n) = I_{h_{C_1}}(n) - I_{h_{SS}}(n) - I_{h_{L_1}}(n). \tag{A.3}$$

The phase inversion at $n = 1$ implies that the voltage at the capacitor increases, so

$$V_{C_1}(1) > 1. \tag{A.4}$$

The condition in (A.4) is satisfied if

$$G_A^{-1}\big(I_A(1) - G_{L_1}\cos\big(120\pi \times 4 \times 10^{-6}\big)\big) > 1. \tag{A.5}$$

By replacing (A.2) and (A.3) in (A.5),

$$I_{h_{C_1}}(1) - I_{h_{SS}}(1) - I_{h_{L_1}}(1) - G_{L_1}\cos\big(120\pi \times 4 \times 10^{-6}\big) > G_{C_1} + G_{SS} + G_{L_1}. \tag{A.6}$$

Isolating G_{SS},

$$G_{SS} \ < \Phi(1), \tag{A.7}$$

where

$$\Phi(1) = I_{h_{C_1}}(1) - I_{h_{SS}}(1) - I_{h_{L_1}}(1) - G_{L_1} \cos\left(120\pi \times 4 \times 10^{-6}\right) - (G_{C_1} + G_{L_1}). \quad \text{(A.8)}$$

For RC$_4$, $I_{h_{C_1}}(1) = 50\,\text{pu}$, $I_{h_{SS}}(1) = 50\,\text{pu}$, $I_{h_{L_1}}(1) = 0\,\text{pu}$, $G_{L_1} = 2\,\text{pu}$, $G_{C_1} = 50\,\text{pu}$ and $G_{SS} = 0.392\,28\,\text{pu}$, which leads to

$$\Phi(1) = 1.01. \quad \text{(A.9)}$$

Thus, (A.7) is satisfied.

Table A.1 demonstrates that the initial phase inversion occurs when the condition given in (A.7) is satisfied, which was the case only for RC$_4$.

Table A.1: Per-unit values of G_{SS} and $\Phi(1)$

Nomenclature	G_{SS}	$\Phi(1)$	$G_{SS} < \Phi(1)$?	Initial phase inversion?
TR$_1$	0.384 62	−0.38	No	No
TR2	0.476 19	−0.48	No	No
TR4	0.384 62	−0.38	No	No
RC1	0.445 01	−0.35	No	No
RC2	0.666 62	−0.16	No	No
RC4	0.392 28	1.01	Yes	Yes